Turbulence in the wake of a roughness patch

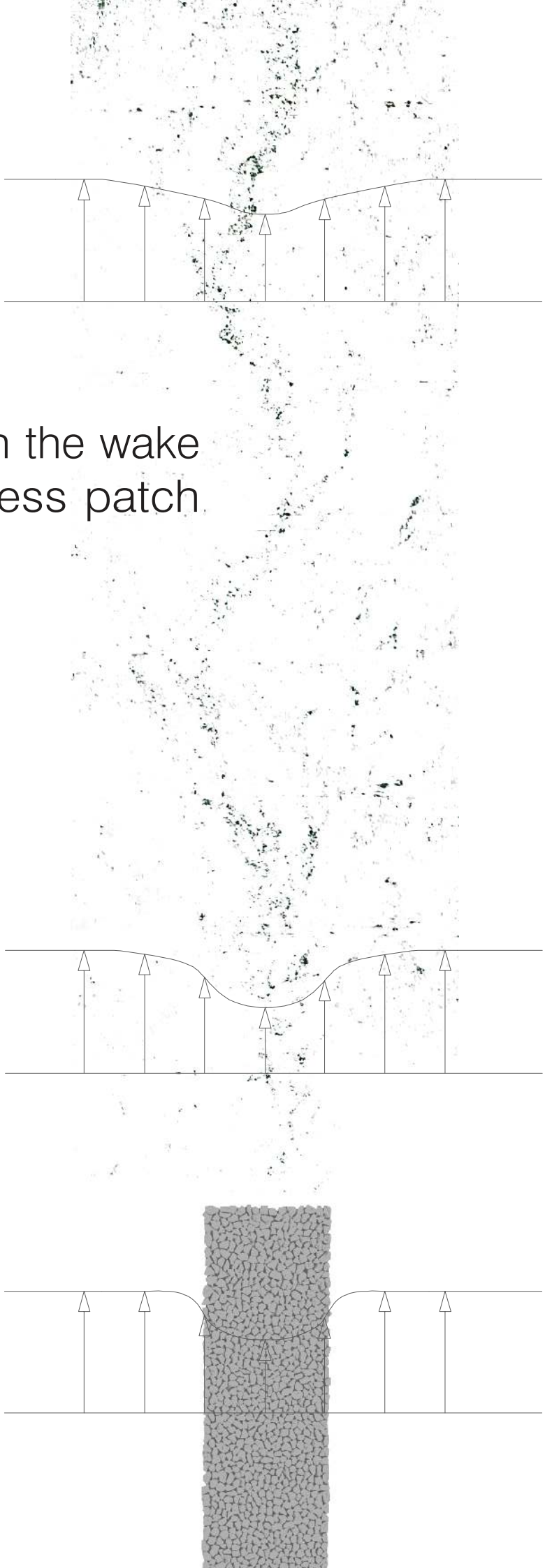

J.J. Voermans

TU Delft

Delft University of Technology
Faculty of Civil Engineering and Geosciences
Section of Environmental Fluid Mechanics

Turbulence in the wake of a roughness patch

J.J. Voermans
March 2013

Thesis comittee
Prof.dr.ir. W.S.J. Uijttewaal
Dr.ir. B.C. van Prooijen
Dr.ir. W.-P. Breugem

TU Delft

Preface

This thesis is the final element of my 6.5 years studying period at the TU Delft as a student. Although I am grateful for the switch to the study of Environmental Fluid Mechanics, the three years at Architecture are not considered to be a waste, since my graphical insight and skills are considered to become a characteristic personal quality. Apart from the tremendous amount of lectures given at the TU Delft, the learning (theoretical, practical and personal) has been most evident during the execution of this project.
Therefore, I would like to thank the committee, Bram van Prooijen, Wim-Paul Breugem and especially Wim Uijttewaal, for their contribution and assistance in this thesis.

I would like to thank my parents and the rest of the family for their support in switching faculty and fun time during non-TU-Delft-related matters. Finally thanks for my roommate and off course to my friends at Architecture.

It is now time to read ‘ Turbulence in the wake of a roughness patch’.

Joey Voermans.

March 2013.

Summary

Little research was done in the past concerning the propagation of three dimensional effect in shallow wake flow caused by a roughness patch. Today's research on related subjects is dominated by emerging obstructions in shallow water where the flow can be assumed as (quasi) two dimensional. However the relevance of a submerged obstruction with increased roughness can be found in wake control, oyster reefs, river- and estuary bottoms and heterogeneous land occupancy. To get a better understanding of the consequences of the three dimensionality of the flow structures, experiments are performed in a wide shallow flume to examine these structures. The main objective is to examine whether the wake structure of a roughness patch can be treated as (quasi)-two-dimensional.

The objective has been answered by a combination of a literature study and an experiment performed at the faculty's laboratory. The results show four dominant mechanisms in the wake of a roughness patch: transverse mass flux, bottom friction, mixing layer and the secondary circulation. Based on a momentum balance the transverse mass flux and the bottom friction are the largest contributions to this balance. Although the contribution of the mixing layer and the secondary circulation to the recovery of the wake are of the order of 10%, their influence on the flow structure is more pronounced. The mixing layer is shifted towards the wake centerline due to the presence of a transverse mass flux forming a misalignment between the maximum spanwise Reynolds stress and the position of the wake half width. Since this shift is of limited influence on the position of the secondary circulation, a misalignment if formed between the maximum momentum transport by the secondary circulation and the mixing layer causing a lower streamwise velocity at the edge of wake with respect to the wake of an emerging obstruction. The secondary circulation is responsible for the transport of low momentum fluid towards the edge of the wake near the bottom, and high momentum fluid towards the wake centerline near the surface. This behavior is responsible for the cross gradient in the streamwise velocity profiles as shown by the data obtained.

For modeling purposes of well mixed quantities, a (quasi)-two-dimensional approach only holds if the weaker streamwise velocity near the edge of the wake is taken into account. In the case a prediction of depth varying quantities is desired, the cross gradient caused by the secondary circulation needs to be implemented as well which results in the need of a three-dimensional modeling approach.

Table of contents

1. Introduction

Changes in surface roughness is a topic of interest for researches in all fields related to fluid mechanics for decades. The flow of wind blowing over the earth's surface meets a continuously changing set of boundary conditions, which is in meteorology modeled as a change in surface roughness (e.g. Pendergrass & Arya [1984] and Panofsky & Townsend [1964]). In compound channel flow, floodplains usually have a relative higher surface roughness with respect to the main channel. Although the flow structure caused by the shear between the floodplain and main channel is in itself already complex, additional mechanisms as a secondary circulation makes it even more difficult. These secondary circulations are not confined to compound channel flow. Their presence have been shown in rectangular open channel experiments and in models as well, caused by lateral roughness changes (e.g. Noat [1984] and Tominaga et al. [1989]).

Every obstruction in a flow can be translated in a local increase of surface roughness. One way to quantify this translation is by determining the effects of the element on the mean velocity profile. This translation holds until the flow structure around the obstruction is examined in more detail and/or specific turbulent characteristics are of importance (Krogstad, Antonia, & Browne, 1992).

Research topics as air pollution and sediment transport due to obstructions are examples of subjects where the turbulent structures are of importance and the flow needs to be examined in more detail. These turbulent structures can be expected with the presence of local mean velocity gradients, which will be in general downstream of the obstruction. These disturbances of the mean flow are called 'wake flows'. Furthermore, the speed at which these disturbances propagate in the transverse direction is related to the stability of the wake.

The establishment of wakes is sensitive for many parameters, they can occur in all length and time scales with changing intensity. For instance, Ingram & Chu [1987] investigated the island wakes of the order of a few hundred meters, whereas stirring in cup of coffee with a spoon can introduce a wake size of just a few millimeters. Besides the span of length scales, all sort of variations on the appearance of obstruction have been studied, for example Zong & Nepf [2012] examined wake flow behind a circular porous cylinder.
In most studies performed on wake flows, the configuration of the obstruction makes the simplification to (nearly)-two-dimensional flow appropriate i.e. the obstruction is fully emerged and the horizontal length scale is large compared to the water depth. Nevertheless, this simplification is not valid in every occasion for instance when the obstruction is submerged. While vortices dominate in the horizontal plane for solid emergent obstructions this does not necessarily hold for submerged obstruction where it has been shown that secondary currents can play a significant role (e.g. Vermaas et al., 2011).

1.1. Problem description

Villages, vegetation, coral reefs or any other submerged obstruction in a flow will locally change the velocity profiles as well as the turbulence characteristics. As mentioned by Rominger & Nepf [2011], these structures are usually organized in patches with a limited length, including a distinct leading edge perpendicular to the mean flow. However, many studies examined a continuous surface of roughness change and thereby taking advantage of a fully developed flow. Even though, today's

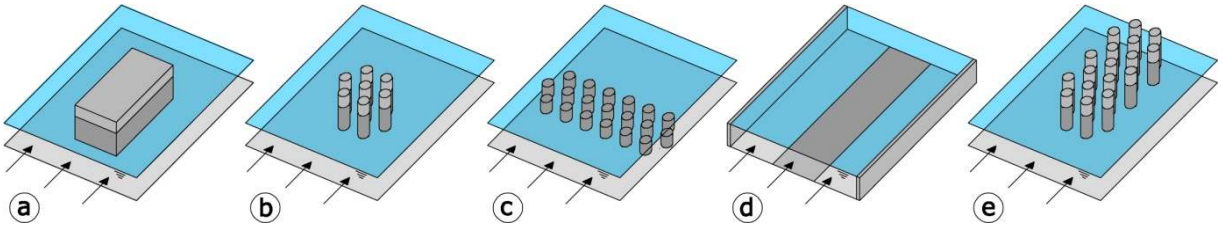

Figure 1; Overview of experimental layout of the obstructions in various studies; e.g. a) Balachander & Tachie [2001], b) Nepf & Zong [2012], c) Huthoff et al. [2007], d) Noat [1984], e) Rominger & Nepf [2011].

experiments done on patch like obstructions cannot be applied on (submerged) roughness patches since three dimensional effects are absent due to the experimental set-up. Note: these three dimensional effects are not always a necessary subject in the objectives of these studies.
These obstructions are shown in Figure 1. The solid obstruction in Fig. 1a is blocking the interaction of the vortices on both sides of the obstruction. This interaction is however still possible in Fig. 1b-1e due to the 'porosity' of the obstruction. In Fig. 1b the emergence of the cylinders causes the flow in the horizontal plane to dominate. In Fig. 1c and 1d, respectively the lateral extent of the submerged cylinders and the sidewalls causes noticable influence on the turbulent structures. In Fig. 1d a continous roughness band is used which is taking care of the existence of fully developed flow similar to the structure of Fig. 1e.

1.1.1. Scientific relevance

Submerged obstructions acting like increased roughness patches contribute to the change of the flow structure somewhat in front but mainly downstream of the obstruction, called the wake. Due to its freestanding position, a variety of turbulent structures can appear which are only partly addressed in the experiments shown in Figure 1c-e. In addition these turbulent structures can act as a (de)stabilizer on the wake.

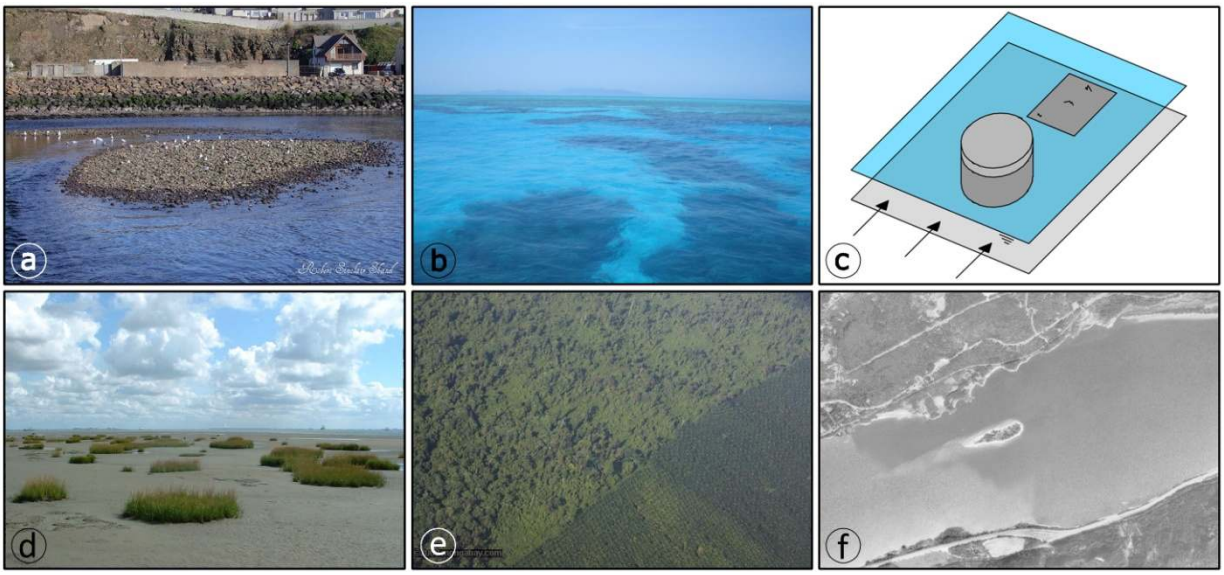

Figure 2; Examples of application;
a) patch of rocks in an estuary, New Zealand *(http://www.flickr.com/photos/scorriesisland/3376295133/in/photostream/), 21-05-'12*;
b) patches of oyster reefs, Australia *(http://www.flickr.com/photos/35593477@N00/1130545372/), 21-05'12*;
c) roughness patch as wake stabilizer *(Negretti et al. [2005])*.
d) developing salt marsh *(http://chapter.ser.org/europe/files/2012/08/VandeKoppel.pdf), 26-02-'13;*
e) Palm oil plantation *(http://world.mongabay.com/dutch/travel/malaysia/p23416p.html), 26-02-'13;*
f) River island, Columbia river *(http://users.rowan.edu/~Wyrick/presentations/River%20Islands%20Hydraulics.pdf), 26-02-'13;*

The turbulence intensity is related to the stability of the wake. Zong & Nepf [2012] found for different values of the canopy density[1] of an emerged patch decreased values of the turbulence intensity for increased wake stability. In the case of bed mobility, an increase in wake stability means a decrease in erosion or likewise an increase in sedimentation. This is probably also the reason why patches of vegetation expand predominately in streamwise direction and thereby lengthen the patch (Sand-Jensen & Madsen, 1992), (Chen et al., 2012).
Although single patches of salt marshes (Figure 2d) do not necessarily create favorable conditions for expansion, the wake structure is playing a dominant role in the development of salt marshes (Wesenbeeck et al., 2007). On their part, the salt marshes, who are positioned at the intertidal environments, are the transition between water and land and play therefore an important role in the management of the coastal zone. However, a clear understanding of the response of patches on the hydro- and morphodynamics is still lacking which is necessary for instance for the prediction of the response of salt marshes to human interference in a coastal system.

In river flow, a geometrical discontinuity in an unconfined river can result in the development of braiding (Yalin, 1992) in which the channel is being split into multiple channels. Between those channels a bar emerges of which an island might evolve due to the combined effect of deposition of sediments and the lowering of the water level (Figure 2f). Due to the elevated position compared to the two channels and the coarser material present, the bar is able to alter the velocity profiles resulting in a wake region behind the bar.
Besides the field of sediments, knowledge of the flow structures can be used for predictions in the fields related to the dispersion of pollution and nutrients (e.g Fig. 2b), optimizing the predictions for discharges (Fig 2a) and the roughness patch as aid for the control of a wake (Fig 2c). The latter has been examined by Negretti et al. [2005], where data showed an increase in stability of an unstable wake by making use of a roughness patch at a specified location. Despite the successful increase of the stability, the increase of Reynolds shear stresses downstream of the roughness patch indicate the development of a wake behind this roughness patch.
Roughness changes in shallow flows are not limited to water flows. In the presence of large horizontal length scales, the atmospheric boundary layer behaves similar as shallow water flows. An example of a change in surface roughness is the transition of a rain forest to a palm oil plantation (Figure 2e). But the application of a surface roughness patch is more generic and extents to structures as cities, land-sea transition and differences in land use. An accurate representation of these flow structures is of importance for meteorological purposes.

Simulations of the geophysical flows as in Figure 2 are based on quasi two-dimensional models which have been adjusted to include dominant three-dimensional effects to a certain extent. For the submerged roughness patch as described previously, it is uncertain to what extent the present literature can describe the wake structure since it is unknown how dominant the three-dimensional mechanisms will be. This makes it necessary to understand the flow regime in the case of a roughness patch.

[1] A canopy is defined here as a structure consisting of multiple similar elements as a forest or the branches of a tree, see e.g. Figure 1 a,c,e.

1.1.2. Problem definition

Wake flow caused by differences in roughness can cause three dimensional structures which might be of significant importance for the flow structure. In two dimensional cases, i.e. emergent structures in shallow flows, these structures are not taken into account by current modelling approaches. The presence of three dimensional turbulent structures can cause transfer of mass, momentum and turbulent kinetic energy which has for instance consequences for the sediment transport in water flows. This study is initiated to reveal the three dimensional structures in the wake of a roughness patch (Figure 3). Specifically, can the three-dimensional wake flows be treated as two-dimensional?

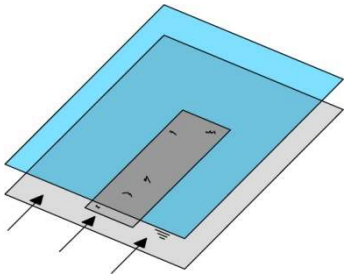

Figure 3; Schematic overview of a freestanding roughness patch.

To achieve this objective, an appeal to literature is made combined with an experimental investigation. The following goals are formulated in order to achieve the objective:

1) Similarities in the characteristics of the wake are provided by literature, for instance the theoretical models for the unbounded wake (plane wake) and the bouned wake (shallow wake). Experimental data obtained can be used for comparison in order to find the similarities and differences.
2) While the previous goal is focused on literature comparison of characteristics as mean velocity profiles and Reynolds stresses, the individual influence of the different mechanisms can be overviewed by a momentum balance. Specific interest lies with the presence of a secondary circulation and its contribution to the recovery of the wake.
3) In the case the previous results show a difference between the experimental results and the two-dimensional wake as provided by literature, can the wake be characterized by a model and/or parameter?

1.2. Approach

While interest lies with the characteristics of two-dimensional wake flow, the provided background literature in chapter 2 is organized by the mechanisms to be expected in a three-dimensional wake. This will provide more insight in the possible differences with the two-dimensional wake. As the theory provided by the literature is not detailed enough to determine the final set-up of the experiment, an additional experiment has been executed with the intention of determining the parameters to be varied and the parameters to maintain constant, see chapter 3. Since the measuring device to be used has not been used before in the department, a series of quality checks has been done before the experiment.

After the post-processing of the data obtained, the flow characteristics are analyzed and compared with literature (goal 1), see chapter 4. The resulting conclusions are integrated in the analysis of the momentum balance (goal 2). In the case the flow is not sufficiently represented by the two-dimensional models provided by literature, an attempt is made for new model(s).

The outline of this report is in accordance with the approach described above.

2. Background literature

A lot of research has been done on the characteristics of the wake behind obstructions. Where models obtained for emerging canopies can be compared with porous solid obstructions, the roughness patch cannot be compared to those directly because its drag is not distributed over the whole water column.

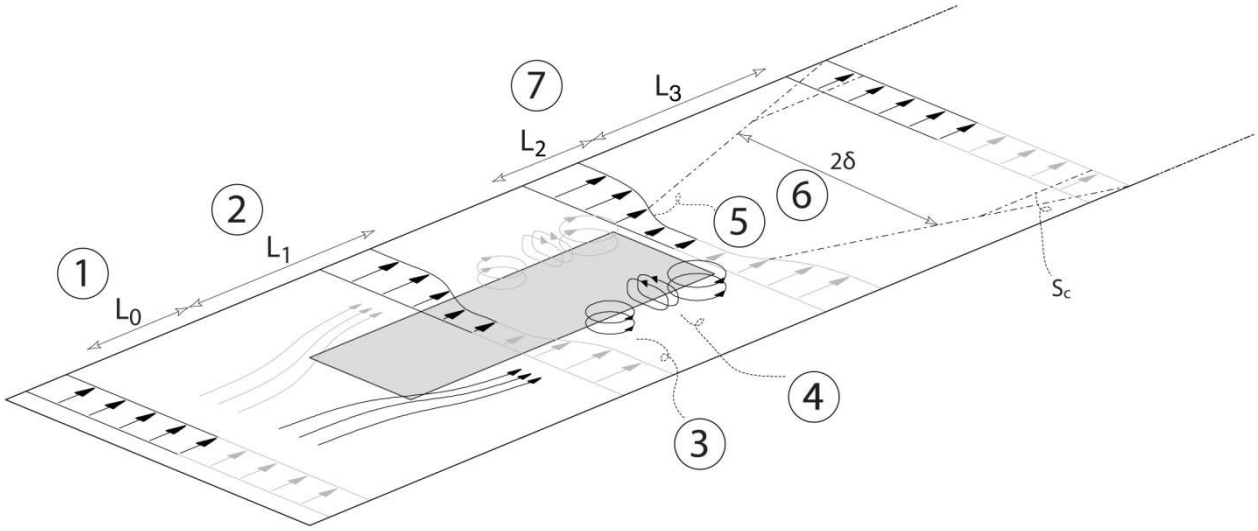

Figure 4; Overview of expected characteristics of the flow over a roughness patch. The numbers refer to the text in §2.1.

The presence of studies of canopies within the atmospheric boundary layer are numerous, for instance Belcher et al. [2003], Pendergrass & Arya [1984] and Panosfky & Townsend [1964]. However, most of them are limited to the influence of an increased surface roughness on the vertical velocity profiles above or within the canopy, representing e.g. a city or a forest.

For that reason, several components which are expected to influence the wake characteristics are being treated here in the upcoming subsections. An overview of these components is given in Figure 4**.**

2.1. Overview

1. *The upstream adaptation length* – The existence of this length is caused by the discontinuity of roughness resulting in a pressure gradient upstream of the patch. The upstream adaptation length is defined as the distance from the patch towards the location where the streamwise velocity gets disturbed. By order-of-magnitude analysis Rominger & Nepf [2011] (Figure 1e) found the adaptation length (L_0) to be proportional to the width (b) of the obstruction. The experiments showed indeed this proportionality $L_0 = (4.0 \pm 0.7)b$. The upstream deceleration is less for low flow-blockage canopies and therefore the adaptation length decreases as well. For comparison, the flow blockage decreases more drastically if we do not evaluate a canopy but a roughness patch. A rough estimation based on the results of Vermaas et al. [2011][2] would suggest an adaptation length of 2 m for a obstruction width of 2 m.

[2] The experiment by Vermaas et al. [2011] is similar to Figure 1d with a few adjustments like a developing region at the leading edge of the roughness lane.

2. *The interior adaptation length* – This length is defined as the distance needed to arrive at an equilibrium state within the patch, starting at the edge of the roughness patch. In case of a short obstruction, this equilibrium will not be reached. Many studies done on the development of a internal boundary layer after a surface roughness increase confirmed the thickness of the boundary layer to follow the ⅘th power law (e.g. Pendergrass & Arya, 1984). The proposed relation given by Pendergrass & Arya (see (1)) with z_2 to be the effective roughness height and h the internal boundary layer thickness, does not hold in every situation.

$$\frac{h}{z_2} = 0.35 \left(\frac{x}{z_2}\right)^{0.8} \quad \textbf{(1)}$$

Applying the relation on the data given by Rominger & Nepf [2011], by making use of the volume fraction to estimate the effective roughness, the length estimation becomes of the same order as shown by the data. However, using the relation to estimate the adaptation length for the experiments done by Vermaas et al. [2011] the results are significantly smaller.
By means of an order-of-magnitude analysis, Rominger & Nepf [2011] (Figure 1e) found a model for the estimation of the interior adaptation length. For low-blockage canopies, this relation is given by:

$$L_1 \approx \frac{2}{C_D\, a} \quad \textbf{(2)}$$

Where 'a' is the frontal surface area of the obstruction per unit volume, and C_D the drag coefficient for an array, usually set equal to one. The translation of the relation to non-canopy roughness elements is difficult because it is a generalized relation for canopies.
However, the frontal surface area per unit volume can be estimated by means of a typical length scale of the individual roughness elements 'k' which will result in 'a' being proportional to 1/h where h is the water depth. This leads to the interior adaptation length above the roughness patch being proportional to the water depth. Similar is found if the adaptation length is interpreted as the length needed for an eddy to adapt to the new boundary condition, i.e. the product of the eddy lifetime and the speed of the adaptation. The first is proportional to h/U_* and the latter proportional to U_* since an increased roughness height will intensify the growth of the new boundary layer (e.g. (1)). The product of the two will show again a proportionality of the adaptation length to the waterdepth. However the results of Vermaas et al. [2011] were different based on the mass redistribution in which a decrease in waterdepth results in an increase of the adaption length.
A different approach for the quantification of the adaptation length above the roughness patch is based on its definition. If a new equilibrium is obtained above the patch the local transverse mass flow will be absent, implying the total transverse mass flow at the boundaries of the patch being equal to the mass deficit above the roughness patch at $x=L_1$ (see (3)).

$$2\int_{x=0}^{L_1} h\overline{V_b}dx = hD\overline{U_\infty} - \left[\int_{y=-\frac{1}{2}D}^{\frac{1}{2}D} h\overline{U}dy\right]_{x=L_1} \quad \textbf{(3)}$$

In (3) the overbar represents the depth averaged value of the velocity component, D is the width of the patch, V_b is the transverse velocity at the boundary of the patch and U_∞ is the streamwise velocity at $y=\infty$. The LHS of (3) represents the transverse mass flow while the RHS represents the deficit of the mass flow. If the depth averaged transverse velocity is assumed to be varying

linearly with x, where at x=0 (the leading edge of the patch) $V_b=V_0$ and the streamwise velocity above the patch is assumed to be constant in y quantified by the centerline velocity U_c, the following relation is found:

$$L_1 \propto \frac{D(U_{\infty -} U_c)}{V_0} \quad \textbf{(4)}$$

The relation as shown in (5) is similar to the normalization used in Vermaas et al. [2011] to suggest self-similar behavior for the transverse velocity profiles.

3. *Vortices* – The horizontal vortices, as shown by Rominger & Nepf [2011], evolve around the parallel-edge of the patch after a shear layer has been formed (Kelvin-Helmholtz instabilities), which occurs after the interior adaptation length. In the case of emerged rectangular obstructions, large scale turbulence weakens the instability of the wake behind the obstruction. As published by Nakamura & Ohya [1984], the large scale structures reduce the spanwise correlation of the streamwise velocity component. For porous obstructions, the opposite is true. The study of Rominger & Nepf [2011] demonstrates the interaction between the coherent structures on the parallel edges of the patch. If the patch is wide enough, the spanwise correlation vanishes. If the width becomes too small with respect to the penetration length scale of the vortices, the data shows an increase in the strength of the vortices with respect to the case without communication[3]. The self-organization of the vortices causes an increase in instability of the wake.
4. *Secondary current* – It was found by Hinze [1967] that secondary currents are present in case of transverse roughness changes. He demonstrated the occurrence of downflow over the rough bed and upflow over the smooth bed. The secondary currents are induced by the anisotropy of turbulence, which occur in non-uniformity of geometry and/or surface roughness (e.g. Tominaga et al., 1989). An important feature of secondary currents in shallow flows is the inability of the structure to grow due to limited depth. In the case of a compound channel, the secondary current transports momentum from the main channel to the floodplain (Tominaga & Nezu, 1991). Like the large coherent structures without communication, the streamwise velocity gradients in transverse orientation decrease due to the secondary currents if it can be assumed similar trends will occur as in cellular secondary flow (Wang & Cheng, 2005) where the transfer of high momentum towards the rough lanes causes the depth averaged velocity to be greater above rough lanes compared to the smooth lanes[4]. As will be shown by the stability parameter this gradient weakening effect will have a stabilizing influence on the wake.
   Due to the downflow above the rough bed, it will experience additional shear stresses (Nezu & Nakagawa, 1993; Rodríguez & Garcia, 2008). If secondary currents are present and are being advected for at least a short distance behind the patch, these additional stresses due to secondary currents are unfavorable for the extension of the roughness patch.
   For a more theoretical approach of the existence of secondary currents, the reader is referred to Appendix A.

[3] To prevent communication, a splitter plate has been placed at the centerline of the canopy (Rominger & Nepf [2011]).

[4] If secondary currents are strong enough, they can modify the streamwise velocity profile (e.g. Wang & Cheng [2005]), if not strong enough, a logarithmic profile can still be used in further analyses (e.g. Rodríguez & Garcia [2008]).

5. *Self-similarity solution* – The basic understandings of wake flow starts with the introduction of a concept named self-similarity (or self-preservation). In free shear flows, i.e. unconfined flows in which turbulence arises because of mean-velocity differences (e.g. (Pope, 2000)), the transverse distribution of certain quantities are different in the absolute sense in downstream direction but do show often a similar shape (Townsend, 1976). Under ideal conditions, it can be shown mathematically that a quantity can be made independent of the downstream direction by normalization of the quantity with flow characteristic values, meaning self-similarity.
   For the turbulent wake, the velocity defect ($U_\infty - U$) is made self-similar by normalization with the velocity defect at the centerline of the wake (U_c). The transverse distance y is normalized by the wake half width (l), defined as the distance from the centerline to the position where the velocity deficit is half the centerline velocity deficit (Figure 5).
   The solutions show an exponential relation for the velocity deficit and the Reynolds shear stress (e.g. Pope (2000), p. 147). These relations have been confirmed by experiments (Figure 6), for instance Wygnanski et al. [1986].
   The introduction of a boundary and thereby limiting the depth of the flow, results in a non-uniform distribution of the quantities over the vertical. Meaning it is not necessarily true for the shallow turbulent wake to be self-similar as well.
   Despite this non-uniformity, data published by Balachander & Tachie [2001] shows an indication of self-similarity of the mean velocity profiles for a wake behind a rectangular obstruction. This only holds for profiles in the far wake (with relative downstream distance x/D=5). Carmer [2005] extends the observation by showing self-similarity of the far wake independent of its stability. In the case of an emerged obstacle, the obstruction exerts a drag force on the flow. In terms of a momentum balance, the roughness patch in the present study can be schematized as a sink as well, which explains the expectancy of self-similarity in the far wake in this experiment as well.
   Though the shapes coincide in the far field for bounded and unbounded turbulent wakes, the current study focuses on both the near field and the far field of the wake. The velocity deficit distributions in the near field presented by Carmer [2005] shows two clear deviations from the self-similarity solution. The first is the flat peak for small values of x/D, the second is the overestimation of the velocity deficit near the edges of the wake. Experimental data shows larger gradients near these edges and even a possible second inflection point. Although self-similarity in the far wake is to be expected, the near field might depict different characteristics compared to the shallow turbulent wake behind an emerged object. The roughness patch has got a longer time span for redistributing the mass along the patch, secondly if secondary currents are present, the initial transverse profiles will be distorted in a different way.

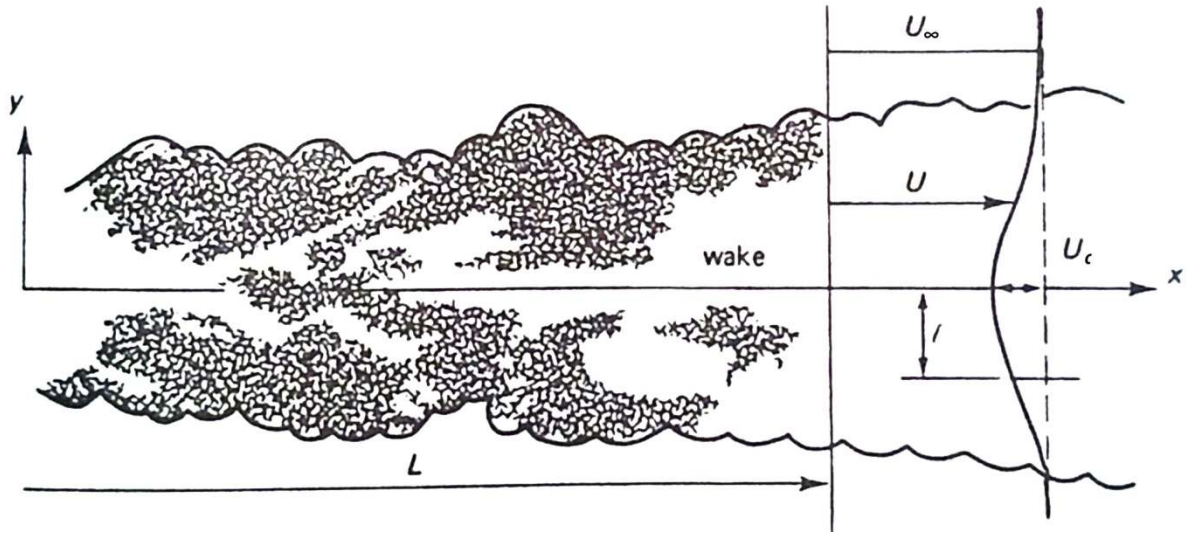

Figure 5; Definition sketch of the plane turbulent wake (Tennekes & Lumley, 1972).

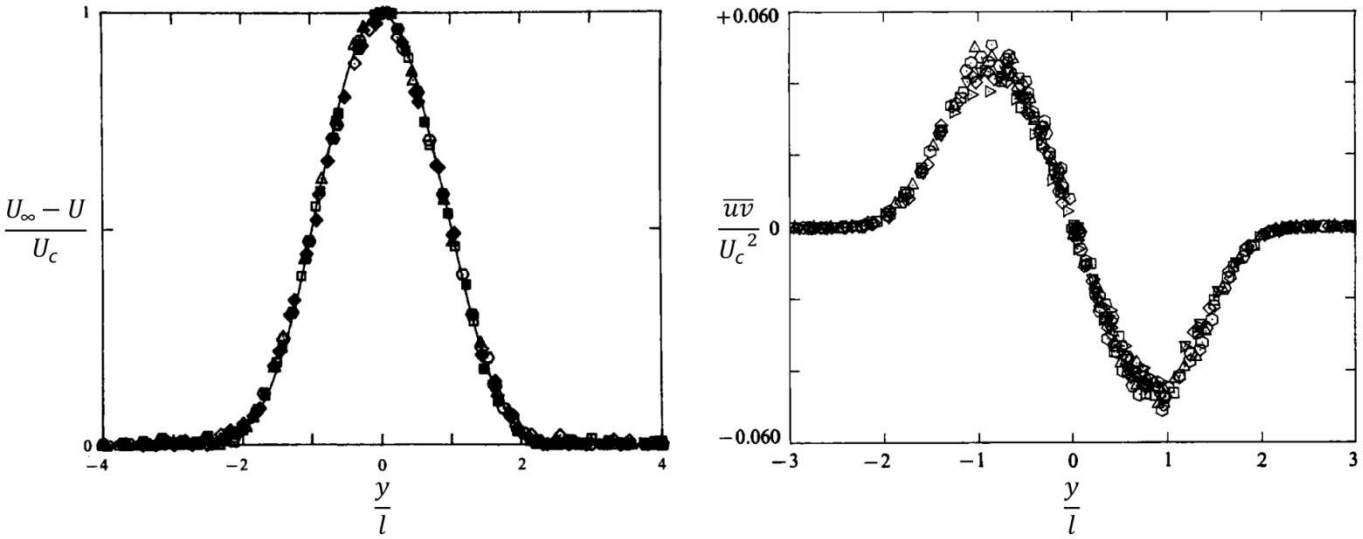

Figure 6; Left) self-similar mean velocity profile of a wake behind a cylinder; Right) self-similar mean shear stress profile of an airfoil wake; taken from Wygnanski et al. (1986).

6. *Stability parameter* – A practical parameter quantified by experiments but with clear physical interpretation is the stability parameter 'S'. In the definition of shallow turbulent wakes, where the width of the wake is twice the wake half width, the width must exceed the water depth (2 δ >> h). The behavior of shallow turbulent wakes depends on the interaction of two forcing mechanisms, the vertical shear layer induced by bottom friction and the horizontal shear layers induced (generally) by the obstruction (Carmer, 2005). For a summary of the complete derivation, the reader is referred to Appendix B.
   The stability parameter is now defined as the ratio of the bottom friction induced dissipation (F) and the production of kinetic energy to the transverse motion (P) (Chu et al., 1991).
   From the equation for the kinetic energy of the large-scale transverse motions follows:

$$S_f = \frac{F}{P} = \frac{2\langle u'^2\rangle + \langle v'^2\rangle}{-\langle u'v'\rangle}\left(\frac{C_f}{2h}\frac{U}{U_y}\right) \quad \textbf{(5)}$$

   Where u' and v' represent the velocity fluctuations with respect to the local average velocity. For F ≥ P (i.e. S ≥ 1) the transverse motion would be suppressed and the wake will be stable. This stability criterion is referred to as S_c, the critical value of the stability parameter. Chu et al. [1991] used models for the estimation of the first term on the right hand side in terms of a constant. Resulting in an stability parameter which is more easy to handle:

$$S = \left(\frac{C_f}{2h}\frac{U}{U_y}\right) \quad \textbf{(6)}$$

   The constant is left out of the definition, and therefore the critical value is not equal to one anymore. The velocity component U and the velocity gradient U_y are defined at the inflexion point of the transverse profile of the streamwise velocity.
   Due to the use of models for the velocity fluctuations, the critical value of stability has been changed. Based on experimental data for island wakes, Ingram & Chu [1987] found the critical stability value 'S_c' at 0.12-0.13 [5] instead of unity as mentioned before. This value is also dependent on the turbulent fluctuations. As shown by Chen & Jirka [1995], the critical stability parameter decreases when the strength of the reverse flow in the wake has been decreased by making use of a porous plate. Zong & Nepf [2012] showed a decrease in turbulence intensity for increasing canopy porosity, which suggests that the critical stability parameter for a roughness patch is different too.
7. *Wake length* – The wake length has been divided in two parts by Zong & Nepf [2012], the stable wake region 'L_2', and the wake recovery region 'L_3'. These length scales can be explained by the research done by Chen & Jirka [1995] who classified three flow regimes: the vortex street, unsteady bubble and the steady bubble.
   They characterized these regimes by different values of the stability parameter. The wake of an obstacle can be at first unstable and at any time become stable. After a certain distance, the velocity gradient in transverse direction decreases and therefore S increases up to the critical value where the wake becomes stable again. The distance from the downstream edge of the obstacle to the point where the wake becomes stable is called the wake region. The distance that is needed for the wake to reach a constant velocity is the wake recovery region. The effect of a

[5] Ingram & Chu [1987] used another definition for the stability parameter S_w, corresponding to 4 times S as defined in (6). In their paper, the critical stability parameter S_w was about 0.5.

cylinder with a changing free end (H/D)[6] on the wake region has been investigated by Park & Lee [2000], who found an increasing wake recovery region for an increasing free end. Which is in line with the expectations based on previous notions, i.e. the 'porosity' increases which will stabilize the wake. The consequence of increasing the free end is found in the length of the recovery wake, because the turbulence intensities decreases (see also Zong & Nepf, 2012).

[6] The free end in the experiments is defined as the height of the cylinder over the diameter of the cylinder where the cylinder is fully submerged. Note that the free end of a cylinder is usually defined as the height of the obstruction over the water depth.

3. Set-up experiment

3.1. Flume

The experiments have been executed in a glass flume of 19.2 m long and 3 m wide. By means of a adjustable weir (Figure 7, nr. 4) at the end of the flume, the water level can be regulated. With the support of mobile carriages the measurements can be carried out. As estimated in Schiereck [2003] a new boundary layer will reach the surface after about 30-50 times the water depth. The roughness patch has been located in the middle of the flume. The starting point for the patch has been constructed at 3.6 m after the entrance in which we assume the flow to be well developed for a water depth of the order of 10 cm. The limited length at the leading edge of the patch is the result of giving priorities to a larger area available for measurements at the wake of the patch.
The results of Vermaas [2007] suggest a patch length of 50 to 80 times the waterdepth in order to achieve a full developed mixing layer and secondary circulation for which the length of the patch has been set to 6 m long. After subtracting the space necessary for the carriages, a length behind the patch of 6 m is available for measurements.

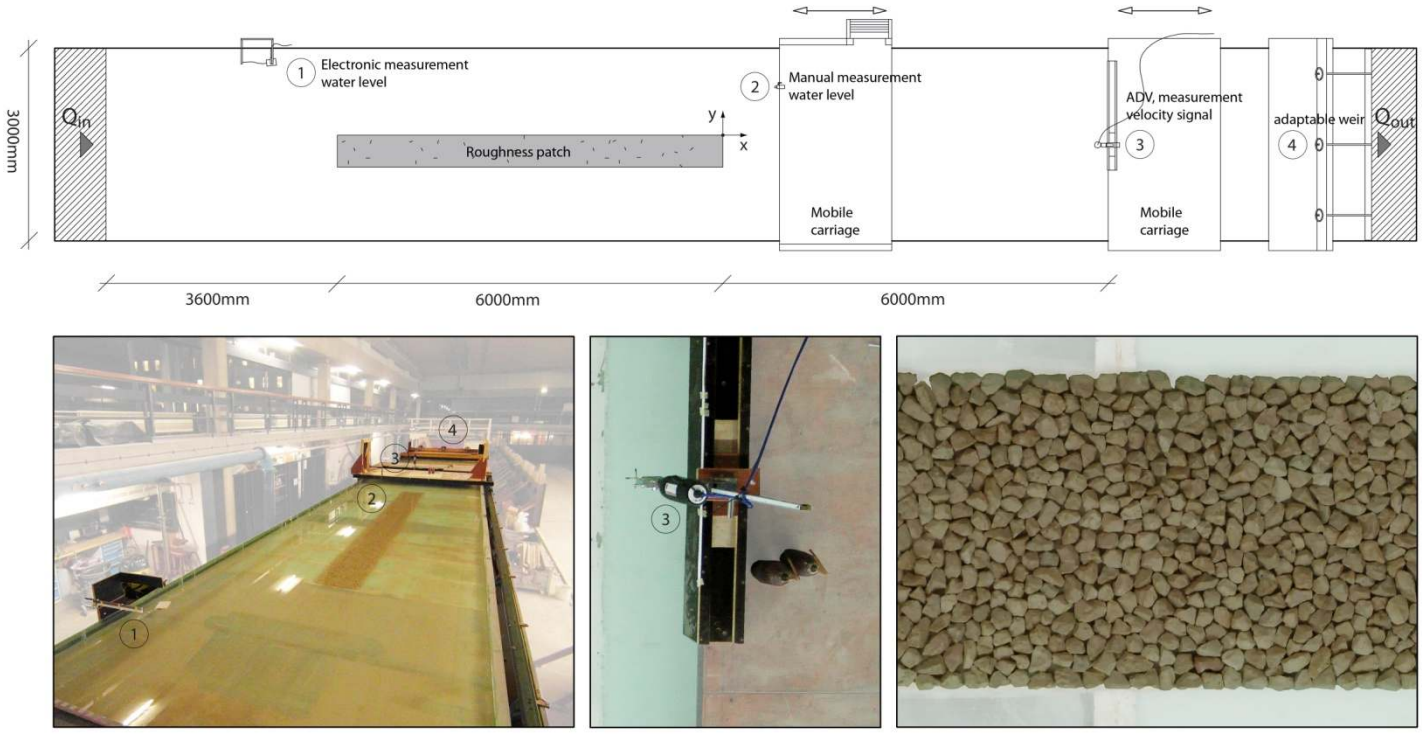

Figure 7; Schematic overview of layout experiment; 1) Electronic measurement of water level; 2) manual measurement water level; 3) ADV, 4) adaptable weir.

The individual stones used for the roughness patch needed to be large enough to create a significant velocity gradient and small enough to limit the volume occupied by the patch. Eventually stones with a nominal diameter of d_n=21 mm have been used. The stones have been positioned manually on the bottom of the flume to ensure a well packed patch. Based on a counting of the number of stones on an area of 0.5 m by 1.2 m, the packing density of the stones has been determined to be 1170 stones/m^2.

3.2. Defining the experiment

To examine the impact of a roughness patch on the characteristics of the wake, two cases will be investigated in more detail. The design of the cases is based upon literature as well as own observations[7]. For reasons of comparison, it is preferred to select the cases for a stable and unstable situation. The essence of the set-up is in deciding which variables to keep constant and likewise which to change.
An essential parameter is the stability parameter. One version of this parameter has been introduced by Wolanski et al. [1984], and is based on the same principles as the one introduced by Ingram & Chu [1987]. The latter will be used in this investigation because it is more frequently applied in literature and therefore easier to connect to.
To decide which parameters to vary, additional experiments are performed where dye visualization is used to obtain information about the influence of the parameters involved. The results are treated in §3.2.1-§3.2.4. The visualization provided are photographed just behind the patch. The flow direction as well as the dye streaks are indicated.

3.2.1. Velocity

For reasons of simplicity the stability parameter for solid emerging obstructions (as in Figure 1a) has been used and is given by $S=Cf \cdot D/h$ in which the centerline velocity in the near wake is assumed to be zero. Here the width of the obstruction is represented by D and the waterdepth by h. Besides the friction factor (for high Reynolds number weakly depending on velocity), the absence of another velocity related parameter in this expression of S suggests the shallow wake to be independent of the velocity. The results of Chen & Jirka [1995] on the wake stability show that the stability is indeed mainly determined by the width of the obstruction and the water depth. Also Jirka [2001] suggests the stability of a cylinder induced wake to be invariant of the Reynolds number for $Re_h \geq 1500$. However, based on dye visualization of own experiments (Figure 8), the strength of vortices in the

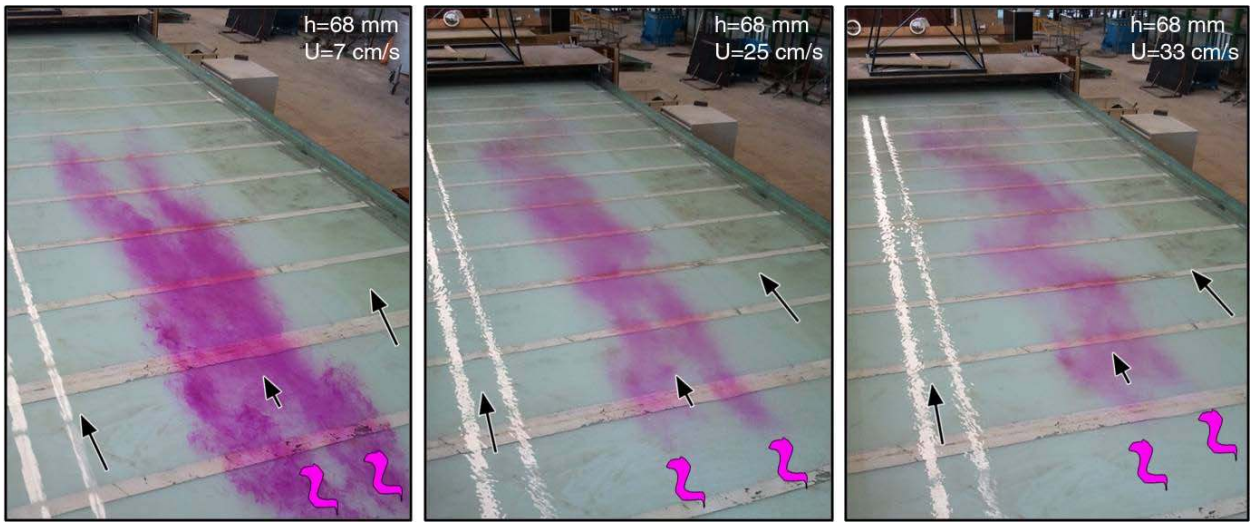

Figure 8; Dye visualization of the wake structure for changing discharge. Water depth of 68 mm and a roughness patch width of 50 cm. Left: U=7 cm/s, S=0.04; Middle: U=25 cm/s, S=0.03; Right: U=33 cm/s, S=0.03.

horizontal plane increases with increasing velocity while the stability parameter is nearly constant. The discrepancy is caused by the use of the expression for a solid emerging obstruction, in which the

[7] The influence of a roughness patch on the wake structure has been examined visually by means of dye visualization in order to determine the influence of the variables qualitatively.

centerline velocity is assumed to be an order of magnitude smaller than the ambient velocity. In the case of a roughness patch, the velocity at the centerline is often of the same order as the ambient velocity. The results imply the wake of a roughness patch not as invariant of the ambient velocity.

3.2.2. Width

The width of the patch is a variable with a large influence on the stability parameter. An increased width will cause an increase of the drag force exerted on the flow and it will increase the displaced volume as well.

Supported by data of Chen et al. [2012], the flow blockage[8] is at first sight related to the stability parameter, where recirculation zones behind the porous obstructions (as in Figure 1b) are found for higher values of the flow blockage. Meaning a high flow blockage is accompanied with a low stability parameter.

In order to keep the flow blockage and the stability parameter constant, an increased width of the patch needs to be compensated by an increased waterdepth. This scaling has been visualized in Figure 9 (left and middle) in which the width of the patch and the waterdepth have been increased 50%. In this way, the stability parameter has been kept nearly constant. The scaled cases are clearly not resulting in similar flow structures.

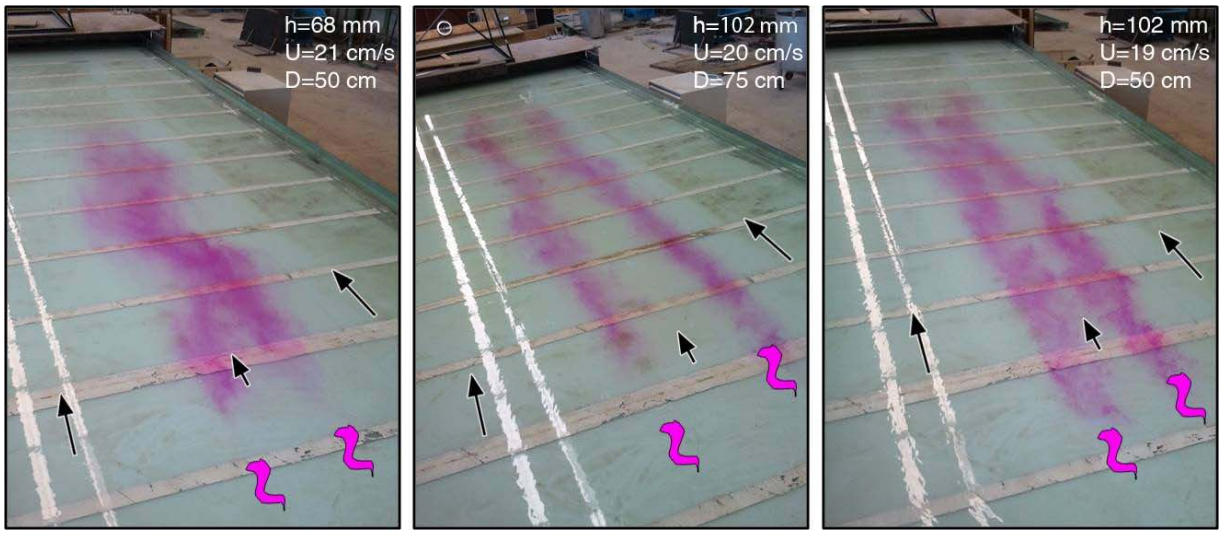

Figure 9; Dye visualization of the wake structure for a changing width of the roughness patch. Left: D=50 cm (width), h=68 mm (water depth), U=21 cm/s, S=0.03; Middle: D=75 cm, h=102 mm, U=20 cm/s, S=0.03; Right: D=50 cm, h=102 mm, U=19 cm/s, S=0.02.

3.2.3. Water depth

As Rominger & Nepf [2011] depicted, it takes some time for the shear layer to develop once the flow has reached the leading edge of the porous obstruction (as in Figure 1e) , this distance is called the interior adjustment region. Based on emergent canopies, they found the adjustment region for high flow blockage to be proportional to the width of the obstruction, where for low flow blockage, it is inversely proportional to the frontal area per volume. Belcher et al. (2003) found the same proportionality of a submerged canopy in the absence of a free surface.

The adaptation length for low blockage canopies coincides with the observed development of large structures in the current experiments. An increased waterdepth would mean a decrease in frontal area per volume concluding an increase in adaptation length. Which suggests the shear layer to be

[8] Flow blockage is in the paper of Chen et al. (2012) defined as $C_D aD$, where C_D is the drag coefficient of a single emergent cylinder, 'a' is the frontal area per volume and D is the diameter of the structure.

undeveloped before the end of the patch has been reached for larger water depths.
Based on the dye visualization shown in Figure 10 the water depth has a less significant effect on the wake structures compared to the case of changing the velocity, although velocity measurements do show significant changes. For decreasing waterdepth, the distance needed for the mixing layers to interact, decreases as well.

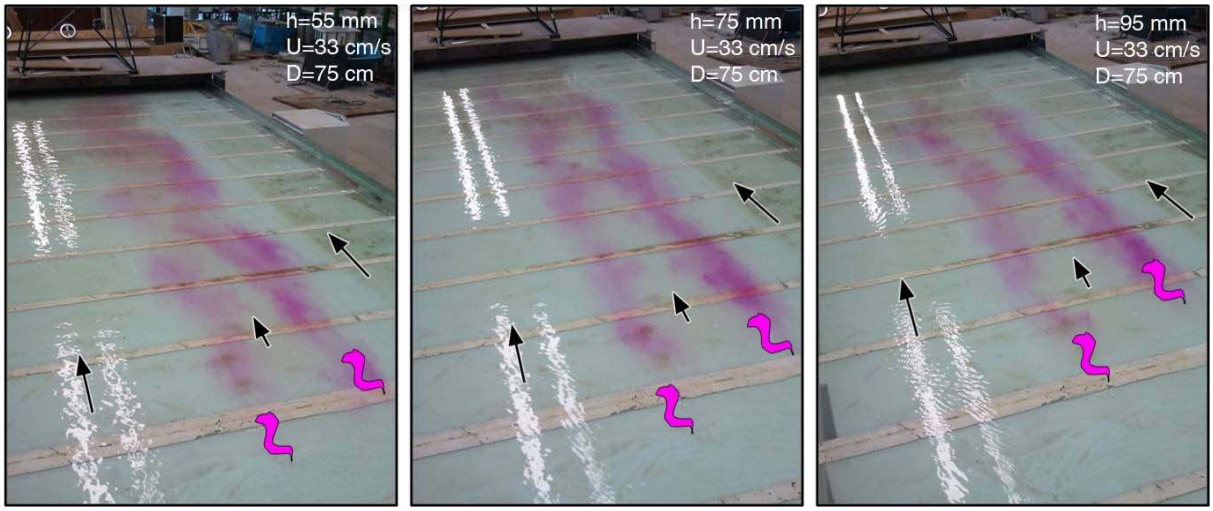

Figure 10; Dye visualization of the wake structure for changing depth. U=33 cm/s, D=75 cm. Left: h=55mm, S=0.06; Middle: h=75 mm, S=0.04; Right: h=95 mm, S=0.03.

3.2.4. Length

Within boundaries, change of the length of the roughness patch is expected to change the wake structure as well, due to the time needed for the shear layer and a possible secondary current to develop. Vermaas [2007] estimates the distance for the vortices in the horizontal plane to fully develop at 50 times the water depth and for the secondary current about 80 times. For a few different water depths, the influence of shortening the length of the patch has been visualized by means of dye, here 71 respectively 54 times the water depth. Although the influence seems to be limited it looks like large structures become more pronounced for an increased patch length (Figure 11).

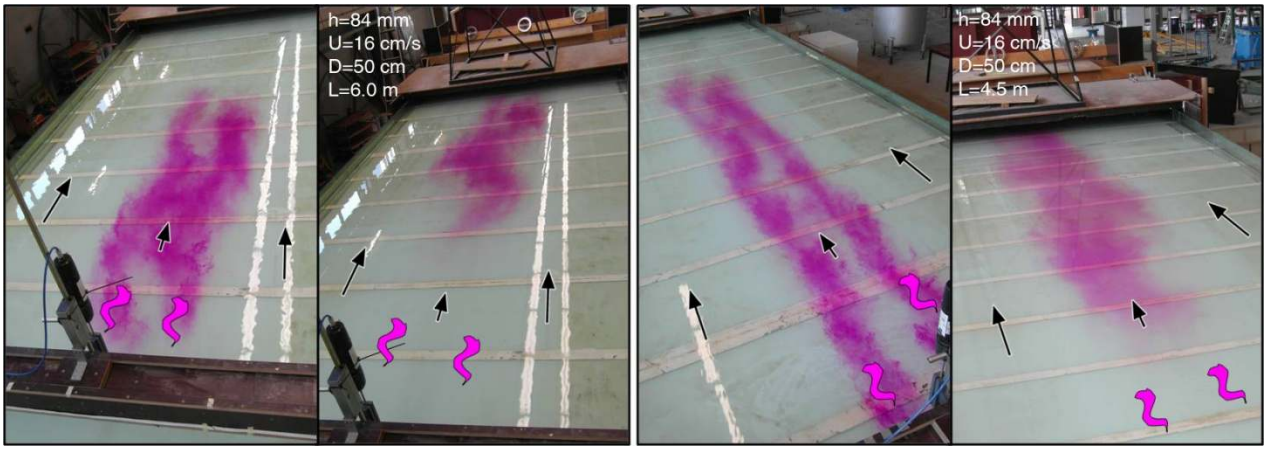

Figure 11; Dye visualization of the wake structure for changing length of the roughness patch. D=50 cm, h=84 mm, U=16 cm/s. Left: L=6.0 m (length patch). Right: L=4.5 m. The right photo of each case is taken further downstream with respect to the left photo.

3.2.5. Choices made for the experimental parameters

It was preferred to realize and investigate a stable and unstable wake. As will be depicted in §3.3, an ADV will be used as the measuring device for velocity signals. The disadvantage is however a limited measuring range of which the upper 4 cm of the water column cannot be measured. Based on this disadvantage combined with the failed scaling as in §3.2.2, it has been decided to get as close as possible to the unstable situation where sufficient measurements can be obtained by the ADV. Hence the water depth and the ambient velocity are the two parameters to vary during the experiments. The ADV used cannot measure a velocity signal in the upper 40 mm of the water column. Meaning no sufficient amount of measurement points are available for the cases where an unstable wake has been visualized i.e. at a waterdepth of 60 to 70 mm. A minimum water depth of 80 mm will be used to allow measuring the wake characteristics near mid-water depth. The increase of water depths has been limited to 120 mm because flow patterns do not change significantly any more for larger depths and will result in the disadvantage of longer lengths needed for the flow to develop.

In the following part of this paper, the next references will be used:

reference	waterdepth	discharge	ambient velocity	$Re = \frac{U\,h}{\upsilon}$	$Fr = \frac{U}{\sqrt{g\,h}}$	C_f	S [9]
	mm	l/s	cm/s				
h80U15	80	36	15	$12*10^3$	0.17	0.0030	0.0026
h80U25	80	60	25	$20*10^3$	0.28	0.0027	0.0018
h100U15	100	45	15	$15*10^3$	0.15	0.0028	0.0026
h100U25	100	75	25	$25*10^3$	0.25	0.0025	0.0017
h120U15	120	54	15	$18*10^3$	0.14	0.0027	0.0029
h120U25	120	90	25	$30*10^3$	0.23	0.0024	0.0022

3.3. Measurement devices

To obtain qualitative information of the flow characteristics, several measuring devices have been used. For high resolution velocity signals several measurement techniques can be used, e.g. LDA (Laser Doppler Anemometry) and ADV (Acoustic Doppler Velocimeter) which are called single point methods. The LDA and ADV have the advantage of small sampling volumes which are necessary to be able to measure the smaller turbulent structures. Although LDA has a higher temporal resolution compared to the ADV and is a non-intrusive device, the ADV is the only device available in the laboratory of which it is able to retrieve the three velocity components (x, y and z) from the data simultaneously. For the experiment the Nortek Vectrino II has been used, which is compared to the older version, Vectrino I, able to measure multiple points at once marking a 3-4 cm long profile. The major disadvantage of an ADV is the inability of measuring the velocity signals in the upper 4 cm of the water column. The absence of data in the region near the surface could have been resolved by using SPIV (Surface Particle Image Velocimetry) which would have provided flow characteristics at the surface. The latter has not been executed due to the conclusion that enough data could be obtained to draw conclusions, i.e. in all cases at least the characteristics at mid-depth have been

[9] S is defined as in (6). The values for the velocity and the velocity gradient are determined by the experimental data located 25 cm downstream of the patch.

acquired, in conjunction with the limited time left.
ADV's consist of a center point emitter and four receivers. The first is responsible for a short acoustic pulse where the receiver will capture the echo of the signal coming from particles in the flow. The change in frequency (Doppler shift) enables a conversion to velocities. To retrieve a three dimensional velocity signal, at least three receiver signals are necessary. The presence of a fourth receiver is in this experiment used to provide additional information to judge the quality of the signal. The restriction of the inability of measuring velocity signals close to the surface as mentioned earlier, is due to the need of the transmitter to be in the water. The intrusion of the ADV does disturb the flow locally but due to the fact that the volume in which the velocity signal is obtained is 4 cm below the transmitter the disturbance is negligible.

During the experiments, visualization techniques have been applied. The use of dye has been used in order to shape the experiment and has been used as an indicator of the experimental settings. A second visualization technique, with small floating particles, has been used to compare the different surface flow patterns. This has been videotaped to visualize the macro structures. Rough estimates of macro time and length scales can be obtained from these videos.

In order to keep the boundary conditions within reasonable limits, electronic measurement devices have been installed to monitor the throughput of the discharge pipe as well as the water level at the leading edge of the roughness patch. The device mounted upon the pipe was used for monitoring the discharge for the inlet of water.
An estimation of the discharge derived from the data, where the depth averaged transverse velocity profiles at the far wake have been extrapolated to the sidewalls, show an offset well below 4% of the measured discharge (with the exception of one case, 5.5%). One contributor to the offset is the extrapolation of the data towards the sidewalls. According to the estimation of the discharge it seems that the discharge measurements are within reasonable boundaries. Since the same device is used for all the cases, the presence of a systematic error of the measured discharge will be present in all the collected data.

The water level has been monitored by two independent measurement devices. One is a manual gauge able to measure within a 0.1 mm accuracy and is positioned at one of the carriages at the flume (Figure 7, nr. 2). The manual gauge has been used for the water level measurements in transverse and longitudinal direction and the calibration of the electronic gauge. At every position the bottom level and the water level have been measured with respect to a reference level, except above the roughness patch. The electronic gauge consists of a framework holding a laser, and a flat floating object on the surface. The distance between the floater and the laser is given in a to be translated signal in volts. Due to a continuously need for the electronic gauge to be calibrated if repositioned, the device has been located one meter upstream of the leading edge of the roughness patch (Figure 7, nr. 1). The gauge has only been used to check whether the boundary conditions were constant.

3.4. Pre-processing

3.4.1. ADV

The use of a profiling ADV comes with great advantages but the user needs to be aware of some challenges as well. Compared to a single point ADV, it takes a bit more time for the user to understand the pitfalls of the profiler. The manufacturer advertises with a 100Hz frequency and a profile consisting of a measuring point every millimeter resulting in 34 measuring points over 3.4 cm. Testing the device during the experiments shows that the signal quality increases for a decrease in these two settings (the sampling frequency in Hz, and the number of points to measure, related to the sampling size in mm^3). Also if both the number of points to measure and the sampling frequency is increased, the number of particles in the water needs to be increased as well. By changing the sampling frequency and sampling volume an optimum balance in settings has been chosen to continue the experiments. In addition to the required concentration of clay particles, the sampling frequency has been set to 60 Hz and the sampling size 3 mm (compared to the ~6 mm sampling size and 25 Hz for the single point ADV). For a summary of the testing see Appendix C.

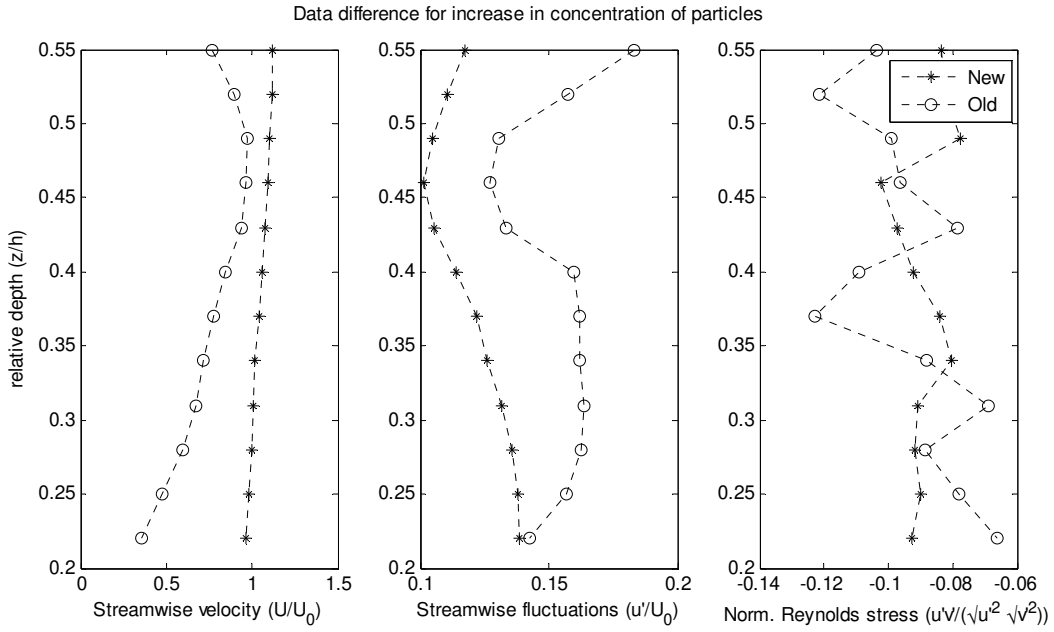

Figure 12; Difference in results due to increase in concentration of clay particles. The black crosses (*) represent the data with an increased concentration, while the open circles (o) represent the results for a low concentration. The streamwise velocity and fluctuations have been normalized by the depth averaged ambient velocity and the Reynolds stress by the product of the mean local fluctuations. The relative depth is defined as the vertical coordinate 'z' over the water depth in which the bottom is positioned at z=0.

Besides the settings itself, the ability of the ADV to measure multiple points simultaneously showed difficulties. Often the points near the edges are of low quality and needed to be dismissed. During the experiments it has been found this issue can partly be addressed to a too low concentration of particles (Figure 12). Although the increase in particles increases the quality of all characteristics, i.e. linear profiles are expected to appear[10] for all three characteristics since fully developed flow is

[10] The streamwise velocity profile is for fully developed flow logarithmic where the turbulent fluctuations show an exponential relation (Nezu & Nakagawa [1993]). However, for the given domain as in Figure 12, a logarithmic and exponential relation approach a linear profile.

assumed, an optimum point within the profile can still be found. For example see Figure 12 for the turbulent fluctuations where for z/h=0.45, a minimum is measured.

The issue of a minimum in the profile of the turbulent fluctuations has also been seen when comparing the Vectrino I and Vectrino II measurement results of Zedel & Hay [2011]. This publication does not comment this observation. Another difficulty shown without detailed comment is the misfit of the tails of the measurements. Which makes it necessary to create an overlap between measurements in order to be able to locate these tails.
Although it is uncertain to what extent the improved data contain noise, the reduction of noise is visible since noise is random and therefore uncorrelated. The right graph in Figure 12 shows a fairly linear change of the correlation. Secondly the measuring device will not measure less fluctuations in the signal than present (i.e. measurement = signal + noise) which means the whole profile of the fluctuations have improved since all measured intensities decreased.

3.4.2. Time

The duration of the individual measurements needs to be long enough in order to obtain correct time average characteristics. By keeping the boundary conditions constant the flow is considered as fully developed, meaning the flow is stationary and no upper limit needs to be considered in determining the duration.
To determine the minimum duration, the autocorrelation function in time is used in which the duration of the measurement must be much larger than the time scale of the macrostructure (comparable to the integral time scale). The maximum value for the integral time scale and time scale of the macrostructure is found for the largest waterdepth and lowest flow rate. Although the integral time scale is only in the order of a few seconds for the streamwise velocity component, the largest vortices are a magnitude larger, i.e. 10-40 sec., based on the visualizations and the autocorrelation function. For the case with the largest timescale, a duration of 100 seconds showed to be sufficient to decrease the error made due to a finite time record to 1% for the mean streamwise velocity and 2% for the turbulence intensity.

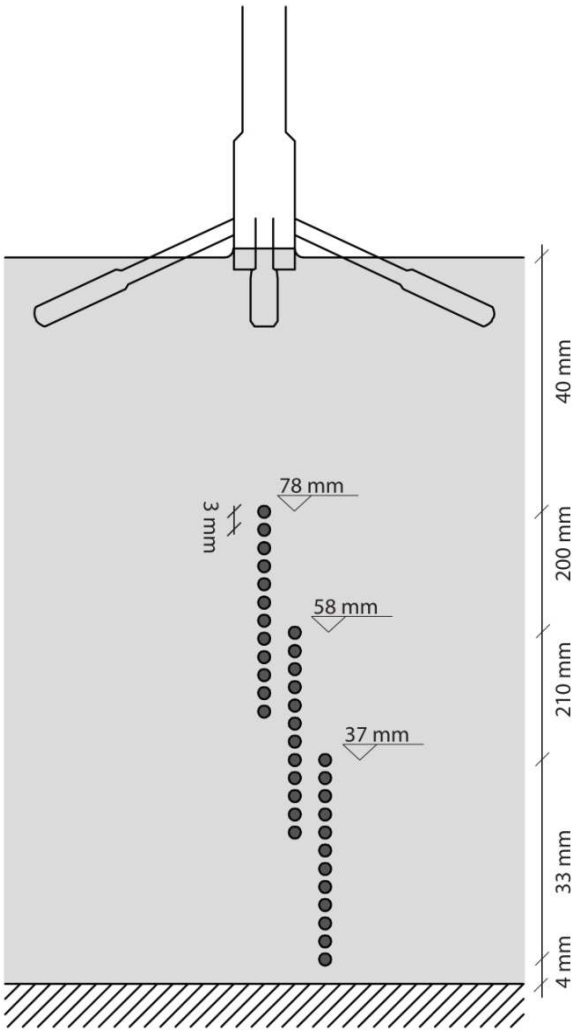

Figure 13; Measurement points in the vertical for the 120 mm waterdepth cases. Note the original measurements are all in line.

3.4.3. Location measurements

Since the edges of the measured profiles are uncertain, an overlap region has been created between the profiles. For the 120 mm waterdepth cases, three profiles on top of each other are measured (Figure 13) in order to reach a profile from mid-depth to the bottom. Same is valid for the cases of 100 mm and 80 mm waterdepth although here not three but respectively two and one measurements are executed, which means less overlap regions are created for the cases with lower waterdepth.

Due to the possibility of a secondary circulation present, the locations for measurements in transverse and longitudinal direction have been focused on nine cross sections of which the density at the near wake is higher compared to the far wake. Due to growing mixing layer which develops behind the roughness patch, the points in transverse direction become more spread over the cross section which should limit the number of measurements at one cross section to 15-20 measurements (Appendix D).
In order to get a higher resolution in the results, at the centerline as well as at the edge of the mixing layer a more dense grid has been applied.

3.5. Post-processing

3.5.1. Rotation matrix

The ADV has been placed on a rail oriented in transverse and vertical direction as shown in Figure 7 (nr. 3). Although a correction for the rotation angles do not seem to be necessary from first observations, a small pitch angle appears to be present according to the data. Due to the effect of the streamwise velocity on the transverse and vertical velocity components, a rotation matrix needs to be derived in order to correct the data.

Several techniques are available to extract the rotation matrix, one technique is based on continuity. Due to the possibility of a changing rotation matrix in transverse direction, i.e. on several positions in the transverse direction translations were possible, the carriage has to be positioned at the most downstream side of the rail.

Hence it has been chosen to perform several measurements in the absence of the roughness patch. For positions far downstream of the inlet, the flow can be considered as fully developed. For several water depths from the side walls, the log-law profile for the vertical velocity distribution holds, meaning the rotation matrix can be derived due to the principle of a zero mean vertical and lateral velocity component.

The data obtained shows an negligible roll angle and a small mean yaw angle of -0.1 degree. The pitch angle is larger than expected, with an average angle of -2.1 degrees (Figure 14 & Figure 15). The data have been obtained on five different cross sections. Although a slightly smaller pitch angle seems to be present around a transverse distance of 300 mm, the standard deviation is too large to confirm this. Therefore just one rotation matrix has been used to rotate the three dimensional vectors obtained by the ADV.

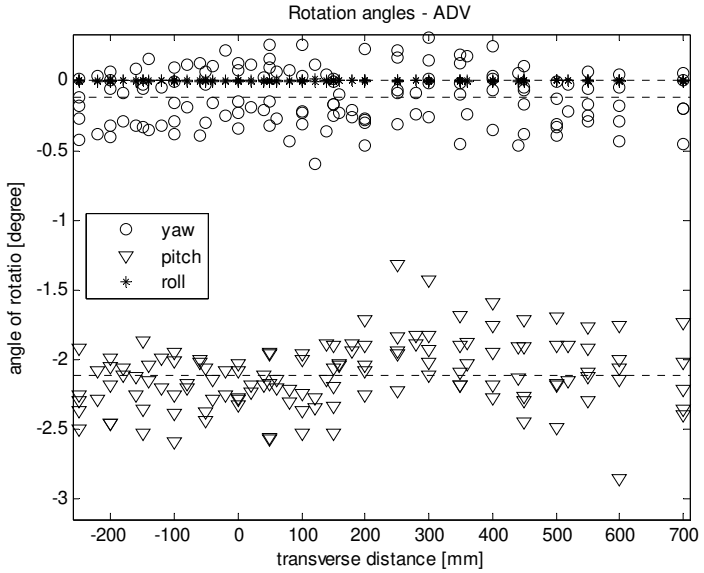

Figure 14; Rotation angles as a function of the transverse location of the ADV on the rail. No roll angle is present and the yaw angle is small but the pitch angle is significant.

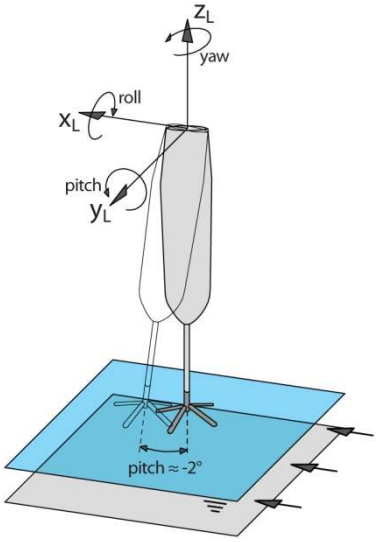

Figure 15; Definition of rotation angles; and local axis system.

3.5.2. Filter

Common in the output velocity signal of an ADV are the spikes present. These spikes are caused by the aliasing of the Doppler signal which is linked to the maximum velocity and the Nyquist frequency. Sometimes they are hard to distinguish which makes it hard to remove this 'contamination'. Several methods are available to filter the signals received. A simple filter would be using thresholds for maximum and minimum allowed velocity. The same can be done for the correlation of the signal which can be seen as a measure of the quality of the signal. Only for the correlation a threshold has been applied in which points have been discarded for correlations lower than 50%.
Due to the subjectivity necessary to obtain these thresholds, a method has been used which does not require any further input. This method is based on the three-dimensional phase space (Goring & Nikora, 2002), which uses a Poincaré map to distinguish outliers. Although various methods are available for the replacement of the spikes, it has been chosen to leave those positions empty.

As discussed in §3.4.1, the edges of the measured profiles can have a large offset. A general approach is necessary to locate the points to be discarded. The middle of the profile is considered to be accurate due to the fixed angles of the four beams with respect to the transmitter. Despite the log-law does not hold for accelerating flow together with the presence of secondary circulations, the effects of this combined effect is considered negligible in the far wake. According to the measurements done in the far wake for all cases, the last four points for the profiles close to the bottom show often strong deviations from the log-law even when the points are not in the near wall region, i.e. the buffer layer is being expected to be less than 4 mm of the wall[11]. Hence for all profiles the lower four will be left out the data analysis (see the profiles for streamwise velocity, Figure 16). Every profile has been examined individually to reassure the quality of the profiles. In several occasions more points were necessary to be discarded like the upper point of the profiles and points of which a significant amount of the data has been excluded by the filter. The threshold has been set to a 1.5% removal of the total length of the signal. On average 1% of the points in a time record has been removed for points in the near wake which is below 0.5% for in the far wake.

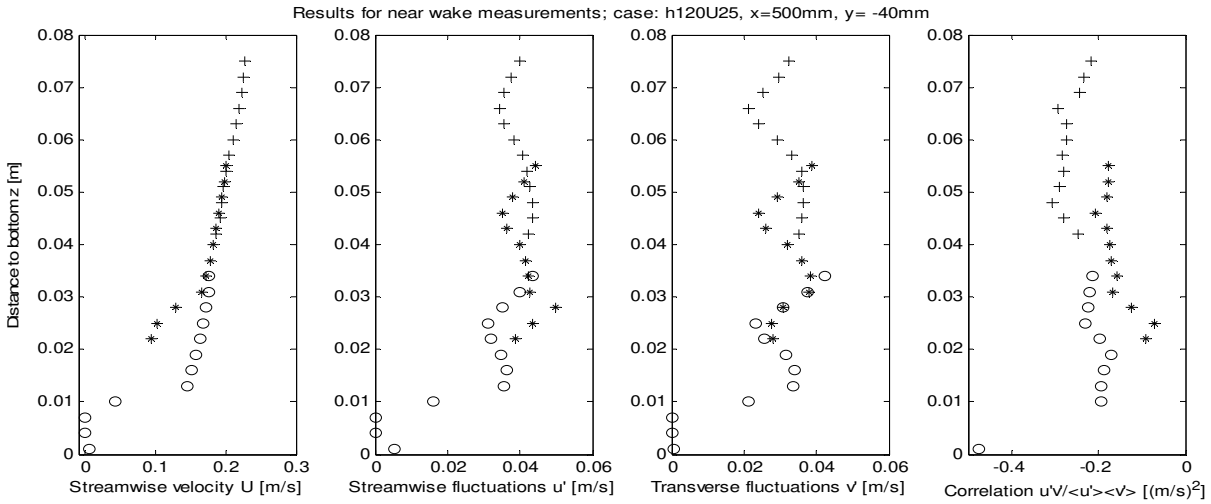

Figure 16; Four characteristics for the near wake of the case h120U25. Note all twelve points of the profile have been included. For the streamwise velocity the tails of the lower two profiles show deviations.

[11] Buffer layer is up to y^+=30. For a shear velocity of approximately 0.05 to 0.10 times the mean streamwise velocity, this results in a maximum of 4 mm off the wall.

3.5.3. Turbulent intensity.

Typical for the data obtained is a convex profile for the turbulent fluctuations (Figure 16). It's minimum is always located a little above the centre of the profile probably at the optimum of the profile. This has also been shown by Zedel & Hay [2011], where they performed measurements with the Vectrino II for an axis symmetric jet of which detailed LDA measurements are present. The results show the same convex shaped profile for the velocity fluctuations of which the minima correspond best to LDA measurements. The noise present in the signal is likely to be larger for the points further from the optimum due to the increased fluctuations. If the noise level is higher at the edges compared to the optimum just above the middle, the correlation of the two signals should decrease towards the edges, which can also be seen at the last graph of Figure 16. For further analysis of the data involving the turbulent intensity the minima described in this section will be used.

4. Results

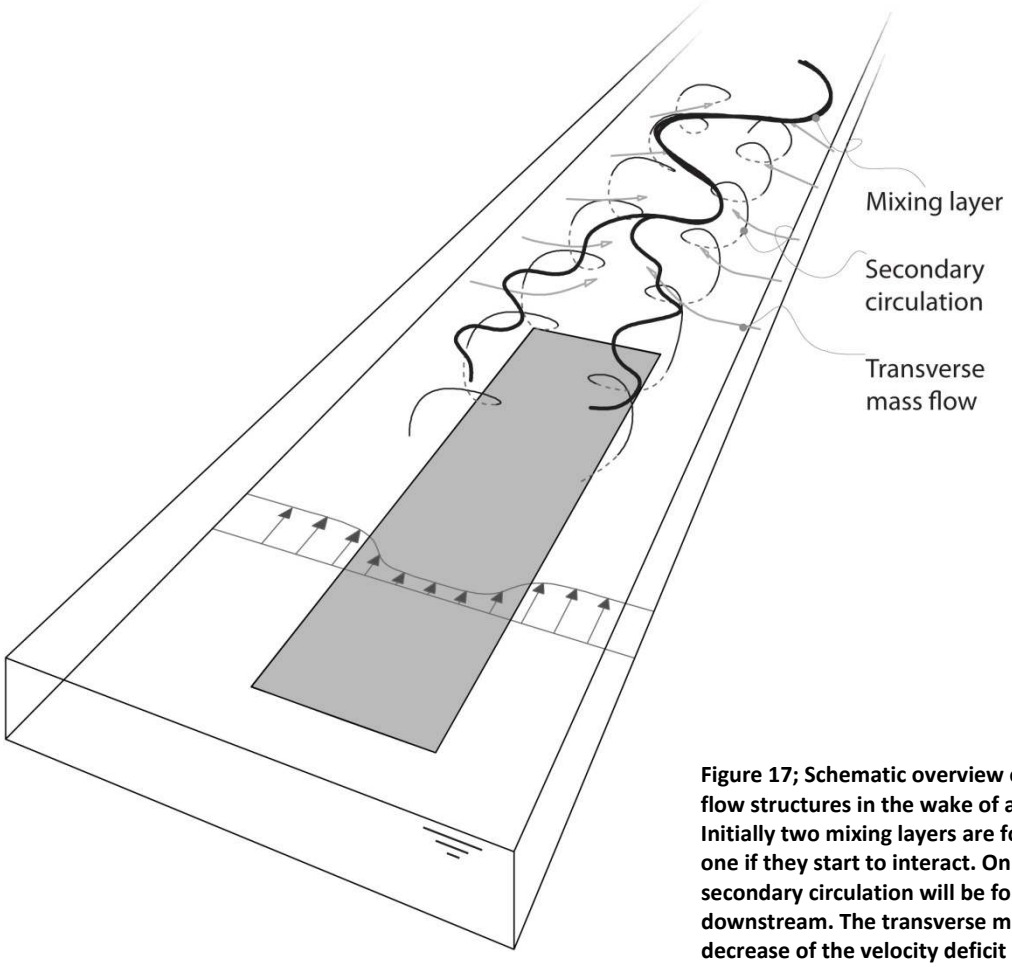

Figure 17; Schematic overview of the three dominant flow structures in the wake of a roughness patch. Initially two mixing layers are formed which becomes one if they start to interact. On both sides of the patch a secondary circulation will be formed which is advected downstream. The transverse mass flow is the result of a decrease of the velocity deficit at the patch's centerline.

In the far region of a three-dimensional wake the mixing layer (or vortices with a vertical axis), bottom friction, transverse mass flow and the advection of streamwise momentum due to the secondary circulation are assumed to determine the flow (Figure 17). In this chapter the significance of these processes will be shown for the individual element as well as its interactions.

4.1. Water level

Like velocity profiles, the water level data can provide information about the behavior of the flow structures. In this experiment, the water level at the centerline of the flume, i.e. y=-250 mm, is expected to increase in front of the leading edge of the patch and to decrease at the end of the patch due to the increase and respectively decrease of the local bottom friction. With respect to the water levels at the outer edges of the flume, a transverse pressure gradient due to the differential water levels will develop, resulting in outward flow above the roughness patch and inward flow in the wake.

The mounting stage of the electronic gauge has been positioned outside the flume in order to prevent disturbing the flow. Since the gauge was very sensitive to slight changes in its position, it has not been moved and has only been used for monitoring. Hence a manual gauge has been utilized in obtaining the water level data. The manual gauge was mounted on the mobile carriage and for each

location the thickness of the water layer was measured, i.e. water level and bottom level, due to differential bending of the carriage. It has been found that the bottom of the flume is not equal in both directions. Therefore new measurements have been performed in which a non flowing water layer was present of which it can be assumed to have a constant water level. The differences in the bottom of the flume have been subtracted from the measured water layers.
The results for the U25-cases (i.e. cases with an ambient velocity of 25 cm/s) are shown in Figure 18. The measurements are done at three different longitudinal transects, of which one is at the centerline of the flume. Above the roughness patch, the bottom level has not been measured due to the presence of the individual rocks. The data has been extrapolated for these points by means of using the same differential bottom levels as the transect at y=250 mm.

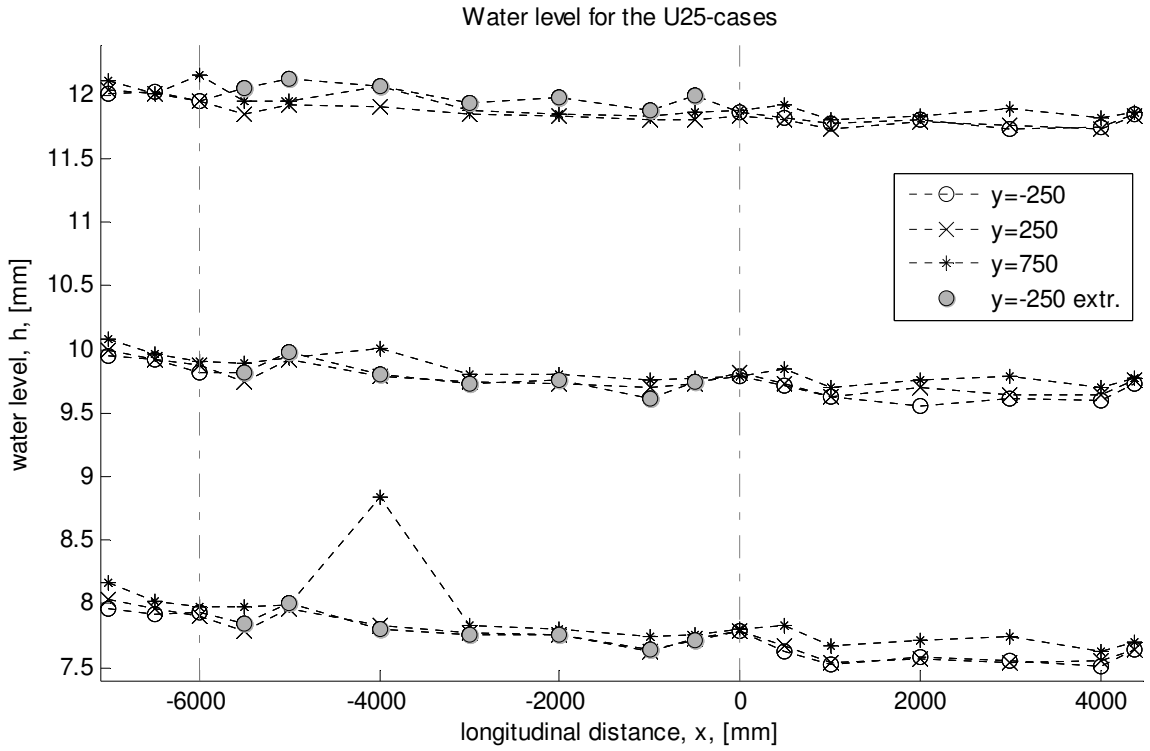

Figure 18; Water level for the U25-cases, i.e. the cases with a 120 mm, 100 mm and 80 mm water depth. At three longitudinal transect the levels have been measured. The bottom level above the roughness patch has not been measured and is extrapolated. The position of the patch is indicated by the gray dashed lines.

The data obtained for the h120U25-case corresponds to the expectations, in which we see a slight increase of the water level due to the increased roughness at the patch centerline and a slight decrease behind the patch. This cannot be seen for the other two cases in which the water level as shown in Figure 18, is always below the water level at y=750 mm. The measurements behind the patch show resemblance for the cases in which the water level exactly at the end of the patch is approximately equal to and the water level in the wake of the patch is lower than the water level at y=750 mm. It is therefore concluded that the extrapolation based on the differential bottom level at y=250 mm is false, which can be explained if the unevenness of the flume's bottom is caused by the bending of the beams supporting the glass bottom.

Since the bottom of the flume can be assumed as horizontal on average, a water level gradient needs to be present to allow the water to flow. The flow is driven by the corresponding hydrostatic pressure gradient. When no roughness patch present, the flow can be described by the one-

dimensional depth averaged continuity and momentum equation as given by Uijttewaal & Booij [2000] (see (7)(8)), which results in a water level gradient as in (9).

$$\frac{dU_0}{dx} + \frac{U_0}{h}\frac{dh}{dx} = 0 \quad \textbf{(7)}$$

$$U_0\frac{dU_0}{dx} = -\frac{C_f}{h}U_0^2 - g\frac{dh}{dx} \quad \textbf{(8)}$$

$$\frac{dh}{dx} = -C_f\frac{1}{\frac{gh}{U_0^2} - 1} \quad \textbf{(9)}$$

For all six cases the data and the theoretical water levels are presented in Figure 19. The differential equation as in (9) has been estimated and not solved since iterative solving the equation for the h120U25 case results in an error of less than 0.1 mm at the end of the flume compared to the estimation of a constant water level gradient at the upstream boundary. For the friction coefficient

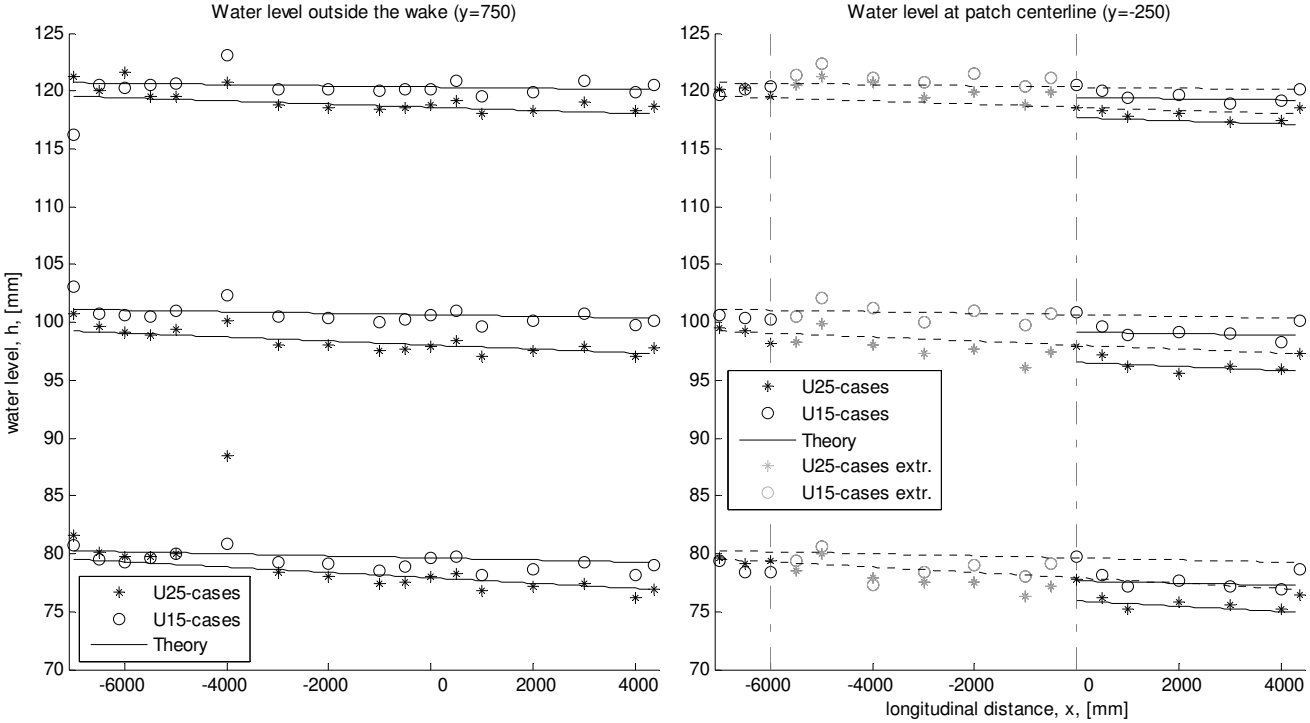

Figure 19; Water level development for all six cases. Left) the water level at y=750 mm (besides the patch); right) the water level at y=-250 mm (at the patch centerline). The solid lines represent the theoretical water level. In the right graph the solid lines have been shifted downwards. The grey markers correspond to the extrapolated points. The position of the patch is indicated by the gray dashed lines.

the Colebrook-White-equation has been used in which the coefficient is a function of the Reynolds number. Herein the bottom has been assumed to be smooth. The water level given by (9) agrees fairly to the data obtained although some outliers are still present. The water level at the centerline of the wake also corresponds to the gradient. Therefore the theoretical water level gradients are adopted in the following sections.

4.2. Transverse Profiles

The description of wake flow starts with the evolution of the transverse and longitudinal profiles. The transverse streamwise velocity profile has been measured at the end of the patch in order to obtain the initial conditions of the wake which are of importance for the stability parameter.
The change of the velocity profiles in streamwise direction are represented often in self similar formation. Not only for reasons of comparison but also for the translation of the information to models. Carmer [2005] presented the transverse profiles of the two dimensional shallow wake in self similar form and showed the profiles to be more flat at the wake centerline and the slope to be much steeper. The profiles change gradually towards the solution of the unbounded two dimensional wake. Definitions for defining the boundary between the near and far wake are typically 'a few diameters' of the obstruction. In the case of the roughness patch, the dominant structures of the flow scale with the water depth and not the width of the patch. The boundary between the near and far wake has been defined as ten times the waterdepth for the result evaluation. Besides the plane wake, other definitions for self-similarity profiles are available of which two are given in (10). Herein represents U_c the centerline velocity, U_∞represents the ambient velocity and $\delta_{1/2}$ the wake half width (determined by the velocity profiles and defined as the transverse position at which the velocity is half the sum of the centerline velocity and the maximum velocity[12]). N is a shape factor denoting the mixing layer width with respect to the wake half width, where the mixing layer width is the distance between the wake centerline and the lateral position at which U(y) becomes $0.99U_\infty$.

$$U(y) = \frac{1}{2}(U_c + U_\infty)\left[1 - \frac{U_c - U_\infty}{U_c + U_\infty} + 2\frac{U_c - U_\infty}{U_c + U_\infty}F(y)\right] \qquad \textbf{(10)}$$

$$F_{Monkewitz}(y) = sech\left(\frac{y/\delta_{1/2}}{\sinh(1)}\right)^N, \quad F_{Carmer}(y) = sech\left(y/\delta_{1/2}\right)^N$$

For the limit of N to ∞, the shape transforms to a nearly discontinuous block shape profile.
In Figure 20 the profiles at 500 mm and 3000 mm downstream from the end of the patch have been presented where the first represents the near wake profiles and the second the far wake profiles. The transverse distance has been scaled with the wake half width which is up to x=3 m approximately 0.25 m for all cases which is half the width of the roughness patch. The local velocity deficit has been normalized by the velocity deficit at the centerline. The profiles in the near wake represent similarities with the shallow wake profiles obtained by Carmer [2005] and Zong & Nepf [2012] in the case of the two dimensional shallow wake with the corresponding flatter wake center and a steeper gradient. These deviations from the self similar profiles of the plane wake can be represented by the general formulation given by Monkewitz [1988] with a shape parameter of N=4 (see (10)), although for transverse positions near the edge of the mixing layer, deviations occur and the measurements tend to the plane wake formulation.

Profiles in the far wake show similarities with the plane wake around the centerline but the results around the edges of the mixing layer become less steep as shown in the near wake as well. These deviations start around 1.5 times the wake half width ($\delta_{1/2}$) and can be fitted to the formulation given by Carmer [2005] by decreasing the shape parameter to N=1.6 (see (10)). Since the point of impact of the secondary circulation is located around 1.5 times the wake half width, the hypothesis is that the

[12] For the maximum velocity the velocity has been extrapolated to a distance close to the sidewall of the flume, in which it is assumed to be unaffected by the wake which is valid in the case of a flume of infinite size.

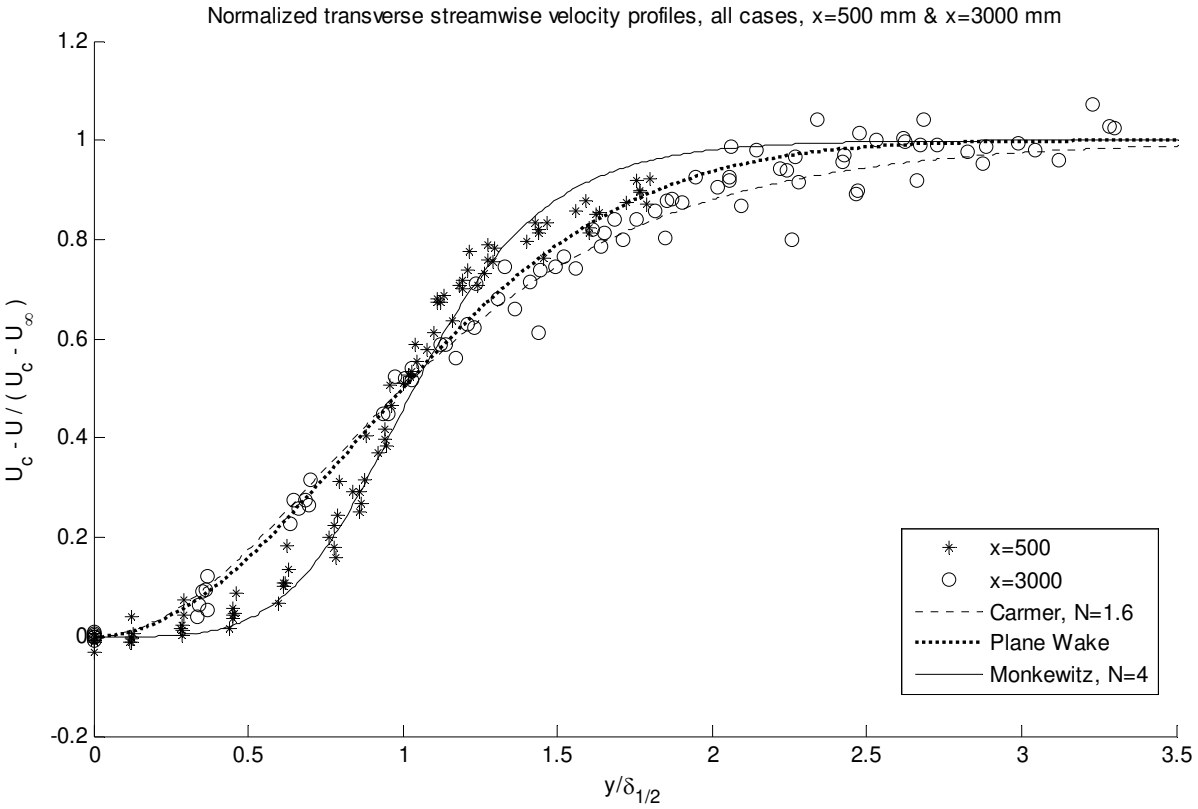

Figure 20; Transverse streamwise velocity profiles taken around half the water depth. The profiles for x=500 mm and x=3000 mm are plotted for all cases. The profiles have been normalized by the wake half width ($\delta_{1/2}$) and the minimum and maximum velocity. The self-similarity solution for the two dimensional plane wake has been included, as well as algebraic expressions with the corresponding shape factor 'N', see Monkewitz [1988] and Carmer [2005].

momentum flux caused by the secondary circulation is responsible for the flattening at the edges, which will be discussed in §4.6.

The waterdepth has an influence on the flow structures present. For example, a decreasing waterdepth will cause the relative friction above the roughness patch to increase, resulting in a larger velocity difference as an initial condition for the wake. In this case a larger velocity difference is equivalent to a larger velocity gradient resulting in an increase in the magnitude of the vortices in the horizontal plane. Therefore the influence of the waterdepth on the different processes can be seen indirectly on the mean streamwise flow field.
In Figure 21 and Figure 22 the streamwise flow field for the cases h80U25 and h120U25 are given. Note the normalization of the z-axis and that the location of the roughness patch ends at (x,y)=(0,0). The black area in the plot visualizes the lack of data due to the presence of the patch making interpolation between the points impossible. The velocity difference and gradient are larger for the shallowest case, as expected (i.e. Figure 21). Immediately behind the patch the streamwise velocity decreases due to the presence of a recirculation zone. The flow at a transverse distance larger than 300 mm is considered to be approximately undisturbed by the mixing layer although for the shallowest case the velocity starts to decrease even at the x=6000 mm cross section.
Other influences, possibly caused by the difference in water depth, are the high velocity top layer observed at the larger water depth case (Figure 21, x=-250 and 0), and the presence of a velocity gradient in the y and z direction for the deepest case between y=0 and y=100 mm. The first cannot be confirmed by the data acquired due to the difference in the relative depth. For instance, for the

h80U25 case, a top layer with higher velocity seems to be present as well at x=0.
The latter can be confirmed by the data. For this purpose the gradient can be quantified by means of transverse profiles for varying relative depth. By measuring the gradient for equal relative depth in terms of the relative transverse distance (y/h), the results show an increase in the gradient for an increase in waterdepth.
This gradient is translated in the streamwise direction where a larger vertical gradient is still visible in the cross sections further downstream whereas these gradients are absent in the shallowest case. The core of this gradient in the near wake is positioned at the same transverse coordinate as the edge of the roughness patch. It is therefore suggested that the secondary circulation and the vortices are responsible for the gradient. In §4.6 more comments will be provided on these phenomena.

The centerline characteristics are important in the sense that: it provides information about the speed of recovery of the flow; it provides scaling information i.e. the velocity deficit, valuable for modeling the flow; and the position is constant when scaled with a chosen parameter, i.e. the axis of symmetry in streamwise direction.
The characteristics at the centerline are in agreement with earlier research done on porous and non-porous obstacles in shallow water (at least for the streamwise velocity and horizontal turbulent fluctuations), by for instance Zong & Nepf [2012]. The streamwise velocity decreases immediate behind the end of the patch, which suggests that a small recirculation zone (with transverse axis) is present after which the velocity starts to increase monotonically again. After about 60 times the waterdepth the streamwise velocity at the centerline becomes fairly constant for all cases, which is about 83% of the ambient velocity for the U25 cases (Figure 23) and 80% for the U15 cases.
Although it is uncertain why the centerline velocity shows asymptotic behavior after 60 times the water depth, its behavior is not unique. Zong & Nepf [2012] (in reference Fig. 3c) show the centerline velocity to be approaching 85% of the ambient velocity for a porous patch, however no clarification is given.
A possible explanation can be obtained from the momentum balance as given in Figure 32. At the end of the flume, the mechanisms contributing to a decrease of the wake deficit all decrease (except the streamwise pressure gradient) while the bottom friction starts to increase again. As in fully developed flow driven by a (hydrostatic) pressure gradient, the pressure gradient and bottom friction are in equilibrium. Since the bottom friction at the centerline of the far wake is slowly increasing again it is suggested that this equilibrium is starting to develop. The speed of the wake recovery starts to depend solely on the difference between the streamwise pressure gradient and the bottom friction which is a slow process (see Figure 23, where the two dashed lines indicate the fast- and slow recovery of the wake).

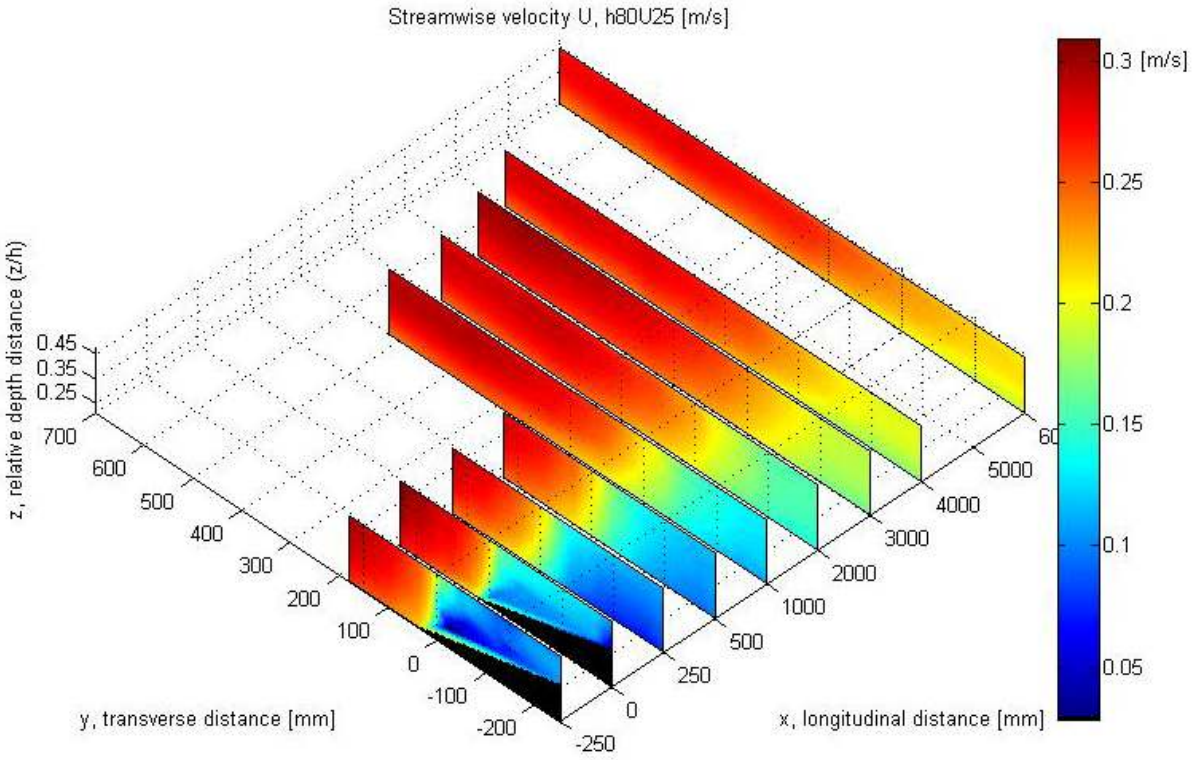

Figure 22; Streamwise velocity [m/s] at the wake for h=80 mm and U=25 cm/s. Note the scaling of the z-axis. The patch ends at x=0 and at y=0. Here no significant gradient as described for the h120U25 case is present.

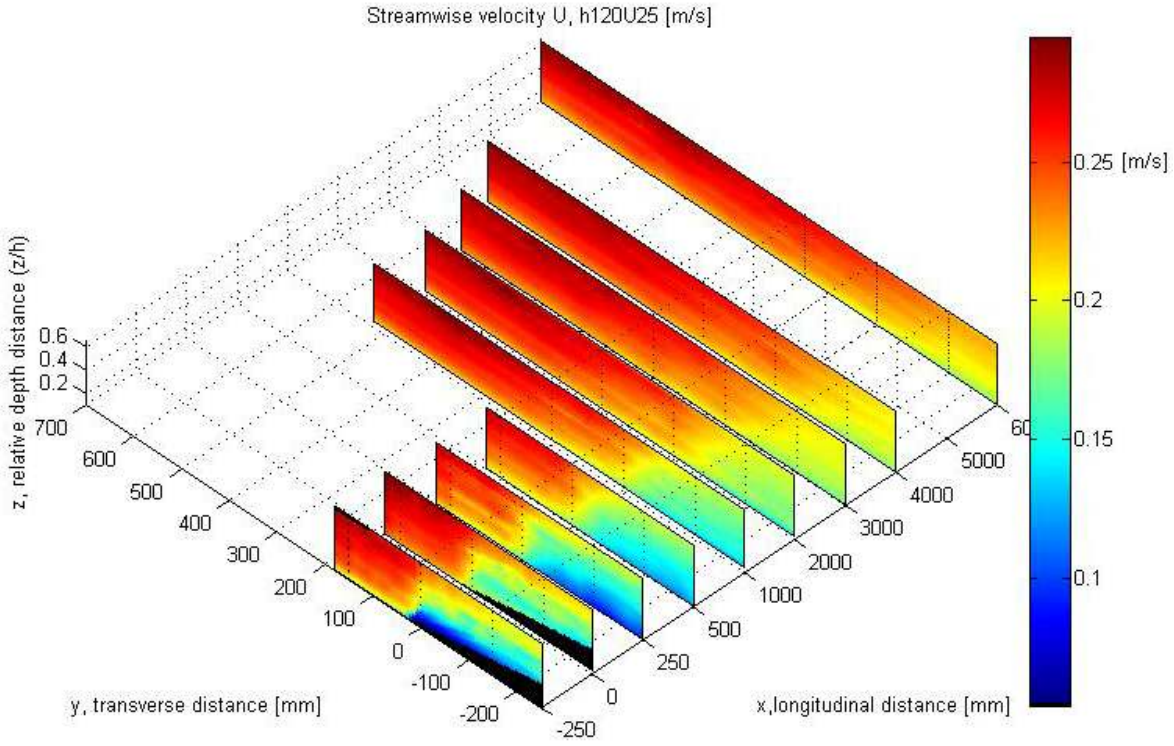

Figure 21; Streamwise velocity [m/s] at the wake for h=120 mm and U=25 cm/s. Note the scaling of the z-axis. The patch ends at x=0 and at y=0. Starting from x=500 mm, until x=3000 mm a velocity gradient in y and z direction is present (between y=0 and y=-100 mm).

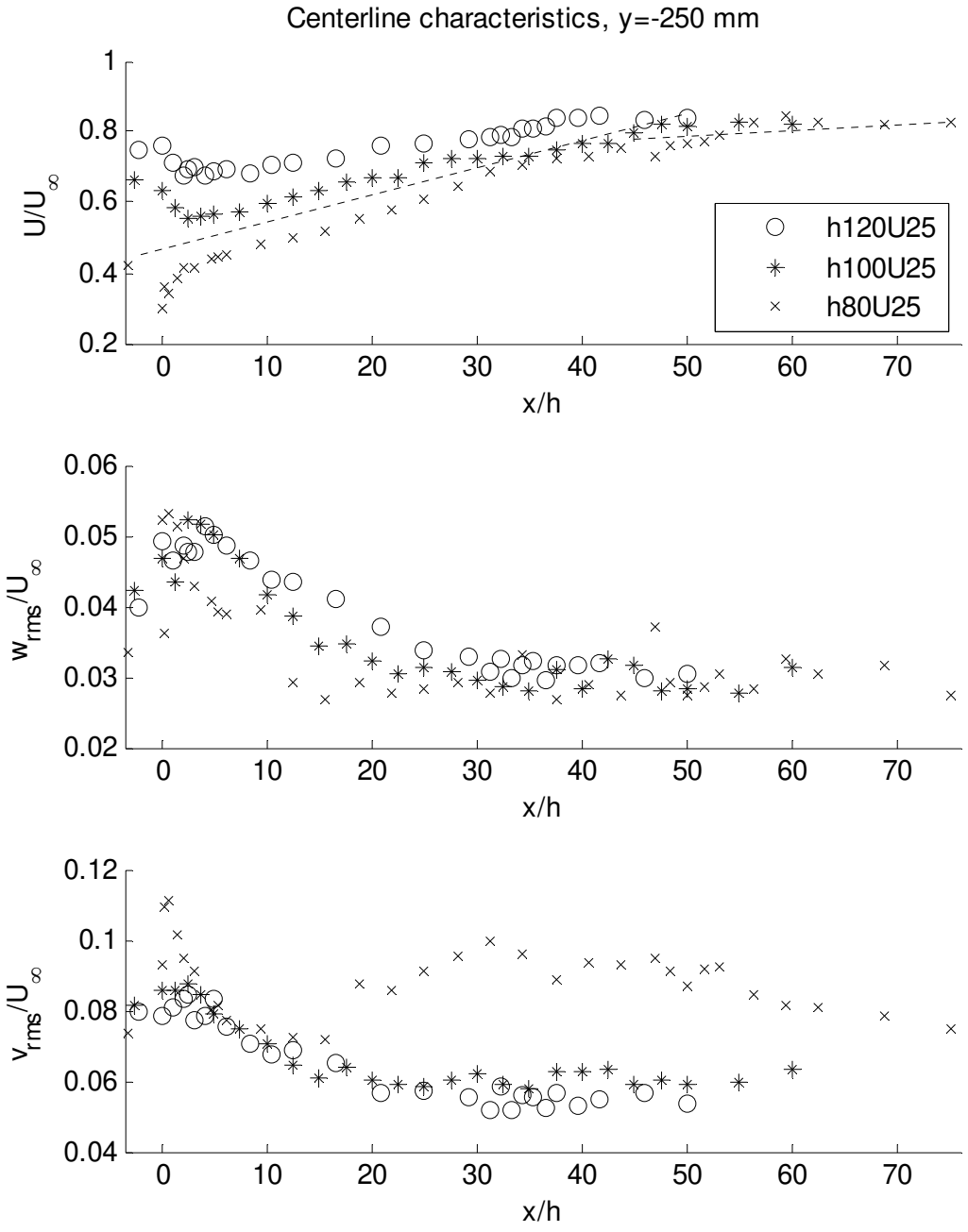

Figure 23; Centerline characteristics (streamwise velocity, vertical turbulent fluctuations and transverse turbulent fluctuations respectively) at mid-depth for the cases h80U25, h100U25 and h120U25. The streamwise turbulent fluctuations present similar behavior as the transverse turbulent fluctuations. The data has been normalized by the ambient velocity at mid-depth, the longitudinal distance has been normalized by the water depth (h). For the streamwise velocity at the centerline, a fast recovery region is visible as a slow recovery region as well.

In Figure 23 only the transverse velocity fluctuations are shown due to its resemblance with the streamwise fluctuations. The transverse turbulent fluctuations can be used as a measure for the mixing layer and has therefore been included in the figure. The short peak in the profile is present directly behind the patch caused by the individual roughness elements. Since it takes time for the two mixing layers at the side edges of the patch to develop, the intensity of the turbulence at the centerline decreases again. Due to the large velocity gradient caused by the patch for the shallowest cases, the magnitude of the developing mixing layer is greater and its growth faster. For the shallowest case the interaction between the two mixing layers occurs around 15 times the water

depth behind the patch where the transverse fluctuations at the centerline start to increase again which is confirmed by the videos recorded. For the other cases it is less clear at which point the mixing layers meet. For the cases h100U25 and h120U25 this distance is around 25 and 40 times the water depth respectively, according to the videos.
For the U15 cases, the initial velocity deficit at the centerline is lower, implying the forcing mechanism for the mixing layer to be smaller with respect to the U25 cases. Therefore the intensity of the peak seen for the shallowest case (h80U15) decreases to 8% of the ambient velocity. This is about 10% of the ambient velocity for the case h80U25 (see Figure 23).
Once the mixing layers interact, the recovery of the streamwise velocity at the centerline should increase more strongly due to the weakening of the velocity gradient by the transverse momentum transport. This cannot be concluded for the deepest cases from the data collected. Note that it is also hard to extract the point of the interaction of the mixing layers from the data whereas it can be seen for the shallowest case. For the streamwise velocity of the h80U25 case an inclination point is visible around 25 times the water depth, which is around the point where the transverse turbulent intensity reaches its maximum. Once the streamwise velocity becomes approximately 80% of the ambient velocity, the intensity of the vortices start to decrease again.
In the middle graph of Figure 23 the vertical turbulent intensity is shown. Although far downstream the intensity reaches a constant value of about 3% of the ambient velocity, the intensity in the near wake region increases with increasing water depth. This suggests that the increase is caused by the increased vertical streamwise velocity gradient as seen in the Figure 21 and Figure 22 for increasing water depth.

As mentioned in the introduction, the wake structure of an emergent canopy may provide favorable conditions for the canopy to expand in streamwise direction. However, if the roughness patch as in the experiment was positioned on a mobile bed, the patch would not necessarily have caused favorable conditions for expansion. Since the step change and the individual elements cause an increase in the turbulence intensity, the bed shear stress is elevated up to approximately 10 times the water depth for all cases (as will be further explained in §4.6 and shown in Figure 35). Further downstream the bed shear stress decreases dramatically for all cases with a width proportional to the diameter of the patch which would suggest the possibility of sediments to deposit. It is however possible that the presence of deposition further downstream alters the flow structure in the wake of the patch where it decelerates the flow at the leading edge of this deposition. Implying the patch might expand in streamwise direction after a certain period of time due to the favorable conditions caused by the deposition of sediments.

4.3. Transverse mass flux

At the leading edge of the roughness patch, flow redistribution occurs due to the increased friction at the patch, leading to mass flow from the center of the patch to the outer part of the flume. As obtained by Vermaas et al. [2011] this redistribution shows signs of self similarity when scaled with the velocity difference of the across the flow.

The data obtained in the wake of a roughness patch do not show similar behavior, with respect to the outward transverse mass flux above the patch as obtained by Vermaas et al. [2011], due to an unclear dependency on the ambient velocity which is a characteristic parameter for the velocity difference of the cross section. As shown in Figure 24, the water depth is the dominant parameter for the magnitude of the transverse velocity whereas the ambient velocity is not. The depth averaged transverse velocity has been obtained by extrapolation of the data to the surface and bottom.

The depth averaged transverse velocity has a large impact on the momentum exchange in the near wake as will be shown in §4.6, which can also be seen by the large transverse velocity in the near wake region. In the far wake these velocities are limited and the profiles as shown in Figure 24 suggest an exponential decay of the transverse velocity which will be explained below. The momentum transfer due to transverse mass flow is dominant in the near wake region with respect to the other mechanisms except bottom friction which is of the same order of magnitude (Figure 31, see §4.6). Initially the momentum loss due to bottom friction in the near wake is neglected which implies the increase in momentum in the near wake at the centerline is caused by the transverse mass flow. On the other hand the transverse mass flow will decrease for decreasing velocity deficit. In other words, an expression for the transverse velocity can be written in the form of a first order linear ordinary differential equation.

$$\frac{dV}{dx} = C_1 V \tag{11}$$

In which C_1 [1/m] is assumed to correct for neglecting the bottom friction. By integration of the equation with respect to x we find the expression:

$$V(x) = C_2 e^{c_1 x} \tag{12}$$

In which the coefficient C_2 [m/s] regulates the magnitude of the transverse velocity and is characterized by the transverse velocity V_0 at x/h=0. As shown in Figure 24, V_0 is -0.055·U_∞, -0.047·U_∞ and -0.037·U_∞ for the h80-, h100- and h120-cases respectively. Since the velocity deficit is the determining parameter for the transverse mass flow, the transverse mass flow at x/h=0 is suggested to be a function of k/h in which k is the relative roughness height of the patch. A decreasing water depth would result in an increasing transverse mass flow. Based on the curve fits presented in Figure 24, $C_2 = V_0 \approx -0.225\frac{k}{h}U_\infty$.

The first coefficient C_1 determines the gradient at which the transverse mass flow decreases in magnitude. The dimension of C_1 is [1/m] implying it is determined by a characteristic length scale. Equivalent to the proposed adaptation length of the flow at the leading edge of the patch as in (4), the derivation can be applied on the extend of the transverse mass flow in the wake of the patch. Since C_1 is proportional to the inverse of a length scale, the following is proposed:

$$C_1 \propto \frac{-0.225}{D}\frac{k}{h}\frac{U_\infty}{U_\infty - U_c} \tag{13}$$

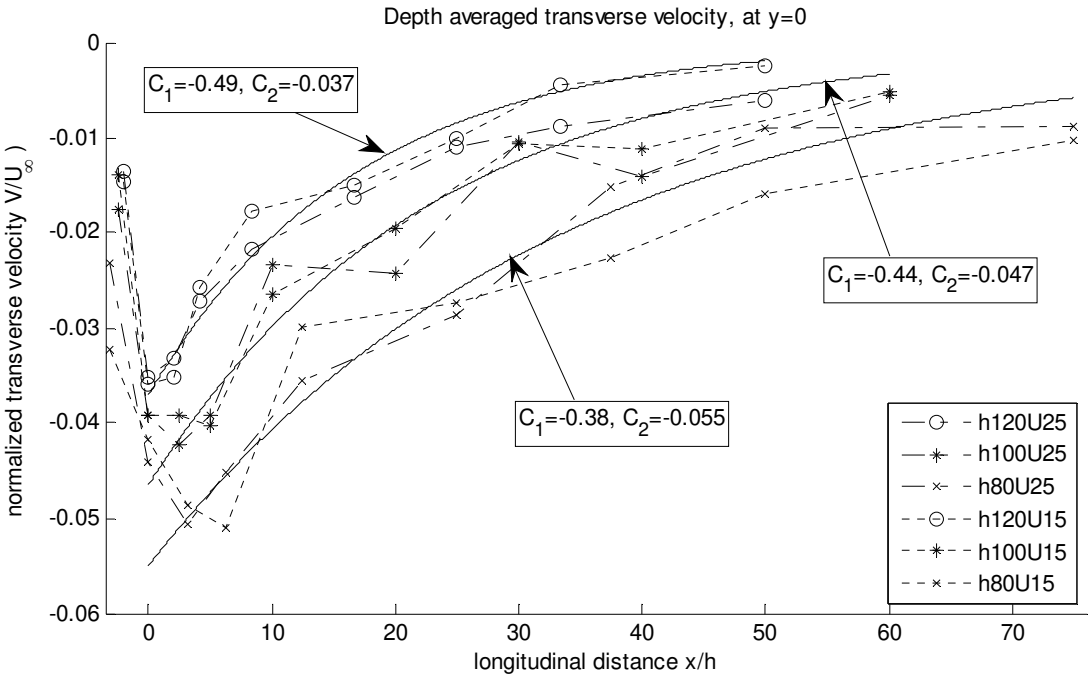

Figure 24; Depth averaged transverse velocity in downstream direction taken at the edge of the roughness patch, i.e. at y=0. The velocity has been normalized by the ambient velocity and the longitudinal direction by the water depth. The water depth is the dominant parameter in these experiments while the ambient velocity is not. The solid lines represent an exponential fit to the near wake measurements with corresponding coefficient as in (12).

In which the expression for V_0 has been substituted and D is defined as the width of the patch. Determining the coefficient C_1 based on (13) gives values deviating from the fitting coefficients as given in Figure 24 as '$C_1 + (0.185 \pm 0.006)$'.

4.4. Mixing layer

A mixing layer in the horizontal plane (vortices with vertical axis) transports momentum from the high velocity side to the low velocity side thereby weakening the velocity gradient present. The vortices are caused by the shear between the high and low velocity parts of the flow. In this way the turbulent kinetic energy (TKE) is extracted from the main flow due to this lateral shear and will feed the large structures in the mixing layer.
The structures in the mixing layer differ from regular fluctuations in the sense that they are correlated and therefore contribute to the momentum balance. Random fluctuations are uncorrelated implying that the averaged product of the fluctuations (covariance) in the horizontal plane is equal to zero for infinitely long signals, i.e. $\overline{u'v'} = 0$. The self similar solution of the plane wake shows the maximum covariance to be found at the wake half width of the transverse velocity profile (Figure 6), i.e. the inclination point.
In the case of the unbounded plane wake, all TKE extracted from the main flow by shear is gained by the structures in the mixing layer. In the case of a bounded wake, like the shallow wake, bottom friction dissipates a part of this TKE as well. In the case that the bottom friction becomes higher, the large structures in the mixing layer will not grow any further which is the essence of the stability parameter 'S'.
In Figure 25 the normalized spanwise Reynolds stress (or correlation) has been shown. The magnitude of the correlation is highest for the shallowest case which is explained by the large velocity difference created by the roughness patch. The wake half width, retrieved from the streamwise velocity profiles, is shown by the solid black line. The key difference with the unbounded plane wake is the movement of the maximum correlation towards the inner side of the wake (note that compared to Figure 6, only half of the wake has been measured due to reasons of symmetry) instead of being positioned at the wake half width. This difference can also be seen in the results of Uijttewaal & Booij [2000], in which the maximum covariance of a single bounded mixing layer is slightly shifted to the low velocity side. Possible suggestions for the cause are (i) asymmetry of the vortices, (ii) the movement of vortices by the secondary circulation and (iii) the movement by the mass flow. Since the data as shown in the Figure 25 have been retrieved at half the water depth, the secondary circulation can be excluded due to the presence of weak velocity components at this height.
The averaged transverse velocity component as given in Figure 24 is suggested to be the reason. The fitted expression as in (12) combined with the time scale determined by the streamwise velocity, results in a trajectory of a particle submitted to the transverse mass flow as indicated in Figure 25 by the dashed line which captures the maximum covariance at least in the near wake region.
The cases with an ambient velocity of 15 cm/s show similar results, only the magnitude of the correlation is lower but the propagation in streamwise direction remains similar, which confirms the expectations where the magnitude of the spanwise Reynolds stress is mainly determined by the velocity gradient. It is suggested that the misalignment between the position of the wake half width and the position of the maximum spanwise Reynolds stress is influencing the growth of the mixing layer negatively.
As opposed by Vermaas et al. [2011], the maximum covariance within the mixing layer seems to be tilted over the vertical for which the secondary circulation can be the causing factor. This cannot be confirmed by the data obtained in this experiment, in fact no clear tilting of the maximum covariance in the vertical can be recognized.

As depicted in §3.5.3, the usability of the covariance of the fluctuations is limited up to one data point per measurement, i.e. for the h120-cases, only three points are present in the vertical for the Reynolds shear stresses. To get the depth average values for the covariance, the points have been extrapolated at 0th order to the surface and bottom, meaning the magnitude at the bottom is equal to the nearest data point available. After the extrapolation, the depth averaged value has been calculated and used in the following sections.

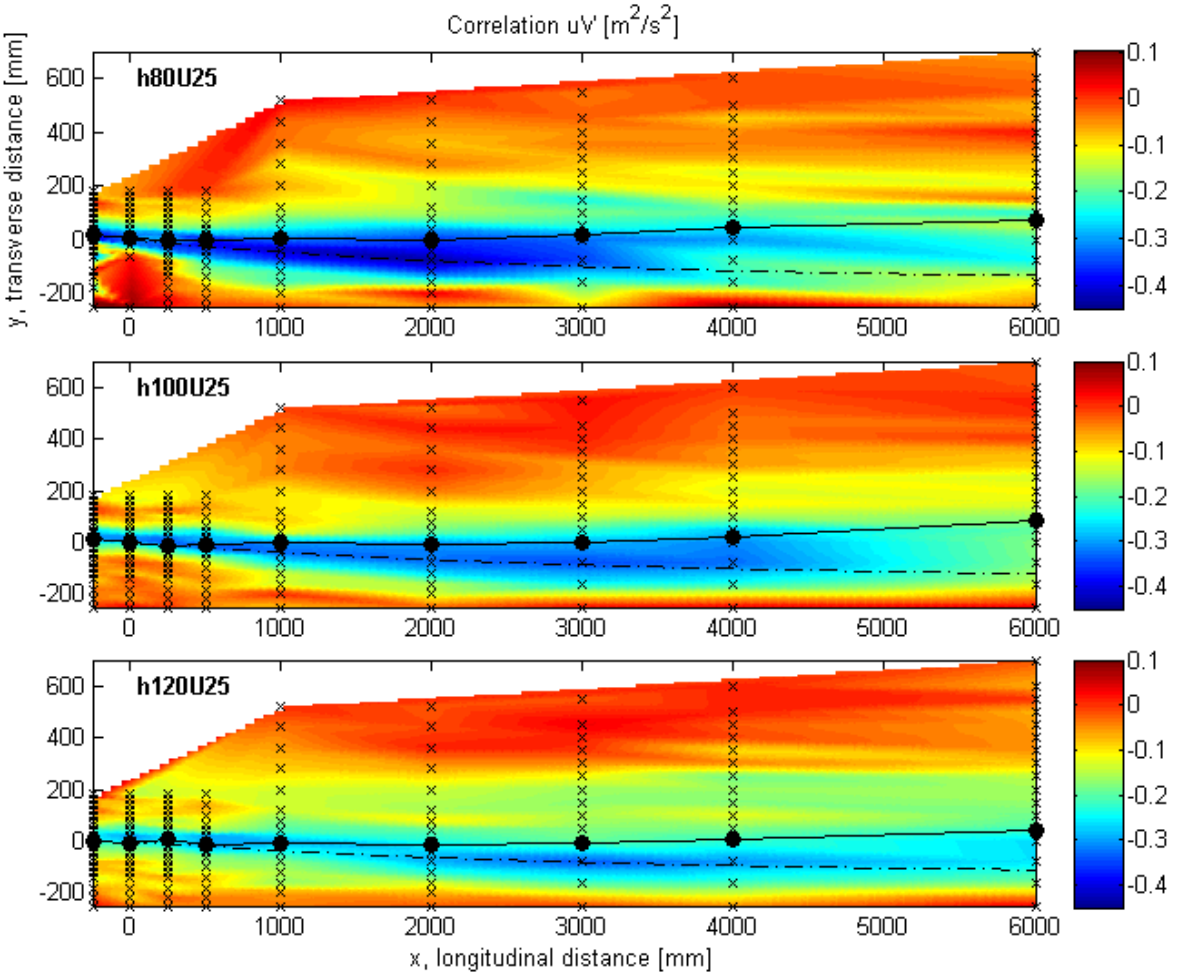

Figure 25; Correlation between horizontal fluctuations, i.e. the covariance u'v' normalized by the standard deviations of the individual signals, for the cases h80U25, h100U25 and h120U25. Data taken at mid-depth. The crosses represent the data points of which the total colored area has been interpolated linearly. The black dots are located at the measured wake half width. The dashed black line represents the trajectory of a particle subjected only to the averaged transverse velocity.

4.5. Secondary current

The origin of the secondary currents have been demonstrated theoretically in two separate ways. Hinze [1967] derived the presence of downflow above a rough surface and upflow above a smooth surface by means of the TKE-equation. Einstein & Li [1958] showed the existence of the secondary circulation by the vorticity equations (both Appendix A). The one by Hinze, which states the origin as a local inequality between production and dissipation of TKE, is depicted as a consequence of the secondary motion and not the cause of the circulation by Nezu & Nakagawa [1993]. For instance a feedback mechanism is present for secondary cells and sand ridges in which the secondary motion stimulates the growth of the sand ridge which in itself increases the local bed friction again which in turn develops the strength of the secondary cell even further. Although in general preference is given to apply the vorticity equations, which shows that the secondary motion is generated by the anisotropy of the vertical and transverse turbulent fluctuations, the physical interpretation of its cause is not straight forward.
The consequences of the circulations are clear, it will transport momentum, energy and other properties. If the secondary circulation is present next to the roughness patch, it will be advected downstream. This also applies for the TKE, which keeps the anisotropy of the turbulence present in the near wake. The additional production of TKE due to the bottom friction of the patch disappears.

In Figure 27 the cross sectional velocity vectors are given for the sections x=1000 mm and x=3000 mm for the case h120U25. They represent the summation of the depth averaged transverse flow and the secondary circulation. Since the measurements for the h120U25 case are limited and range from approximately z=20 mm to z=80 mm, the depth average transverse flow has been determined by extrapolation of the results to the bottom and the surface. The results of the transverse flow have been discussed in §4.3. To obtain the velocity vectors of the secondary circulation, the depth averaged transverse flow has been subtracted from the original cross sectional vectors. The results are shown in Figure 26 for four cross sections. Note that the first section is taken above the roughness patch. Since the transverse mass flow decreases with downstream distance, the effect of the subtraction must decrease with downstream distance as well, which can be confirmed by the two sections given in Figure 27. Here the section of x=1000 mm shows a small circulation around y=80 mm at which it becomes more apparent when the depth averaged transverse flow is subtracted. For the cross section at x=3000 mm, both the circulation and the mean transverse flow have decreased in strength. The circulation can already be seen in the section shown in Figure 27 without subtracting the mean transverse velocity field.
The secondary current next to the roughness patch, i.e. at x=-250 mm, is hard to distinguish compared with the results obtained by for instance Vermaas et al. [2011]. Although a small circulation seems to be visible with a center point at y=80 mm, it is less convincing than reported by others. A possible explanation is the disturbance of the measurements by the presence of the individual stones since the vectors above the roughness patch show a more or less random orientation.
For all cases, the existence of the circulations are most clear just behind the roughness patch which is to be expected as its strength decreases in downstream direction in the absence of the roughness patch. For all six cases, the velocity vectors for the secondary currents at x=250 mm are shown in Appendix E.

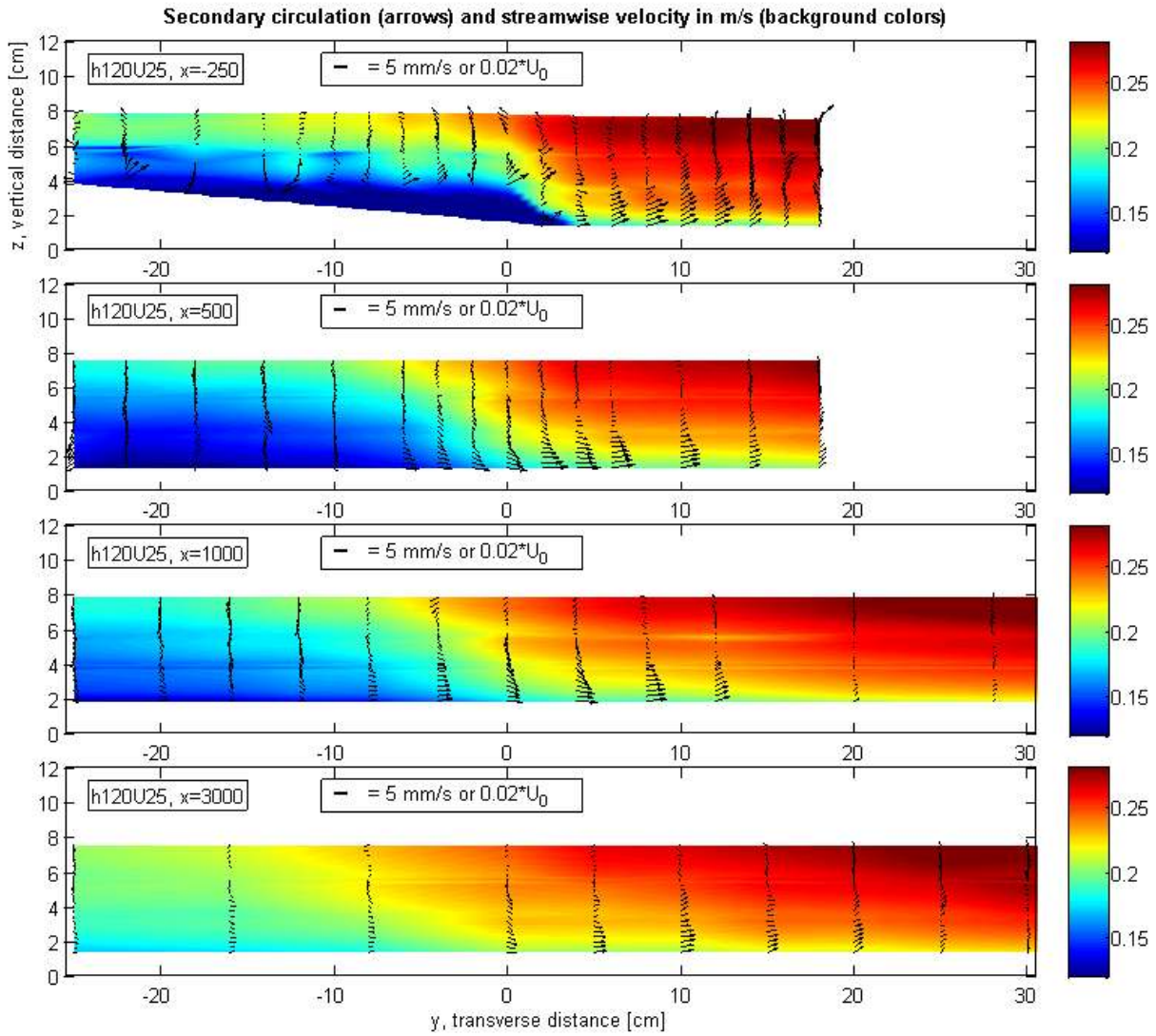

Figure 26; Secondary circulation for the case h120U25 indicated by the black arrows. On the background the streamwise velocity is given by colors. The patch is located at the top graph at the domain y=0 to y=-25.

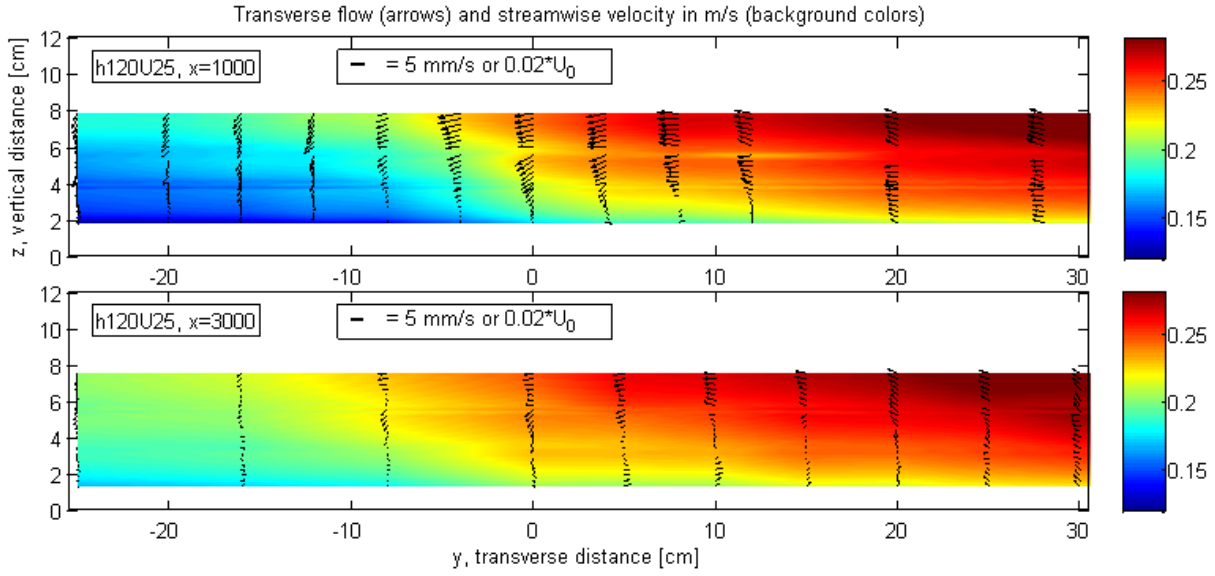

Figure 27; Cross sectional velocity vectors. The vectors represent the sum of the secondary circulation and the transverse mass flow. In the background the streamwise velocity has been included in colors.

The magnitude of the secondary circulation decreases with downstream distance. However there is no common standard on how to quantify this magnitude. For instance, Tominaga & Nezu [1991] scale the vectors with the maximum streamwise velocity while others scale with the depth average velocity, i.e. Studerus [1982] and Rodriquez & Garcia [2008]. Similarly it is unclear at what position these magnitudes are based. According to the data and magnitudes presented by others, there seems to be a majority to use the size of the maximum vector below the center point. By using these vectors as the characteristic magnitude of the secondary circulation, we find just behind the patch at x=250 mm a magnitude for the U15-cases of approximately 2.5% of the ambient velocity and for the U25-cases a strength of 3% of the ambient velocity implying that the magnitude of the secondary circulation with respect to the ambient velocity is more sensitive to the velocity than to the waterdepth.
Nezu & Onitsuka [2001] obtained for a partly vegetated open channel flow, at different Froude numbers, an increase in the intensity of the secondary circulation for an increased Froude number. The Froude numbers in the present experiment have a range of 0.23-0.28 for the U25-cases and 0.13-0.17 for the U15-cases which indeed shows an increase in intensity for increased Froude numbers. However, other experimental results do not show a change in strength with increasing Froude number, i.e. Nezu & Nakagawa [1993].

A more conventional approach to quantify the secondary current can be deducted from the model derived by Ikeda [1981]. The model is based on the streamwise vorticity equation in which the maximum velocity components are described by equation (14) and (15) and the bottom shear stress by equation (16). The angular brackets denote averaging over the perimeter of the circulation cell.

$$\frac{V}{\langle U_* \rangle} = -\frac{6A}{\kappa\pi^2} \quad \textbf{(14)}$$

$$\frac{W}{\langle U_* \rangle} = \frac{6A}{\kappa\pi^2} \quad \textbf{(15)}$$

$$\frac{\tau_b}{\langle \tau_b \rangle} = 1 + A \quad \textbf{(16)}$$

The assumptions made only hold for the ideal case and show the bed shear stress and the velocity components for transversely repeating secondary cells, i.e. cellular currents, resulting in a sinusoidal change of the bed shear stress in the transverse direction. The variable ‘A’ defines the amplitude of the local shear stress as a result of this repetition with respect to the averaged bed shear stress. If the ratio of the shear stresses (equation (16)) remain equal for different types of flow, the intensity of the current is assumed equal because the change in bed shear stress is a direct consequence of the circulation. Hence it is more appropriate, in terms of the physical interpretation, to use the shear velocity as a scaling parameter for the intensity of the secondary circulation instead of the ambient or maximum streamwise velocity.

Since the condition at x=250 mm are far from ideal to determine the averaged shear velocity for the equations (14) - (16), not the perimeter averaged shear velocity but the equilibrium shear velocity has been used based on the friction coefficient for a smooth wall.
In Figure 28 the intensities of the secondary circulation just behind the patch are shown. An increased intensity is seen for increased ambient velocity. The water depth seems to have an influence on the intensity as well.

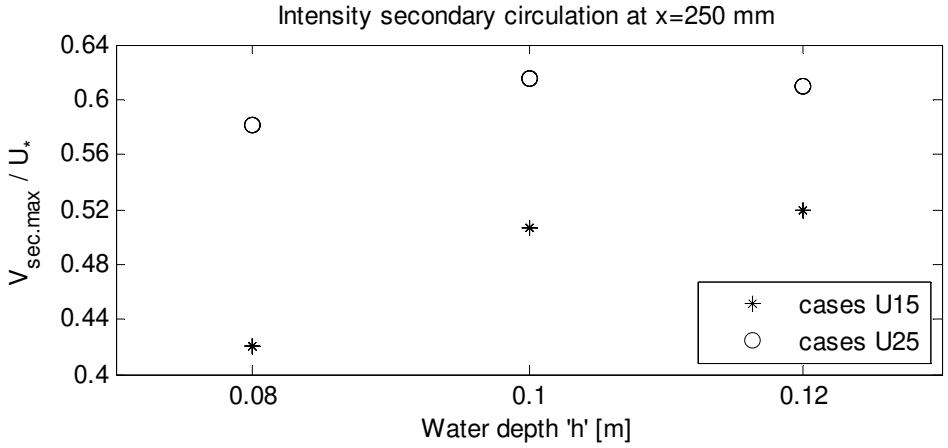

Figure 28; Intensity of the secondary circulation for all cases just behind the patch (x=250 mm). The maximum velocity vector has been normalized by the equilibrium shear velocity.

Based on other experiments on cellular circulations, e.g. Nezu & Nakagawa [1993], and theoretical estimations, Tominaga & Nezu [1991], the undisturbed secondary currents show a maximum bed shear stress which is twice as large as the averaged bed shear stress. This implies that the intensity of the motion is 1.48 which is significant different from results obtained in these experiments. Tominaga & Nezu [1991] obtained a value of 0.7 for compound channel flow which is about the same as the values obtained for the U25-cases.

4.6. Momentum exchange

In order to examine the momentum transport by the various processes described in the previous paragraphs, an integral and differential analysis can be applied. For the latter the two dimensional shallow water equations can be used, see Vreugdenhil [1994], which should be sufficient for examining the accuracy of the data obtained. However the differential analysis requires higher detail of the data making the integral analysis in this case preferable.

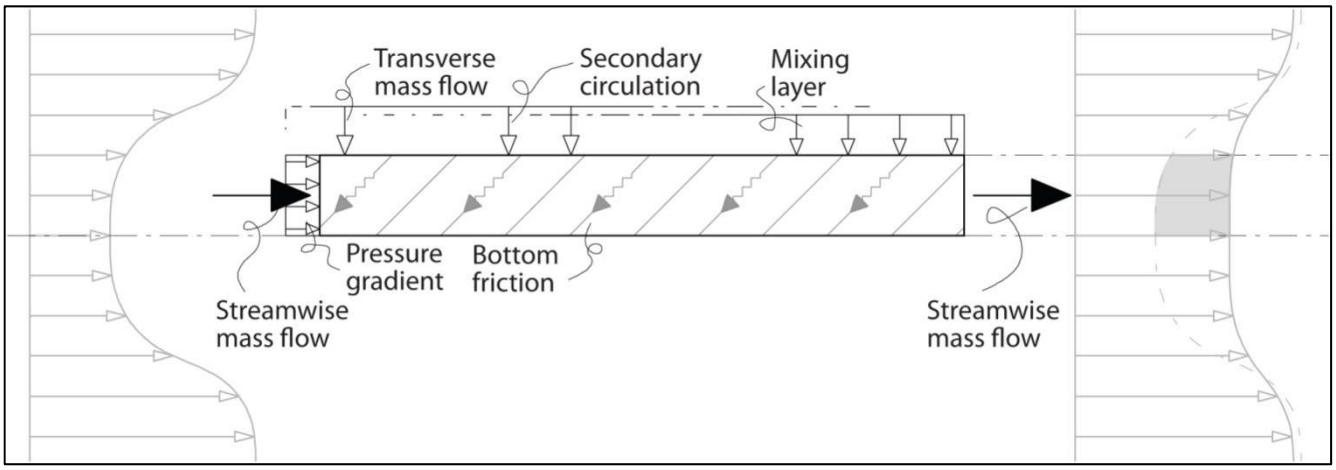

Figure 29; Integral analysis for the conservation of momentum. The momentum fluxes entering the control volume must equal the fluxes leaving the control volume. The control volume has transverse coordinates of y=-250 mm and y=0 mm. The x-coordinates are x=500 mm and x=6000 mm.

In Figure 29 the schematization of the control volume is presented. The volume start 500 mm behind the roughness patch and ends at 6000 mm behind the patch. The width of the volume has been chosen between y=-250 mm and y=0 mm. The centerline has been chosen as a boundary due to the assumption of no momentum transport across the centerline by reasons of symmetry.
In addition to the three processes described in the previous paragraphs, the hydrostatic pressure and the bottom friction need to be taken into account as well.
Based on the second law of Newton, the contributions can be derived individually but can also be seen from the streamwise component of the depth averaged two dimensional shallow water equation (17) and (18) (Vreugdenhil, 1994), in which the capital U and V represent time averaged values as well as the tilde above the Reynolds stress. The over bar corresponds to the depth averaged value.

$$\underbrace{\frac{\partial(h\bar{U})}{\partial t}}_{1}+\underbrace{\frac{\partial(h\bar{U}^2)}{\partial x}}_{2}+\underbrace{\frac{\partial(h\bar{U}\bar{V})}{\partial y}}_{3}+\underbrace{gh\frac{\partial h}{\partial x}}_{4}-\underbrace{\frac{1}{\rho}\tau_b}_{5}-\underbrace{\frac{\partial(h\overline{T_{xx}})}{\partial x}}_{6}-\underbrace{\frac{\partial(h\overline{T_{xy}})}{\partial y}}_{7}=\underbrace{F_x}_{8} \qquad (17)$$

$$T_{ij}=\frac{1}{h}\int_{z_b}^{h}\left[\underbrace{\nu\left(\frac{\partial U_i}{\partial x_j}+\frac{\partial U_j}{\partial x_i}\right)}_{9}-\underbrace{\widetilde{u_i'u_j'}}_{10}+\underbrace{(U_i-\bar{U}_i)(U_j-\bar{U}_j)}_{11}\right]dz \qquad (18)$$

Term 1 is zero because we have taken the time averaged value of the measured signals and not the ensemble average which is allowed for a stationary flow like the wake. Term 2 is shown in Figure 29 and represents the difference between the streamwise mass flow at the beginning and the end of the control volume. The transverse mass flow, the hydrostatic pressure and the bottom friction

correspond to term 3-5 respectively. Term 6 and 7 are a summation of the processes frequently modeled by means of an eddy viscosity parameter, i.e. the viscous stresses, turbulent stresses and the differential advection (18). Term 9 of this summation is negligible for sufficiently high Reynolds numbers and at some distance from the wall. Term 11 represents the secondary circulation as described in §4.5 and is an additional term originating from the depth averaging analysis.
Term 6 in (17) is not taken into account in the control volume. Again the viscous term can be neglected for similar reasons, the differential advection is not present because in the upcoming derivation of the streamwise momentum term the depth averaging is done after taking the square of the streamwise velocity. Term 10 of this summation is the turbulent normal stress, which might be neglected since it contributes only little to the transport of mean momentum compared to the shear stresses (Tennekes & Lumley [1972], p. 33). To make sure it is, the magnitude of the term has been compared to the other terms present in the control volume which confirms its minor importance.
Integration over the section which the force is acting on, leads to the balance equation for the control volume and the formulation of the individual terms (19)-(25). Note the differential advection for the cross term is taken into account by using the actual depth average value of the transverse velocity in the advection term for the mean velocity components.

Balance: $$M + \tau = MF + Mix + SC + Pr \quad \textbf{(19)}$$

$$M = h\rho \int_{y_1}^{y_2} \left(\overline{U_{out}^2} - \overline{U_{in}^2}\right) dy \quad \textbf{(20)}$$

$$MF = h\rho \int_{x_1}^{x_2} -\left(\overline{U\bar{V}}\right) dx \quad \textbf{(21)}$$

$$SC = h\rho \int_{x_1}^{x_2} -\overline{U\,(V - \bar{V})}\, dx \quad \textbf{(22)}$$

$$Mix = h\rho \int_{x_1}^{x_2} -\overline{u'v'}\, dx \quad \textbf{(23)}$$

$$\tau = \rho \int_{x_1}^{x_2} \int_{y_1}^{y_2} -u_*^2 \; dy\, dx \quad \textbf{(24)}$$

$$Pr = \rho g h \int_{x_1}^{x_2} \int_{y_1}^{y_2} -\frac{dh}{dx} \; dy\, dx \quad \textbf{(25)}$$

The term 8 of (17) has been set to zero since no external forces are taken into account. Two methodologies could be used to derive the bed shear stress based on the data present. One is the extrapolation of the Reynolds stress u'w' to the bottom, the other is by fitting the streamwise velocity profiles to the log-law. The first is chosen which will be clarified in the last section of this paragraph. Although the main interest lies with the momentum transport by the secondary circulation and the mixing layer, the balance equation has been analyzed for all six cases in order to examine the accuracy of the data obtained. It must be mentioned that for the h100U25 case, the control volume does not end at x=6000 mm but at x=4000 mm since the last transverse profile of the streamwise velocity shows a large deviation with respect to the upstream profiles resulting in a large imbalance of the balance equation. The results for the six cases are shown in Table 1 in momentum per unit time.

[N.s/s]	*h120U25*	*h100U25*	*h80U25*	*h120U15*	*h100U15*	*h80U15*
M	0.501	0.521	0.607	0.111	0.137	0.203
τ	0.187	0.169	0.161	0.071	0.045	0.053
MF	0.513	0.512	0.462	0.140	0.138	0.183
SC	0.064	0.066	0.057	0.025	0.028	0.024
Mix	0.062	0.077	0.104	0.019	0.020	0.024
Pr	0.221	0.233	0.249	0.086	0.057	0.096
Error [-]	0.20	0.22	0.12	0.32	0.26	0.21

Table 1; absolute magnitude of the processes acting on the control volume in N·s/s, i.e. momentum per unit time. The meaning of the abbreviations can be found at (20) - (25). The error is based on (19) and represents the fraction of the shortage of the LHS with respect to the RHS and vice versa. Note the length of the control volume of h100U15 is shorter with respect to the other cases.

The imbalance of the balance equation is approximately 20-25% which seems reasonable for the experimental data obtained. This error suggests that the contribution of the mechanisms is of the same order as the data presents. The error is expected to be caused by the underestimation of the bed shear stress, as will be described at the end of this paragraph, and the extrapolation of the transverse velocity profile to the surface. Especially if there is still a small rotation angle left in the orientation of the ADV, it will affect the latter of the two.
Since the momentum deficit is the main characteristic of the wake, the processes have been normalized by the difference in streamwise mass flow (M). The corresponding ratios are shown in Table 2. The relatively large error of the h120U15 case can be explained by the relatively low momentum deficit which is twice as large for the other cases.

	h120U25	*h100U25*	*h80U25*	*h120U15*	*h100U15*	*h80U15*
τ_{norm}	0.37	0.32	0.27	0.64	0.33	0.26
MF_{norm}	1.02	0.98	0.76	1.26	1.01	0.90
SC_{norm}	0.13	0.13	0.09	0.22	0.21	0.12
Mix_{norm}	0.12	0.15	0.17	0.17	0.15	0.12
Pr_{norm}	0.44	0.45	0.41	0.77	0.42	0.47

Table 2; relative magnitude of the processes acting on the control volume. The processes have been normalized by the gain of streamwise momentum (M).

The transverse mass flow (MF) is dominant, which is mainly due to its intensity in the near wake. Furthermore, the magnitude of the secondary circulation decreases for a decrease in water depth which is in agreement with the results of Vermaas et al. [2011]. Although the absolute value of the transferred momentum is higher for the high velocity cases, the relative magnitude is lower presumably caused by the faster decrease in magnitude of the circulation with respect to the low velocity cases, as shown in Figure 32 (note the different scaling of the vertical axis).
For the contribution of the mixing layer the results are ambiguous. The absolute magnitude increases with velocity and decreasing water depth. The relative contribution however shows for the U25-cases a increase with decreasing water depth but the other way around for the U15-cases.

As seen in Figure 31, the contribution of the mass flow to the decrease of the momentum deficit is dominant in the near wake (as used for the derivation of (12)). Although the exchange due to the transverse mass flow is for the h80-cases still large in the far wake, the magnitude for the h120U15 case is comparable to the exchange by the secondary current. Essentially, in the far wake all

processes shown in Figure 31 are of the same order implying none of the mechanisms can be neglected.
If we look closer to the contribution of the secondary current and the mixing layer to the decrease of the momentum deficit (Figure 32), we see for the most extreme cases, i.e. h80U25 and h120U15, a clear distinction. The exchange of momentum by the secondary circulation is larger than the mixing layer for the low velocity and high water depth case while it is the opposite for the high velocity and low water depth case. Figure 32 suggest a dominant influence of the water depth over the effects of streamwise velocity on these two mechanisms since the momentum exchange by the secondary circulation tends to be larger compared to the mixing layer for the h120U25 case and the reverse holds for the h80U15 case.
The influence of the water depth on both processes has also been examined by Vermaas et al. [2011] resulting in a similar conclusion. The influence of the ambient velocity on these processes has resulted in an increase in intensity for both for increasing Froude number see Nezu & Onitsuka [2001]. Although the results in Figure 28 suggest an increase in the intensity of the secondary circulation with increasing Froude number in this experiment as well, the efficiency of the processes , i.e. the amount of momentum transported, is not. An increase in velocity shows a greater increase of the transport by the mixing layer compared to the transport by the secondary circulation.

A possible explanation for the absence of a tilted spanwise Reynolds stress over depth as seen by Vermaas et al. [2011] is the difference between the location of the maxima of both mechanisms. As shown in Figure 33, the distance between the maxima is approximately equal to the waterdepth. The momentum exchange as a function of the transverse coordinate is multiplied by -1 for reasons of comparison. The data for the secondary circulation is quite vulnerable for extrapolation although a trend is visible.
The vertical cross gradient in the streamwise velocity distribution as seen in §4.2 was suggested to be linked to the secondary circulation and the mixing layer. This can be demonstrated by taking the momentum transport of the upper and lower half of the water layer. Since formulation (22) is meant for the transport over the whole depth, the formulation is rewritten to (26) which takes the net momentum transport for the lower half, e.g. if a secondary circulation is present in a uniform unbounded flow, the secondary circulation does transport momentum but it does not lead to an increase or decrease of the momentum locally.
Likewise, uniform momentum transport of the secondary current in the transverse direction does not cause any changes in the local momentum, it is a gradient which does. Hence to examine the gain and loss of momentum by the secondary currents the gradient in y will be taken of (26). Similar is done for the mixing layer.

$$SC_{Lower} = \rho \int_0^{\frac{1}{2}h} -(U - \overline{U})\,(V - \overline{V})\; dz \qquad \textbf{(26)}$$

Since the linear interpolation between the measuring points results in a constant gradient for a finite area and the unnatural peaks in the momentum transport resulting from the extrapolation of the data, e.g. Figure 33, the data has been smoothed. The result is shown in Figure 34 for the h120U25 and h80U25 cases in which a negative gradient (blue) concludes a local gain of momentum and a positive gradient (red) means a loss of momentum.
The secondary current near the bottom causes, similar as the mixing layer, a decrease in momentum at the outer part and an increase at the inner part of the wake. Only the magnitude is larger for a

larger water depth. The opposite is true for the mixing layer which is more dominant for the lower water depth case. If we sum all the four contributions, we find the distribution as shown in the lowest two graphs. Although the contributions show clear differences with respect to its magnitude, dominance and location, the total change by these two mechanisms seems to be fairly similar. While the complete transfer of both cases looks similar, the distribution over the two layers is not. The distribution for the shallowest case already shows an inequality for the transport in the upper and lower layer which suggests that the number of measuring points in the vertical for the shallowest case is too low to clearly detect the cross gradient. The inequality for the h120U25 case is larger which confirms the cause of the cross gradient to be the secondary circulation in conjunction with the mixing layer.

As the change in dominance between the secondary circulation and the mixing layer is examined in this section for stationary cases, in practice the boundary conditions as the ambient velocity and the thickness of the boundary layer (in the vertical) are changing. For the patch of rocks in an estuary (Figure 2a) the waterdepth and the ambient velocity are changing due to tidal and river influences. For a city in the atmospheric boundary layer, only the direction and ambient velocity are of influence since the boundary layer thickness is relatively constant in time.
If in the example of a patch of rocks in an estuary, the patch is constantly submerged, located closely to the sea and the boundary conditions are determined by the tide only, a high water level is accompanied by a landwards directed ambient velocity while a low water level is associated with an outward directed ambient velocity (see. Figure 30). The local mixing processes and the sediment transport in the wake of the patch might be different on the leading and trailing edges of the patch, depending on the parameters.

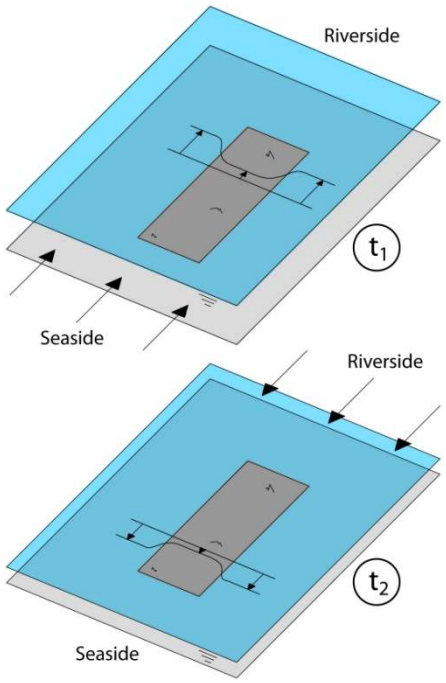

Figure 30; Example of a roughness patch exposed to a tidal cycle. The flow reversal and change in water level will cause different wake characteristics for the edge at the seaside and riverside.

If there is an interest in the prediction of the wake development behind a city, for meteorological reasons or spreading of pollution, the speed of the wind will be a determining parameter since the relative contribution of the secondary circulation to the recovery of the wake increases with decreasing wind speed (e.g. Figure 32). Especially for the spreading of pollution, the depth varying exchange process of the secondary circulation cannot be neglected since the hypothetical pollution near the ground will spread more easily compared to the exchange in the upper part of the boundary layer (e.g. Figure 26).

As mentioned previously, the bed shear stress has been obtained by linear extrapolation of the Reynolds stress u'w' to the bottom. A linear relation between the shear stress and the vertical coordinate is only valid for fully developed flow, which is actually not the case here. However this methodology shows quite convincing results (Figure 35) compared to the results of the shear velocity retrieved by assuming the same but here using the log-law velocity profile (not shown).
The first is believed to be more convincing since it is expected for the bed shear stress outside the

wake to be equal to the equilibrium bed shear stress[13]. For the bed shear stress based on the shear velocity this ratio is twice as large and for the Reynolds stress 0.8-1.0 times the equilibrium bed shear stress. At the same time the extrapolated Reynolds stress shows similarities with experiments performed by others, for instance Lacey & Rennie [2012] who examined the wake caused by a submerged cube. Their results show a decrease in the near bed Reynolds stress u'w' in the far wake for a decreasing relative depth, defined as the water depth divided by the height of the obstruction, and an increase of the area and magnitude of the shear stress at the edges of the obstruction. These characteristics can be found in Figure 35 as well. The area of increased bed shear stress directly downstream of the patch extends to about 10 times the waterdepth and it is suggested to be caused by a mean downward flow. The zone of lower bed shear stress coincides partly with a local decrease of the TKE, see also Figure 35.
The normalized Reynolds stress u'w' is expected to be equal to the one outside the wake which however is not the case. Hence it is expected for the stress to be larger than the results obtained by means of the extrapolation of the Reynolds stress to the bottom. This suggested underestimation of the shear stress is one of the deviations of the momentum balance leading to the estimated error.

The downflow caused by the secondary current which is located around y=0 mm, should cause an increase bottom friction locally and the upflow is expected to cause a decrease in the bed shear stress. These changes are not found in the data as presented. A possible cause is the underestimation of the bed shear stress at the positions of downflow and an overestimation of the stress at the locations of upflow since a linear profile of the Reynolds stress has been assumed combined with a limited number of data points in the vertical.

[13] The equilibrium shear velocity can be obtained from the friction coefficient used in (9).

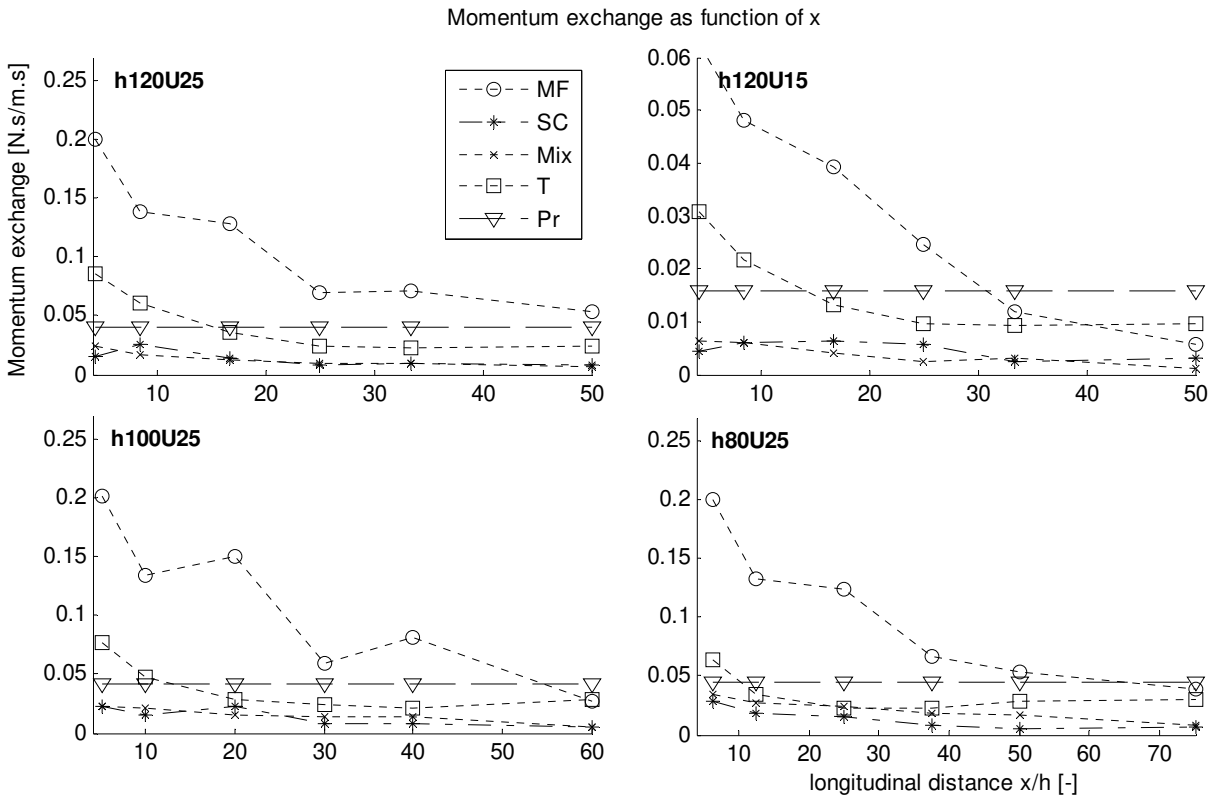

Figure 31; Momentum exchange at y=0 mm for the processes of the balance equation (19). The integral of the processes over x will result in the quantities given in Table 1. Note the dimension of the horizontal axis and the different magnitude of the vertical axis for the h120U15 case (upper-right).

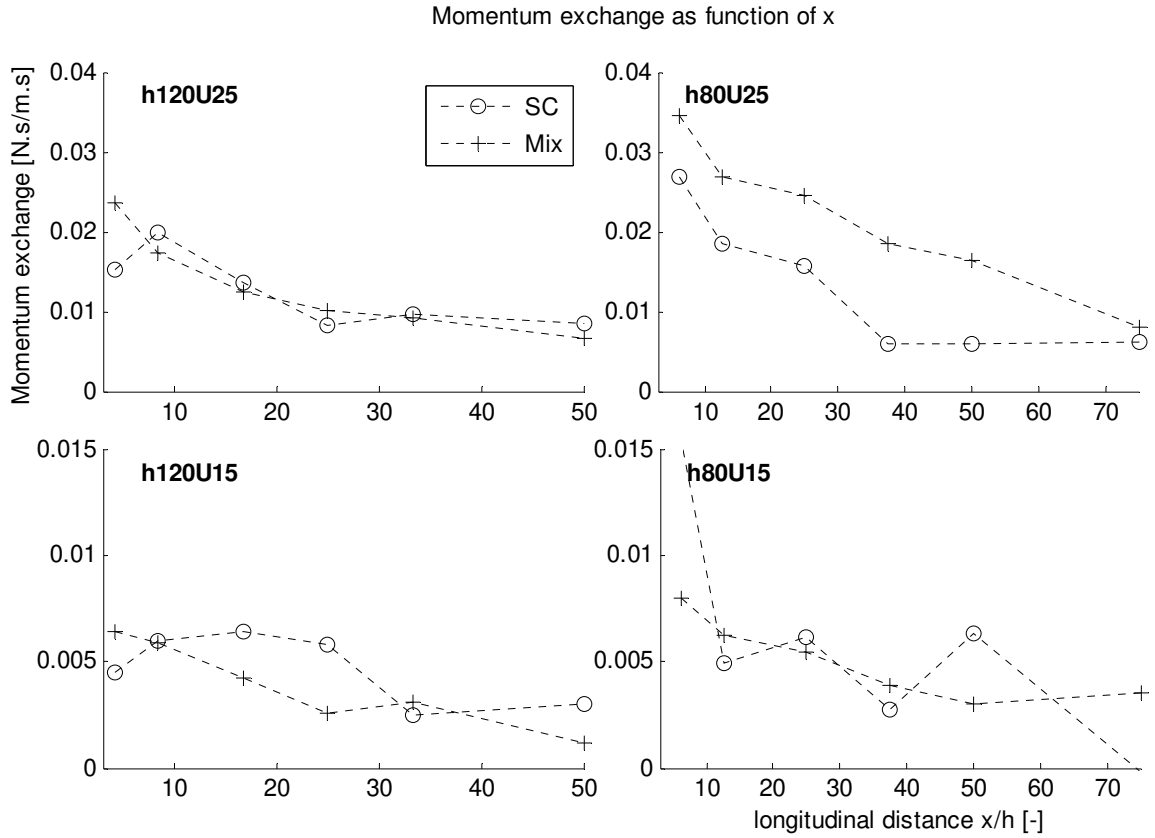

Figure 32; Momentum exchange contribution of the secondary circulation and the mixing layer to the decrease of the momentum deficit at y=0 mm. The horizontal axis is normalized by the waterdepth.

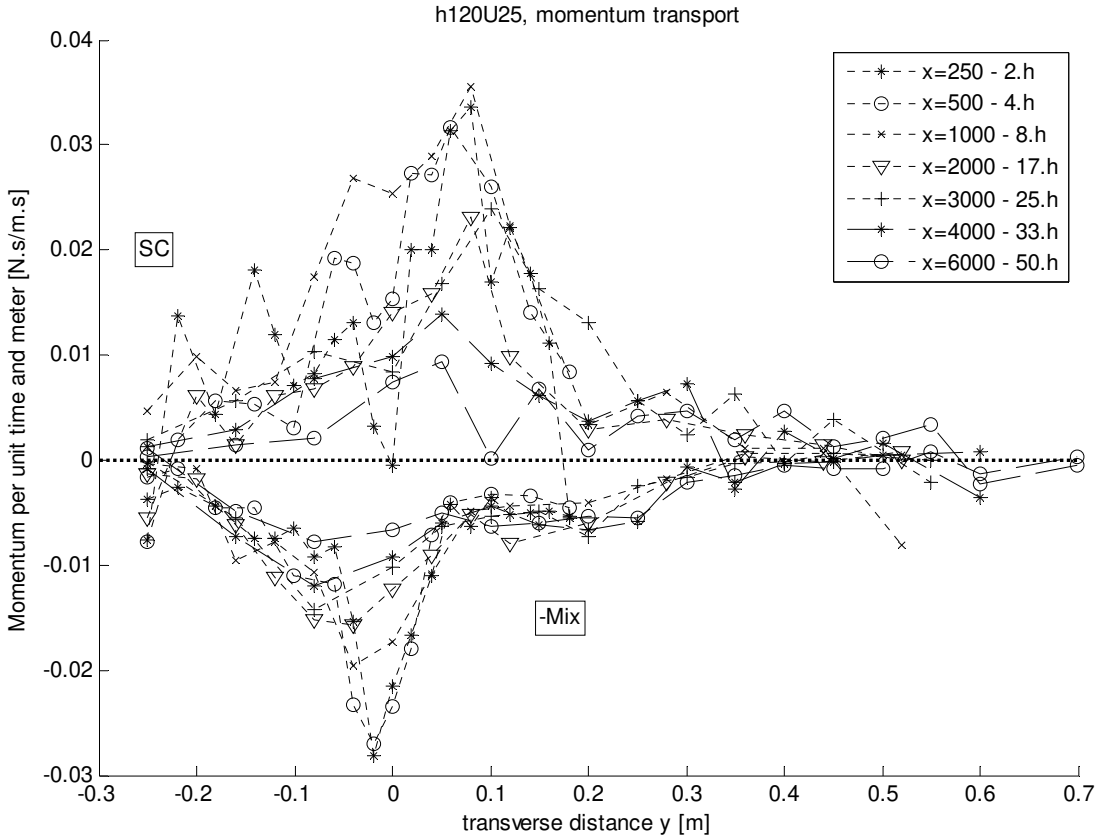

Figure 33; Momentum exchange as a function of x and y for the secondary circulation and the vortices with a vertical axis for the case h120U25. The mechanisms are defined as in (22)(23) (although here not integrated over x). The mixing layer has been multiplied by a minus one in order to visualize the difference.

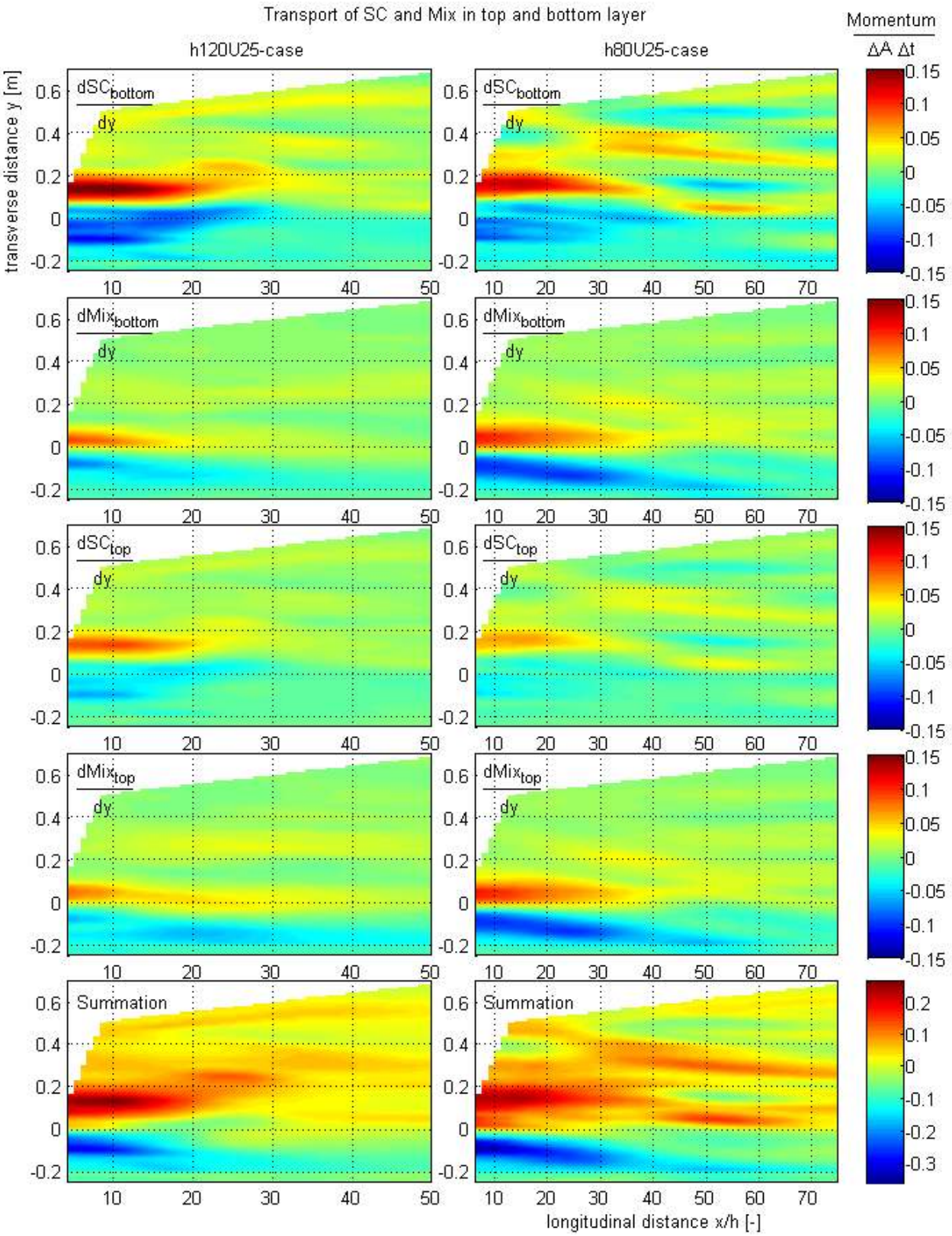

Figure 34; Momentum gain and loss as a function of x and y caused by the secondary circulation and the mixing layer. The color scale is kept equal for all mechanism, except for the summation. The summation represents the sum of the four contributions. SC_{bottom} refers to the momentum transport of the lower half of the water layer while SC_{top} refers to the upper half. Negative values represent an increase in momentum and positive values a decrease.

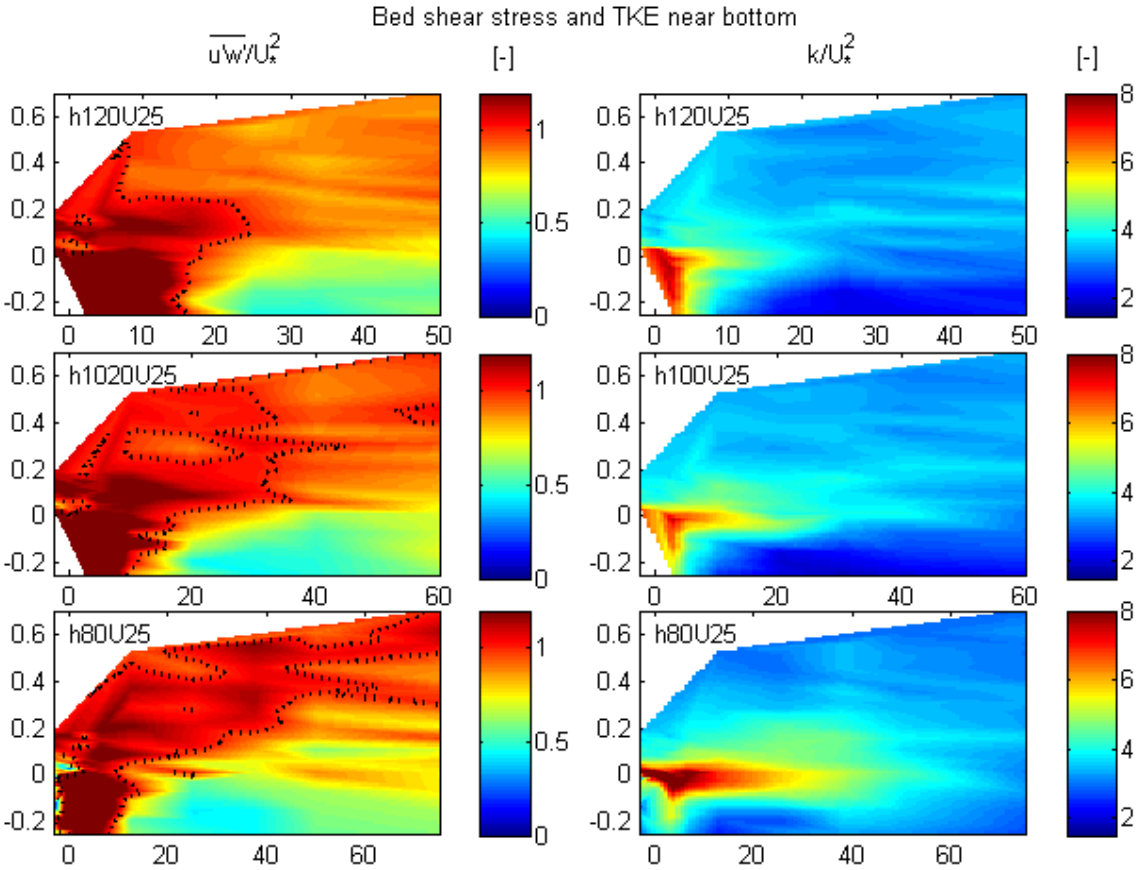

Figure 35; Normalized bed shear stress on the left for the U25-cases. On the right the TKE for these cases obtained 25 mm above the bed and normalized by the equilibrium shear velocity squared. The dotted lines on the left represent the contour line for a value of 1.

4.7. Stability parameter

The stability of the wake for two-dimensional shallow flows can been characterized by the stability parameter (definition repeated in (27)) as done by Chen & Jirka [1995].

$$S_f = \frac{F}{P} = \underbrace{\frac{2\langle u'^2\rangle + \langle v'^2\rangle}{-\langle u'v'\rangle}}_{1} \underbrace{\left(\frac{C_f}{2h}\frac{U}{U_y}\right)}_{2} \quad \textbf{(27)}$$

$$S_c = \left(\frac{C_f}{2h}\frac{U}{U_y}\right) \quad \textbf{(28)}$$

The parameter has been derived theoretically by taking the ratio of the dissipation and production of TKE. The first product on the RHS of (27) has been assumed to be approximately 10 based on the characteristics of fully developed flow.
While the three dimensional shear near the bottom has been approximated by a friction coefficient and a quadratic velocity relation, the contribution of the three dimensional secondary circulation has not been included. The circulation in general dampens the growth of the vortices with a vertical axis in three ways: 1) the bottom friction increases at positions of downflow; 2) the momentum exchange by the circulation weakens the streamwise velocity gradient in transverse direction; 3) the vortices are advected to the centerline of the patch/wake. Although the third has not been confirmed by the experiments and the first is suggested to be present but could not be verified by the data, the second has shown to be significant in §4.6.
For forthcoming estimations, the increased friction by the secondary circulation can be included in the parameter by an increased friction coefficient value, although the correct theoretical approach would be to adapt the complete TKE dissipation term. The additional drag exerted on the flow by the presence of circulation has been examined by many and is often represented by an increased friction coefficient as presented by Townsend [1976] for a finite flat plate in a wind tunnel:

$$\frac{C_f}{C_{f0}} = 1 + C\frac{\delta_{th}}{D} \quad \textbf{(29)}$$

Where δ_{th} is the boundary layer thickness, D the width of the plate and C a coefficient of proportionality. A similar reasoning is reported by Tominaga & Nezu [1991], who examined the additional friction caused by the circulation for compound channel flow by means of the RANS-equations. Assuming a linearly changing transverse flow over depth and no change of the streamwise velocity in spanwise direction, an additional term of $\frac{7}{8}\rho U_*^2$ is found, in which the maximum velocity of the secondary current is found to be $0.7U_*$. The intensity of the secondary circulation has been found to be slightly smaller in these experiments and increasing with the waterdepth, which suggests the additional bottom friction by the circulation to be increasing with water depth.

While the dampening effects of the circulation can be included separately in the variables of the parameter, the essence of the parameter itself should not be overlooked.
The critical stability parameter (28) has been found to be of the order 0.08 – 0.12. The value decreases with increasing porosity of the obstruction. The stability parameters obtained from the data vary from 0.001 – 0.002 which should result according to the parameter into an instable wake. If the ratio of the turbulent fluctuations over the spanwise Reynolds stress in (27) is examined (term 1),

values of 5-14 are found with increasing values for increasing water depth which is of the same order as the 10 for fully developed flow.
The ratio of the dissipation and production of TKE is the essence of the parameter, where a balance between the two denotes the critical parameter, which is for (27) equal to one. Since term 1 in (27) is of the same order as assumed for fully developed flow and term 2 is two order of magnitude smaller, the parameter suggests a negligible bottom friction compared to the momentum exchange by the spanwise Reynolds stress which is as seen in §4.6 not to be neglected. Consequently the stability parameter cannot be used in the three dimensional wake of a roughness patch. Implementation of an increased bottom friction coefficient for reasons of wake stability estimations is therefore unnecessary and the origin of the instability for three dimensional flows is suggested to be unexplainable by means of energy considerations. As can be concluded, the momentum or vorticity balances can provide more insight, knowing that this introduces more complexity of the derivation.

4.8. Spectral Analysis

Spectral analysis is used to identify the development of the macro structures in the flow. Since a given signal can be composed of a finite number of waves each with an amplitude, frequency and phase, the energy of each component can be determined by the square of its amplitude.
The characteristics of the components are obtained by Fast Fourier Transformation with a Hamming window of which the measured signal is divided into six segments to improve the accuracy.

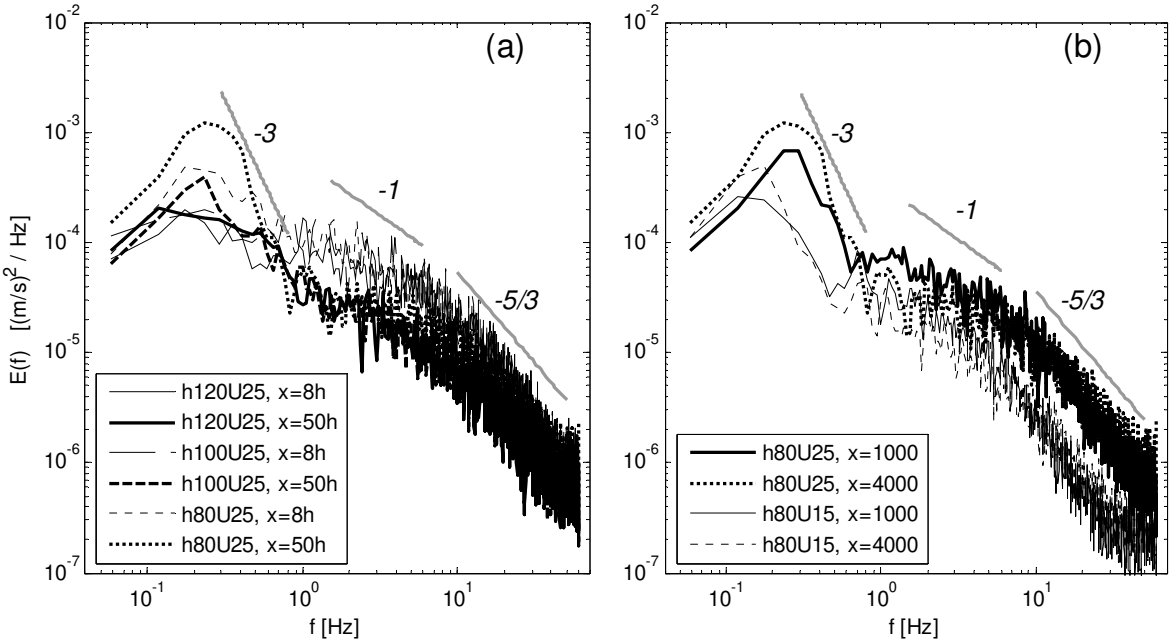

Figure 36; Energy density spectrum for the transverse velocity fluctuations at the centerline of the patch, i.e. y=-250 mm; a) the spectra for a changing water depth; b) the spectra for a changing ambient velocity.

A measurement located in the vortex street of an emergent cylinder results in a distinct peak in the energy density spectrum consistent with the frequency of the shedding. As shown by Carmer [2005] the variety of frequencies corresponding to the large vortices increases for a stabilizing wake, which is translated into a wider peak compared to presence of a vortex street.
In this experiment, similar observations are made. In Figure 36b the spectra for the h80-cases are shown, located at the centerline of the wake. The spectra are obtained by the transverse velocity fluctuations. The spectra for the streamwise fluctuations are not shown since the peak is less evident. This difference can be explained by the favorable position of the centerline at which the maximum and minimum transverse velocity of a vortex is found which is not the case for the streamwise velocity component. The streamwise velocity component of the vortex is at the centerline more sensitive for small displacements of the vortex (see Prooijen, 2004). As shown in Figure 36b, the peak frequency remains constant downstream but increases in intensity for each case. The length scale of the dominant vortices can be obtained by making use of Taylor's hypothesis which is valid in the case the turbulent fluctuations are small compared to the mean velocity. In the far wake, the transverse fluctuations are at most 10% of the streamwise velocity (Figure 23). The peak frequencies are 0.254 Hz and 0.148 Hz for the h80U25 and h80U15 cases respectively.

Multiplying the timescale by the ambient velocity results in a characteristic length scale of 0.98 m and 1.01 m respectively suggesting the large structures are not affected by the change in ambient velocity.
As seen in the videos (representing the macro structures at the surface), distinct macro structures are absent for the h120-cases (Figure 38). This observation is supported by the energy density spectra as shown in Figure 36a. An increase in intensity is seen for increased distance downstream as well as for decreased water depth. The distinct peak frequency vanishes for decreasing water depth. The development of the large structures in the wake is visible in the spectra by a decrease or increase of the energy containment at the peak frequency. A decrease corresponds to a decrease in intensity meaning the vorticity of the structures is dampened. In Figure 37 the development of the spectra for several positions at the centerline of the wake is shown for the h80U25 and h120U25 case. For the h80U25 case the increase in intensity continues till x=2-3 m (25-38 times the water depth) after which the intensity decreases. This position corresponds to the position at which the turbulence intensity start to decay (Figure 23). For the h120U25-case a distinct peak frequency is absent (see also the absence of large structures in Figure 38).

The inertial subrange is for large Reynolds numbers in accordance with to the -5/3 law which states the energy containment in this range is only a function of the energy dissipation and a typical length scale. The length scale is much larger than the Kolmogorov length scale and much smaller than the macrostructure. Assuming Taylor's hypothesis to be applicable, the -5/3 law also holds for the energy density spectrum in the frequency domain.
For quasi-two-dimensional turbulence the high frequency side of the low frequency peak is characterized by a slope of -3. Shallow flow can be classified as quasi-two-dimensional since the vertical length scale is much smaller compared to the horizontal extent of the flow. The -3 slope is however only recognizable in the shallowest cases.

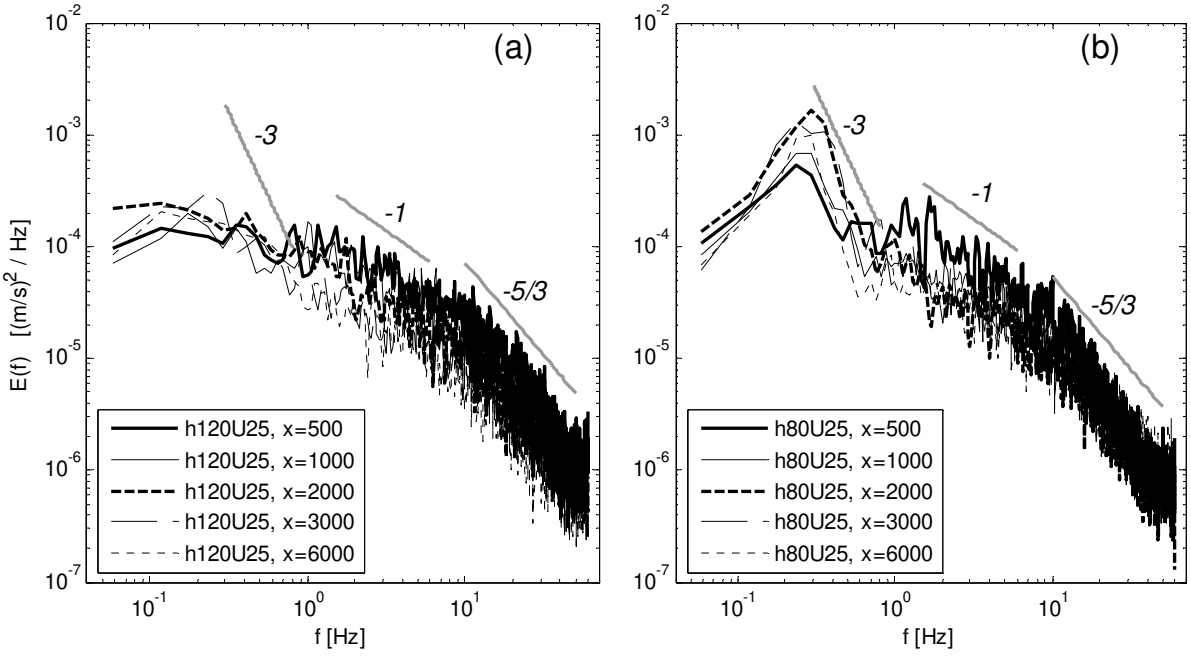

Figure 37; Energy density spectrum for the transverse velocity fluctuations at the centerline of the patch, i.e. y=-250 mm; a) the spectra for the h120U25-case for various distances downstream of the patch; b) the spectra for the h80U25-case for various distances downstream of the patch.

The -1 slope is frequently noticed in wall bounded flow. Nikora [1999] provides an explanation based on phenomenology in wall turbulence, in which the characteristic length scale of the wall shear induced eddies are proportional to the distance to the wall. This implies the -1 slope to be found most likely in the region of the wavelength being proportional to the waterdepth. Although it is not sure whether the -1 slope is present in the spectra presented, for the h80U25 case as in Figure 37, the slope (if present) must be positioned around f=3 Hz (based on Taylor's hypothesis).

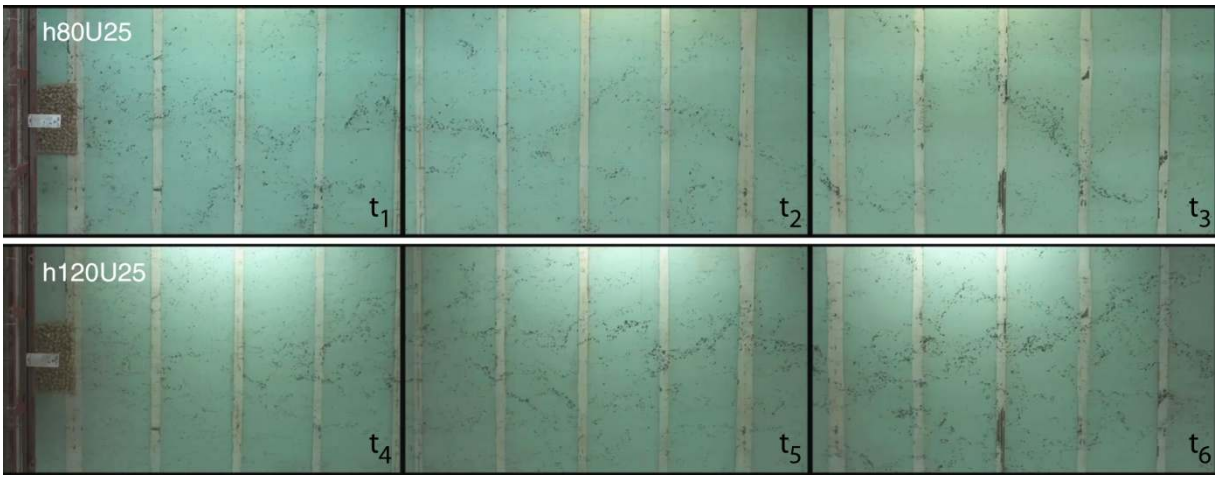

Figure 38; Frame of video for the cases h80U25 and h120U25. Note the separate frames are taken at different time. The width of the roughness patch is 0.5 m, the distance between two glass plates is 0.6 m.

4.9. Modeling

The horizontal extent of shallow water flow sometimes allow three dimensional effects to be neglected. This allows the use of the two dimensional shallow water equations to simulate the flow. In the case of a roughness patch, the three dimensional effects become more dominant and cannot be neglected if the wake needs to be presented more accurately. Since the computational requirements for the three dimensional equations are much larger than the two dimensional equations, the consequences of the three dimensional effect are mimicked by means of models. The spanwise Reynolds stress can for instance be modeled by an increased viscosity parameter since the momentum transport of the vortices show resemblance with the transport of momentum of individual molecules.

The secondary circulation and the spanwise Reynolds stress can be modeled separately or simultaneously as the formulation and their consequences are similar (see (17)-(18)). It is chosen to do separately since their point of acting on the flow is different. As done by Ikeda [1981], the Reynolds stress $\overline{v'w'}$ is approximated by an eddy viscosity model, (30)-(31).

$$-\overline{v'w'} = v_t \left(\frac{\partial V}{\partial z} + \frac{\partial W}{\partial y}\right) \quad \textbf{(30)}$$

$$v_t = \kappa \langle U_* \rangle \frac{h}{6} \quad \textbf{(31)}$$

Although the Reynolds stress term is not present in the two dimensional shallow water equations, the use of an eddy viscosity model is taken over. The secondary circulation (equal to the differential advection, third term of (18)) will be described by:

$$M_{SC} = \frac{1}{h}\int_0^h -[(U-\bar{U})(V-\bar{V})]dz \approx v_t \frac{\partial U}{\partial y} \quad \textbf{(32)}$$

In which the density of the fluid is left out for the moment. The eddy viscosity (v_t) has the dimensions of m^2/s, i.e. a typical length scale times a characteristic velocity scale ($\mathcal{L} \cdot \mathcal{U}$) (see Figure 39).

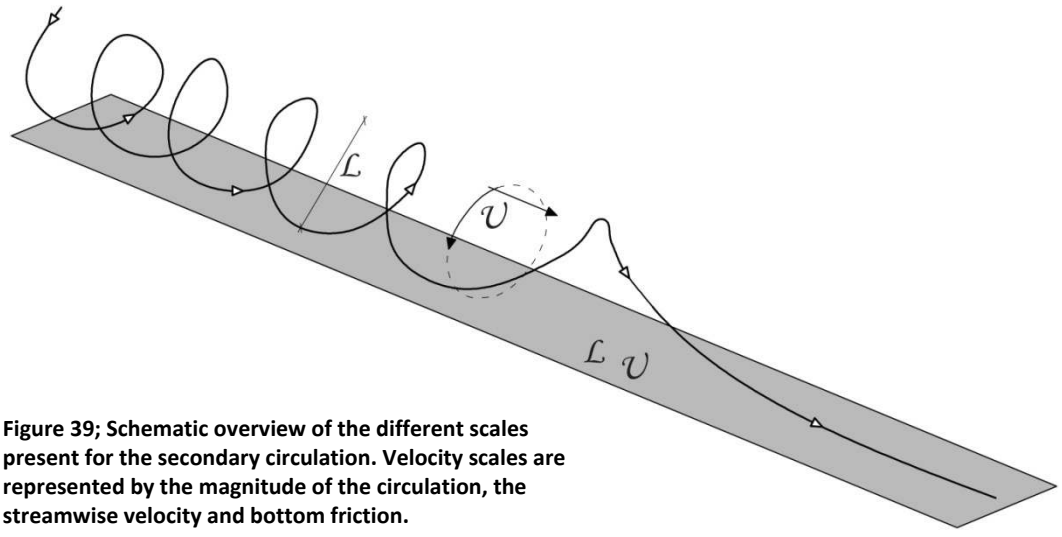

Figure 39; Schematic overview of the different scales present for the secondary circulation. Velocity scales are represented by the magnitude of the circulation, the streamwise velocity and bottom friction.

The characteristic velocity scale of the secondary circulation is the magnitude of the circulation. A typical length scale of the secondary circulation is the water depth since the water depth is limiting the size of the circulation.
In §4.5 the magnitude of the secondary circulation has been related to the intensity by:

$$V_{max} = C_1 \cdot \langle U_* \rangle \quad \textbf{(33)}$$

$$\frac{M_{SC}}{\frac{\partial U}{\partial y}} \approx v_t = C_2\, C_1\, \langle U_* \rangle\, h \quad \textbf{(34)}$$

In which the brackets denote the average shear velocity over the perimeter which is approximately equal to the equilibrium shear velocity. To fit the eddy viscosity model to the experimental eddy viscosity, another constant of proportionality will be included (C_2), see (34). The appearance of the eddy viscosity in (34) is fairly similar to the expression in (31), only the variable C_1 is actually changing

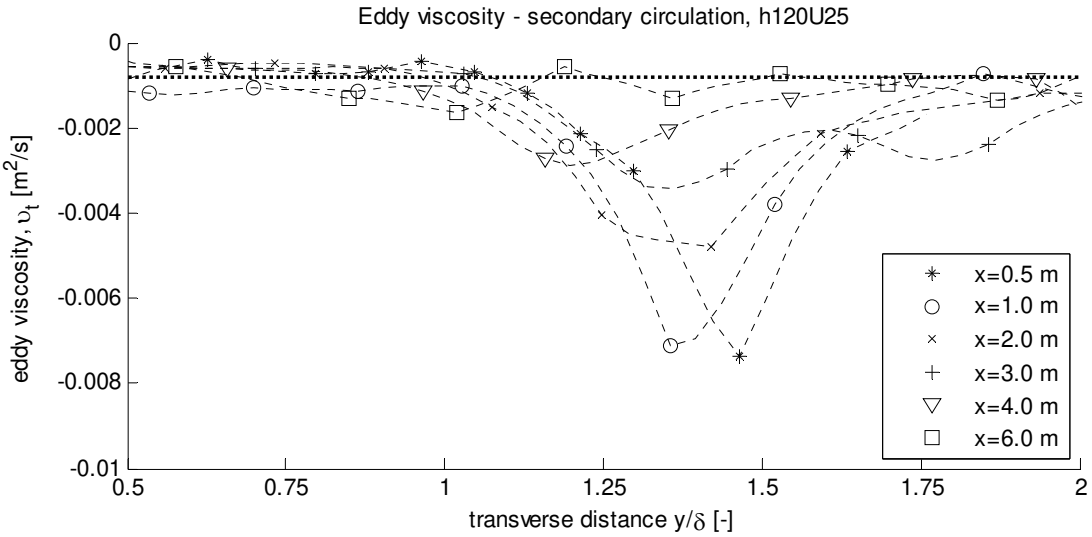

Figure 40; Eddy viscosity derived from the data in transverse direction for the case h120U25 by dividing the momentum transport by the transverse velocity gradient. The latter has been smoothed to create a continuous profile.

in the streamwise direction since the intensity of the secondary circulation decreases in x.
The eddy viscosity only quantifies the maximum momentum exchange by the secondary circulation since the maximum velocity vector is used in the definition. As can be seen in Figure 40, the position of the maximum eddy viscosity is difficult to quantify as it changes with y as well as y/δ. The viscosity decreases sideways and approaches a constant value at a distance of approximately 0.7·δ which is slightly less than twice the water depth. The decrease confirms the decreasing momentum exchange when moving to the centerline of the wake. The constant value to approach is rather negligible compared to the maximum value but is can be approximated for all cases by (34) with $C_2 \cdot C_1 \approx 0.47 \pm 0.04$.

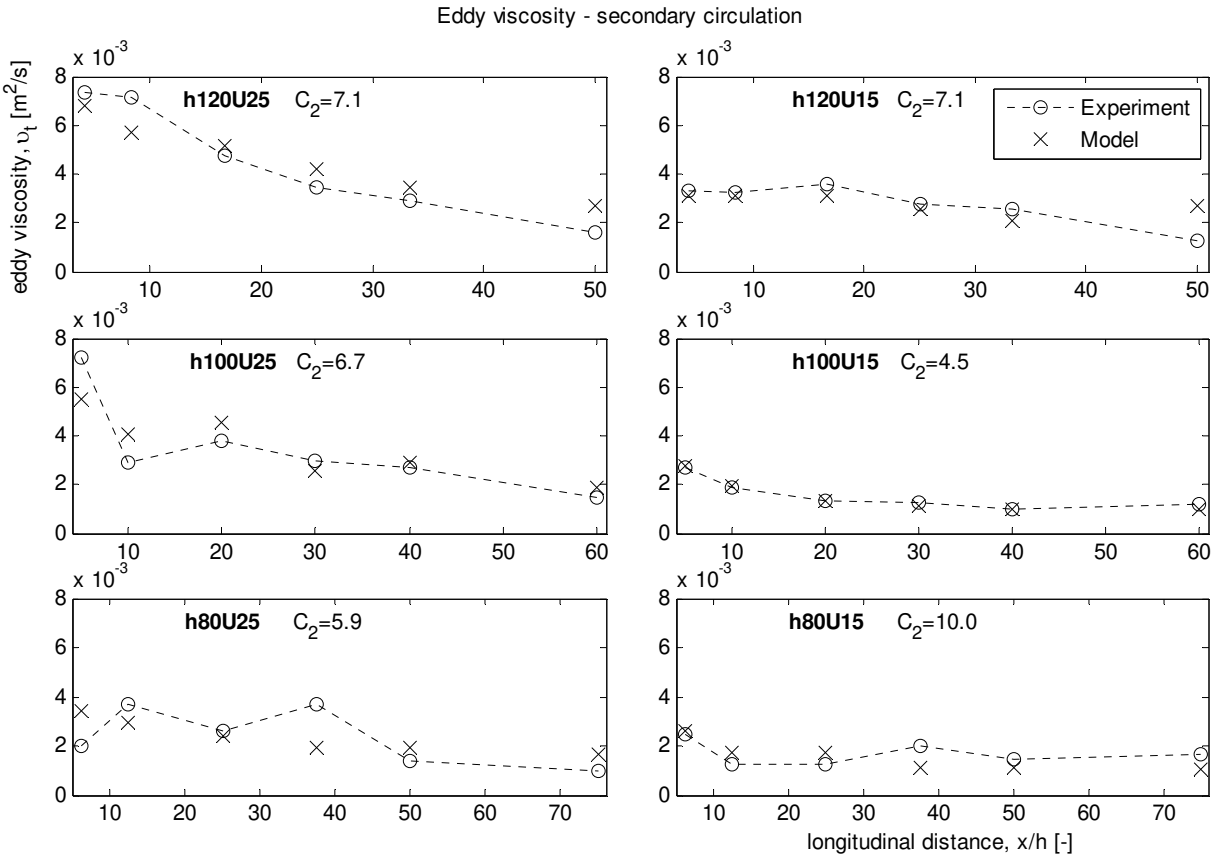

Figure 42; Experimental data and results of the estimation for the maximum eddy viscosity of the momentum transport by the secondary circulation. The experimental values are denoted by the circles and the dashed line. The estimations by means of (34) are denoted by the crosses.

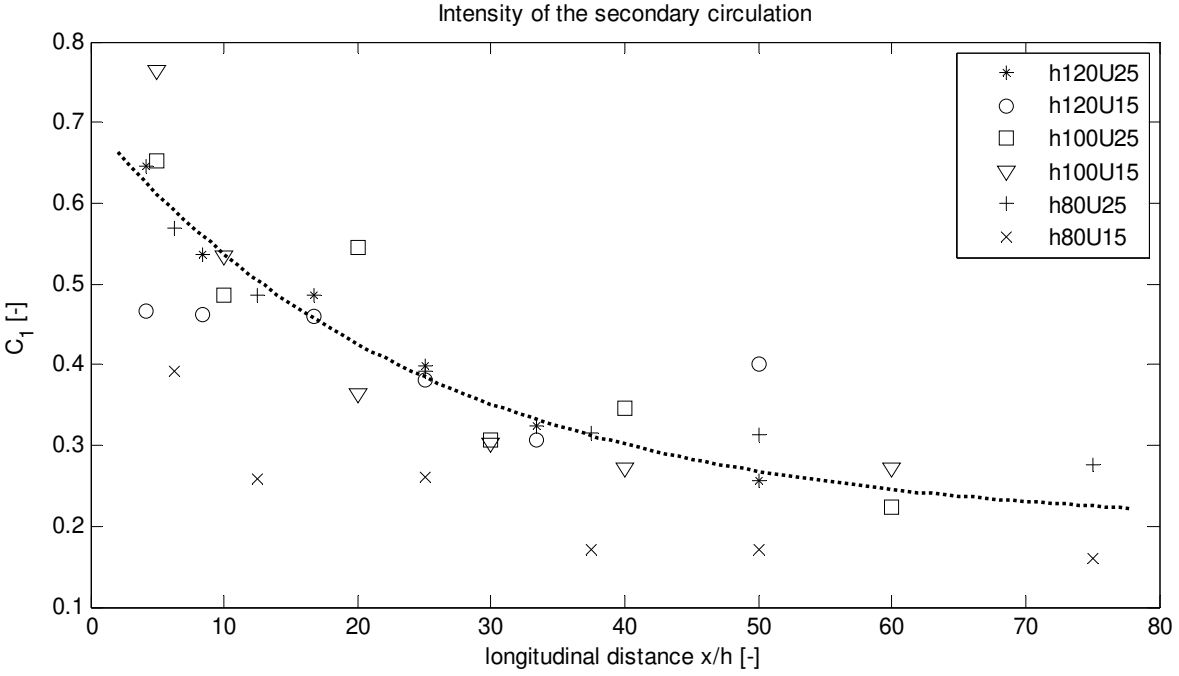

Figure 41; Intensity of the secondary circulation given by the coefficient C_1 which is defined as in §4.5. Note that the intensity is defined by the maximum velocity vector of the circulation and the coefficients for the cross section x=250 mm as in Figure 28 are not included.

As the coefficient C_1 changes in downstream distance, it needs to be quantified beforehand. The coefficient has been obtained from the data and is shown in Figure 41. With the exception of the case h80U15, the coefficient is depending on the normalized streamwise distance and seems to fit an exponential curve which is not entirely consistent with the coefficients shown in §4.5 which were suggested to be depending on the water depth and the ambient velocity.
The result for the maximum modeled eddy viscosity is shown in Figure 42. The coefficient C_2 is given and varies around 4.5 -10.

The spanwise Reynolds stress can be closed by an eddy viscosity parameter likewise. For the self similarity solution of the plane wake, the eddy viscosity is found to be depending on the velocity deficit and the wake half width (for instance Pope [2000]). In spanwise direction the eddy viscosity is assumed constant but experiments show the parameter to be too large near the edges of the wake (e.g. Tennekes & Lumley [1972]. However, due to the presence of the bottom, a suitable eddy viscosity becomes more complicated. Above the patch, the mixing layer growth is limited by the water depth and bottom friction. In the near wake, the transverse mass flow causes the vortices to be advected to the centerline of the wake weakening its dependency on the wake half width as characteristic length scale. Only in the far wake the wake half width becomes slowly a typical length scale of the vortices. Hence it is expected for the bottom shear characteristics to be governing for the eddy viscosity in the near wake while the velocity deficit or velocity gradient and the wake half width becomes increasingly dominant in the far wake. As used by Van Prooijen et al. [2005] for compound channel flow, the spanwise Reynolds stress can be split into a bottom turbulence part and a transverse shear part respectively, (35).

$$\frac{M_{mix}}{\frac{\partial U}{\partial y}} \approx \nu_t = C_3\, h\, U_* + C_4\, \delta^2 \frac{\partial U}{\partial y} \qquad \textbf{(35)}$$

For $C_3 = \frac{\kappa}{6}$ the bottom turbulence component would be identical to (31). In Figure 44 the eddy viscosity obtained from the data and the modeled eddy viscosity are shown. The coefficients are quantified by C_3=0.4 and C_4=0.04 of which the first is about six times as large as (31). The deviation of the estimated eddy viscosity at x=1 m is caused by the second term in (35) which indeed suggest the characteristics in the near wake are scaled by bottom friction. For x=4 m this deviation is absent. The outliers as obtained from the data at x=4.0 m are caused by irregularities in the cross sectional profile. For instance the velocity gradient is decreasing drastically in the edge of the wake, i.e. the velocity gradient is approaching zero (LHS of (35)).
Since a closure is needed for the shear velocity in (35) as well, the shear velocity can be evaluated by the friction coefficient squared and the local depth averaged velocity. In Figure 43 the friction coefficient is presented for all cases and three different cross sections. From the wake half width till outside the wake, the friction coefficient can be chosen as a constant value. The inner region of the wake however is greatly changing in x where only further downstream the whole spanwise profile of the coefficient can be chose as a constant. The magnitude of the friction coefficient is increasing for decreasing water depth and increasing ambient velocity. It does not scale however directly with the relative roughness height or a characteristic non dimensional velocity based parameter as the ratio of the maximum and minimum velocity. The appropriate quantification of the friction coefficient is therefore still lacking.

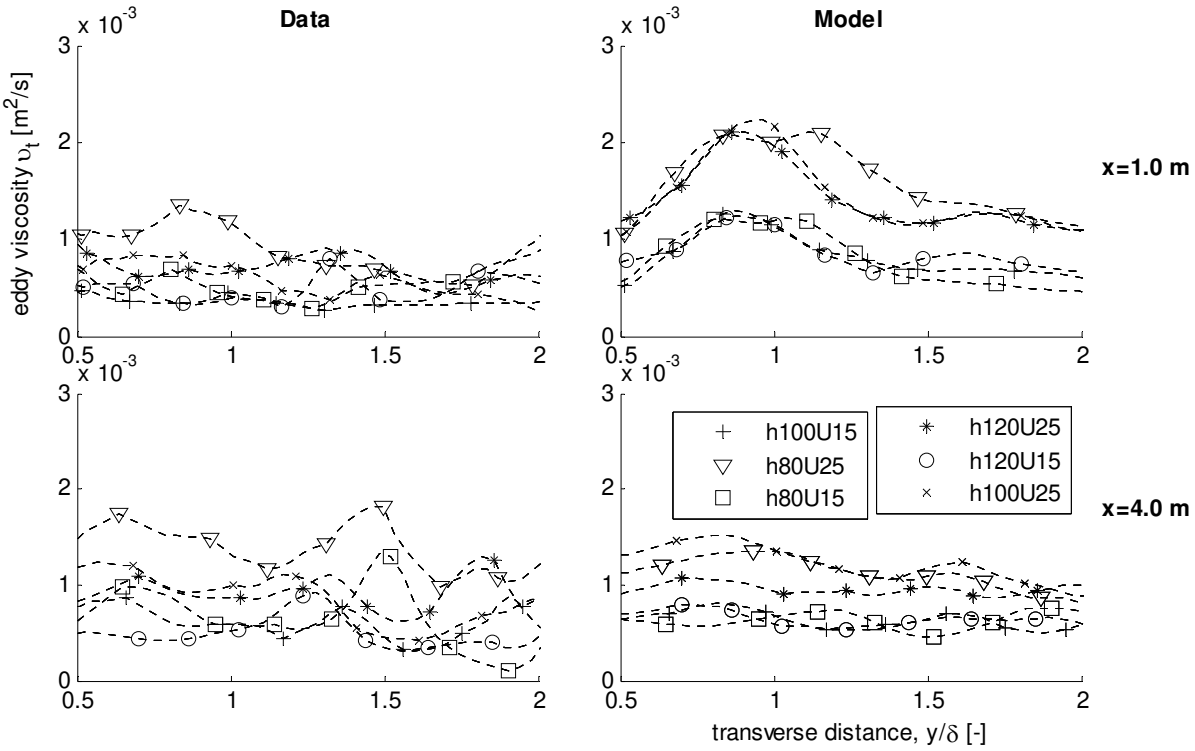

Figure 44; Eddy viscosity for the spanwise Reynolds stress u'v'. On the left the eddy viscosity obtained by the data, on the right the estimation based on (35) for C_3=0.4 and C_4=0.04.

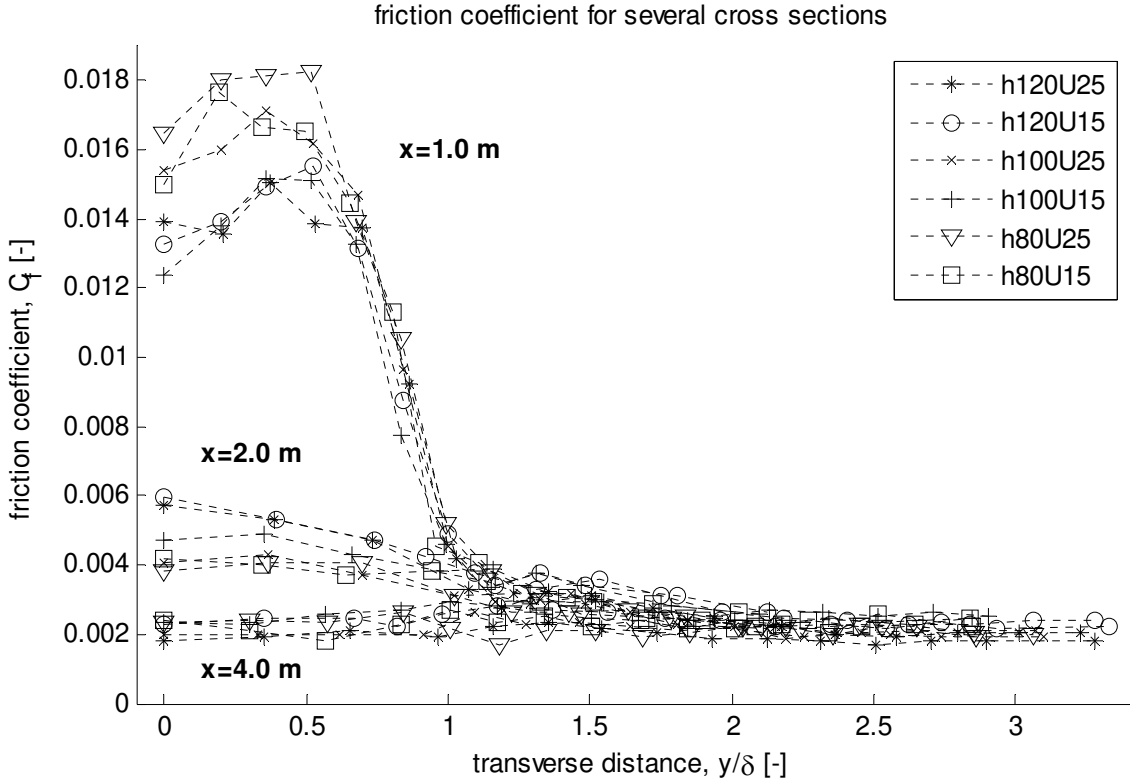

Figure 43; Friction coefficient for three cross sections for all cases. The coefficient reaches a constant value in the outer wake, the elevated value in the wake decreases with x.

5. Conclusions & recommendations

5.1. Conclusions

Little research was done in the past concerning the propagation of three dimensional effect in shallow wake flow caused by a roughness patch. Today's research on related subjects is dominated by emerging obstructions in shallow water where the flow can be assumed as (quasi) two dimensional. However the relevance of a submerged obstruction with increased roughness can be found in wake control, oyster reefs, river- and estuary bottoms and heterogeneous land occupancy. To get a better understanding of the consequences of the three dimensionality of the flow structures, experiments are performed in a wide shallow flume to examine these structures. The main objective is to examine whether the wake structure of a roughness patch can be treated as two-dimensional. To answer this objective, three goals have been formulated.

1. Compared to the data and models provided in literature, what are the differences in the characteristics, e.g. mean velocity profiles and spanwise Reynolds stress, of the two-dimensional wake and the data obtained in the wake of the roughness patch?
2. Based on the momentum exchange processes of the various mechanisms, which mechanisms are dominant and are the three-dimensional structures to be neglected?
3. If the wake structure cannot be expressed (completely) by expressions found in literature, can the flow be described by a (parameterized) model and/or parameter?

A literature study combined with an experimental investigation are performed to accomplish three goals.

Dominant mechanisms in the wake can be distinguished based on their momentum exchange. These mechanisms are the vortices in the horizontal plane, the transverse mass flow, bottom friction and the secondary circulation. The secondary circulation is not significantly present in two dimensional shallow wakes.
Streamwise velocity profiles of the three dimensional wake have found to behave in a similar way as the two dimensional wake with the exception of a lower gradient at the edge of the mixing layer. Based on the differential momentum exchange between the top and lower layer of the water column, the results suggest this to be caused by the secondary circulation. Secondly, this differential momentum exchange causes a cross sectional streamwise velocity gradient, where low streamwise momentum near the bottom is advected outwards relative to the wake, and high streamwise momentum at the surface advected to the centerline relative to the wake.
The recovery of the wake is faster for the cases of lower water depth caused by the interaction between the separate mixing layers. The position at where the interaction starts causes an increased turbulence intensity. The magnitude of this intensity decreases for decreasing water depth in which the velocity deficit at the end of the patch is suggested to be the causing factor.
As present in two dimensional wake flow, the transverse mass flow is present due to the recovery of the streamwise velocity at the centerline of the wake. The magnitude of the transverse mass flow is increasing with the velocity deficit caused by the relative roughness depth (k/h). The expected amplitude of the transverse velocity can be shown to be exponential in the near wake as:

$$V(x) = B_2 e^{B_1 x} \qquad \textit{(§4.3)}$$

In which length scale of the first coefficient B_1 [1/m] is proportional to the wake recovery length which can be estimated based on the mass conservation principle as shown in (4). The second coefficient B_2 [m/s] is equal to the initial transverse flow which happens to be depending on the relative roughness height of the patch.

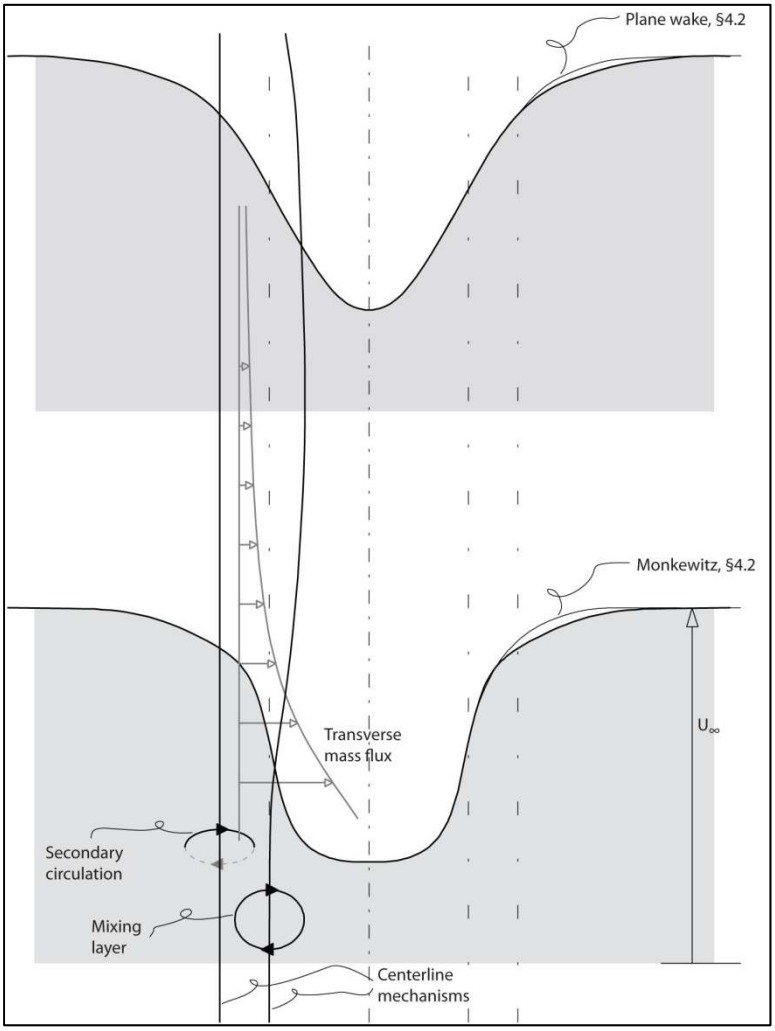

Figure 45; Schematization of the influence of the transverse mass flow, the mixing layer and the secondary circulation on the velocity profile and their interaction. Note that the influence of the transverse mass flow on the secondary circulation is limited.

The influence of the transverse mass flow on the structure of the wake can be visualized by the inward moving maximum spanwise Reynolds stress which is corresponding fairly to the intensity of the transverse velocity. Hereby a misalignment is formed between the wake half width and the maximum spanwise Reynolds stress. The secondary circulation is however not visibly affected by the transverse velocity component and is located around 1.5 times the wake half width (see Figure 45).

In order to check the accuracy of the data obtained a momentum balance based on a control volume has been performed resulting in an imbalance of about 20%. Considering this as reasonably good, the momentum exchange for the individual components could be compared. While the transverse mass flow and bottom friction are dominant in the near wake, all components present in the analysis are of importance in the far wake (i.e. hydrostatic pressure, bottom friction, transverse mass flow, secondary circulation and the spanwise Reynolds stress). The analysis of the control volume show the magnitude of the vortices in the horizontal plane to increase with respect to the secondary

circulation for decreasing water depth and increasing ambient velocity. Although valuable for the analysis, the control volume only presents the momentum exchange over a single boundary. The transport of momentum over the whole area can be obtained by taking the derivative of the local momentum. It shows a rather uniform distribution of the momentum transport by the mixing layer over depth while the transport of momentum by the secondary circulation is dominant in the lower water layer. It is also shown that the magnitude of the momentum transport by the secondary circulation increases for increasing waterdepth and the magnitude of the momentum transport by the lateral vortices decreases with increasing water depth. It implies the secondary current to become increasingly dominant in the stabilization of the wake for larger water depth, where it transports low streamwise momentum out of the wake and high streamwise momentum into the wake. Although the transverse mass flow is an order of magnitude larger in the near wake compared to the secondary circulation and the vortices in the horizontal plane, the three-dimensional effects of the secondary circulation are not negligible compared to two-dimensional wake flow.

As the stability parameter provides insight in the stability of the two dimensional wake, it cannot be applied to the three dimensional wake since the magnitude of the parameter is found to be two orders of magnitude smaller than values found for the two dimensional wake. This would suggest a negligible bottom friction which was found to be incorrect.
Although the three dimensional effects may not be neglected based on their momentum transport, three dimensional equations will require much more computational effort. For that reason it is preferable to include the effects into the two dimensional equations by means of a model. Making use of an eddy viscosity model, the maximum eddy viscosity in spanwise direction for the secondary circulation can be described by the product of the water depth and the shear velocity corrected by a coefficient.

$$v_t = C_2 \, C_1 \, \langle U_* \rangle \, h \qquad \textit{(§4.9)}$$

Where C_1 happens to be a function of the intensity of the circulation and seems to be exponentially decreasing in streamwise direction based on the experimental data.
Providing an eddy viscosity for the Reynolds shear stress is more complicated due to the misalignment of the maximum spanwise Reynolds stress and the wake half width. The eddy viscosity can be split into a bottom turbulence and a transverse shear part of which the first dominates in the near wake. Note that the relations provided are only calibrated on the parameters as shown in §3.2.5.

5.2. Recommendations

Research

While the three dimensional structures have been shown to be important in the recovery of the wake, the exact implication of the separate mechanisms has only been described qualitatively. In order to describe more specific consequences of the individual structures, more parameters need to be kept constant.

Hence in future research it is recommended to change the setting of the patch. One of the possibilities is to make sure the relative roughness height is at the same level as the bed, i.e. the patch is embedded. Hereby it is assured that the transverse mass flow is caused by the velocity deficit alone and not the volume occupied by the patch.

Another methodology is to decrease or increase the roughness height of the patch to cause equal velocity deficit or velocity gradient. In this way the influence of the waterdepth on the momentum transport mechanisms can be examined in more detail, i.e. the exchange of the secondary circulation versus the exchange by the mixing layer and their influence on the stability of the wake.

The results shown for the centerline velocity show a nearly constant value of about 80% of the ambient velocity at 60 times the water depth. Although a possible explanation has been given it has not been confirmed by data. Research in the far field of the wake can bring light to this discrepancy.

It is assumed that the secondary circulations alters the bottom shear distribution as shown by many as for instance Nezu & Nakagawa [1993]. However the resolution of the data obtained in this thesis described experiment is too low to determine the bottom shear stress more accurately. For the determination of the positioning of sedimentation and erosion, the bottom shear distribution is valuable and additional research is advised in the obtainment of more representative bed shear stresses. This can be done by measurements more close to the bed or possibly by using a mobile bed.

Data

In order to increase the accuracy of the data given, it is recommended to introduce another measuring technique for the characteristics close to the surface. This will increase the reliability of the extrapolation of the data from mid-depth to the surface.

ADV-profiler

Measuring the bed shear stress by an ADV-profiler requires close measurements near the wall. It is recommended to locate the optimum position of the profile close to the bed.

Appendix A

Due to the expected occurrence of secondary currents by the discontinuity in surface roughness, its theoretical framework has been elaborated here in more detail. The actual presence of the secondary current can be shown by the equation of turbulent kinetic energy (TKE) (Hinze, 1967).

$$\frac{\partial k}{\partial t} + U_j \frac{\partial k}{\partial x_j} = -\overline{(u'_i u'_j)} \frac{\partial U_i}{\partial x_j} + \nu \frac{\partial^2 k}{\partial x_j^2} + \frac{\partial}{\partial x_j}\left[-\overline{u'_j k} - \overline{\frac{1}{\rho} p' u'_j}\right] - \nu \overline{\left(\frac{\partial u'_i}{\partial x_j}\right)^2} \quad \textbf{(36)}$$

$$\text{with} \quad k = \frac{1}{2} u_i^2 \quad \textbf{(37)}$$

By assuming the flow to be statistically homogeneous in the streamwise direction and statistically stationary, all the derivatives to x and t are zero[14]. For fully developed flow the boundary layer has reached the water surface which means the boundary-layer approximation can be applied, hence all mean velocity gradients are neglected except for the velocity gradients in the vertical (Pope, 2000, p. 127). Furthermore, for high Reynolds numbers and not too close to the wall, the second term on the right hand side (RHS) can be neglected. The viscous dissipation term (last term on the RHS) can usually not be neglected since it is of the same order of magnitude as the production term (first term RHS) in certain parts of the layer. By applying the assumptions it follows for the fully written equation,

$$V \frac{\partial k}{\partial y} + W \frac{\partial k}{\partial z} = -\left[\overline{(u'v')} \frac{\partial U}{\partial y} + \overline{(u'w')} \frac{\partial U}{\partial z}\right] + \frac{\partial}{\partial y}\left[-\overline{v'k} - \overline{\frac{1}{\rho} p'v'}\right] + \frac{\partial}{\partial z}\left[-\overline{w'k} - \overline{\frac{1}{\rho} p'w'}\right] - \epsilon \quad \textbf{(38)}$$

Where 'ϵ' is denoted as the loss of TKE by viscous dissipation. The second and third term on the RHS are negligible in the region of $y/\delta < 0.4$, i.e. not in the upper part of the boundary layer (Pope, 2000, p. Fig. 7.34).

Making use of the continuity equation (note the flow is assumed to be statistically homogeneous in streamwise direction),

$$\frac{\partial V}{\partial y} + \frac{\partial W}{\partial z} = 0 \quad \textbf{(39)}$$

The gradient of V is equal but opposite signed to the gradient of W. From which W can be estimated to be of the same order as –V, for which a constant of proportionality is introduced 'C' (Hinze, 1967).

$$W\left[-C\frac{\partial k}{\partial y} + \frac{\partial k}{\partial z}\right] = -\left[\overline{(u'v')} \frac{\partial U}{\partial y} + \overline{(u'w')} \frac{\partial U}{\partial z}\right] - \epsilon \quad \textbf{(40)}$$

This equation simply states the advection of TKE to be equal to the difference between its production and dissipation. Evaluating the advection term we can assume the following for regions not to close to the sidewalls:

$$\left|\frac{\partial k}{\partial y}\right| \ll \left|\frac{\partial k}{\partial z}\right| \quad \textbf{(41)}$$

[14] The coordinate system is as follows: x is the streamwise direction, y is the transverse direction and z is the vertical direction.

Since the production of TKE is the highest in the buffer layer and the production is damped at the water surface, the gradient of TKE in the vertical will be negative signed. Again applying the simplifications on the equation, and rewriting the production term as 'P':

$$\mathrm{W}\frac{\partial \mathrm{k}}{\partial \mathrm{z}} = \mathrm{P} - \epsilon \tag{42}$$

Two different situations can be evaluated, namely the production to be smaller or larger than the dissipation. In the case of a net production, the RHS of eq. 6 is positive hence the LHS must also be. Which means a negative value of W representing downflow. The other way around, for excess dissipation we find upflow.
As has been found by for instance Hinze [1967], Vermaas et al. [2011] and Noat [1984], is the downflow above the roughness band due to excess production, and upflow above the smooth side.

Although the secondary currents can be visualized directly by presenting velocity vectors in a transverse cross-section, the origin of this secondary current is not explained well since only the consequences are explained above.
The origin of the secondary current is shown by the vorticity equation with its axis in streamwise direction. Assuming fully developed flow it yields:

$$\mathrm{V}\frac{\partial \Omega}{\partial \mathrm{y}} + \mathrm{W}\frac{\partial \Omega}{\partial \mathrm{z}} = \frac{\partial^2}{\partial \mathrm{y}\,\partial \mathrm{z}}\left(\overline{\mathrm{v'^2}} - \overline{\mathrm{w'^2}}\right) + \left(\frac{\partial^2}{\partial \mathrm{z}^2} - \frac{\partial^2}{\partial \mathrm{y}^2}\right)\overline{\mathrm{v'w'}} + \upsilon\left(\frac{\partial^2 \Omega}{\partial \mathrm{y}^2} + \frac{\partial^2 \Omega}{\partial \mathrm{z}^2}\right) \tag{43}$$

For positions not too close to the wall, the viscous term (third term on RHS) can be neglected. Which leaves us with the advection, the production and the Reynolds stress term respectively.
The production term, for instance $\frac{\partial^2}{\partial y \partial z}\overline{v^2}$ can be interpreted as the disbalance of a gradient in z of $\overline{v'^2}$ in the y direction, i.e. when the deviation of the distribution of $\overline{v'^2}$ on the right side of a control volume with height dz is unequal to the distribution on the left side of the control volume a moment is applied on the control volume. This moment can be corrected by the w'^2 component. Hence, when the v'^2 and w'^2 terms do not cancel, the local anisotropy of the flow causes the rotation around the axis in streamwise direction, i.e. a secondary current (Einstein & Li, 1958).

The existence of the secondary current can therefore be visualized by means of the production term $\frac{\partial^2}{\partial y \partial z}\left(\overline{v'^2} - \overline{w'^2}\right)$ or the V and W velocity components in a cross section. The preference goes to the latter which has to do with the procedure to capture quantitative information from the first. As shown by Tominaga & Nezu [1991] who examined the production term $\frac{\partial^2}{\partial y \partial z}\left(\overline{v'^2} - \overline{w'^2}\right)$ for the case of compound channel flow, the discontinuity in geometry at the boundary of the main channel and the floodplain show large values of the production term. In cross sections including lines of constant $\left(\overline{v'^2} - \overline{w'^2}\right)$ the magnitude of the production term can be recognized by the lines being not parallel to each other or the boundaries. To obtain the data quantitatively is highly sensitive for errors. The main cause for this is the need for a high resolution of the measurement grid[15].

[15] In the paper of Tominaga & Nezu [1991] a method is described to overcome this problem partially, by fitting a higher order polynomial to the data and inspecting the accuracy by means of continuity. Nevertheless, the results should be accepted with cautious due to the inclusion of relative errors.

Appendix B

The stability parameter has been derived by Chu et al. [1991] as the ratio of the production of TKE by shear over the dissipation of TKE by bottom friction. In this appendix, the derivation will be recapped shortly. For a full presentation the reader is referred to Chu et al. [1991].
The origin lies within the two dimensional shallow water equations, although with respect to (17) no Reynolds averaging has been applied, see (44)-(46), where the components are averaged over depth.

$$\frac{\partial(hu)}{\partial x}+\frac{\partial(hv)}{\partial y}=0 \tag{44}$$

$$\frac{\partial(hu)}{\partial t}+\frac{\partial(hu^2)}{\partial x}+\frac{\partial(huv)}{\partial y}=-h\frac{\partial p}{\partial x}-\frac{1}{\rho}\tau_{bx} \tag{45}$$

$$\frac{\partial(hv)}{\partial t}+\frac{\partial(huv)}{\partial x}+\frac{\partial(hv^2)}{\partial y}=-h\frac{\partial p}{\partial y}-\frac{1}{\rho}\tau_{by} \tag{46}$$

For the bottom shear stress a quadratic dependency on the velocity has been used, see (47)-(48). The expressions provide information about the direction of the mean flow as well (Vreugdenhil, 1994).

$$\frac{\tau_{bx}}{\rho}=\frac{1}{2}C_f\,u\sqrt{u^2+v^2} \tag{47}$$

$$\frac{\tau_{by}}{\rho}=\frac{1}{2}C_f\,v\sqrt{u^2+v^2} \tag{48}$$

As the equations are rewritten in a different form, a stability analysis is conducted by introducing disturbances for the velocity and pressure components. The mean transverse velocity is assumed to be zero as well as the streamwise velocity gradient. These two simplifications imply the absence of a mean pressure gradient. The spanwise gradient of the streamwise velocity is forced by a spanwise changing bottom friction or water depth. By linearization the resulting equations, it is found:

$$\frac{\partial u'}{\partial x}+\frac{\partial v'}{\partial y}=0 \tag{49}$$

$$\frac{\partial u'}{\partial t}+U\frac{\partial u'}{\partial x}+v'\frac{\partial U}{\partial y}=-\frac{\partial p'}{\partial x}-\frac{C_f U}{h}u' \tag{50}$$

$$\frac{\partial v'}{\partial t}+U\frac{\partial v'}{\partial x}=-\frac{\partial p'}{\partial y}-\frac{C_f U}{2h}v' \tag{51}$$

By summing the product of (50) with u' and (51) with v' the equation for the TKE is found, in which the advection of TKE is found on the LHS, and the redistribution of TKE by pressure disturbances, the production of TKE and the dissipation of TKE on the RHS respectively, see (52).

$$\frac{\partial k}{\partial t}+U\frac{\partial k}{\partial x}=-\left[u'\frac{\partial p}{\partial x}+v'\frac{\partial p}{\partial y}\right]-u'v'\frac{\partial U}{\partial y}-\frac{C_f U}{2h}[2u'^2+v'^2] \tag{52}$$

The ratio of the dissipation over the production leads to the stability parameter as in (53).

$$S_f=\frac{F}{P}=\frac{2\langle u'^2\rangle+\langle v'^2\rangle}{-\langle u'v'\rangle}\left(\frac{C_f}{2h}\frac{U}{\frac{\partial U}{\partial y}}\right) \tag{53}$$

Appendix C

The quality of the ADV profiling has been examined shortly in order to find the optimal setting for the experiments. The settings have been changed on three properties, the amount of clay, the sampling frequency and the sampling size. The first consist of the addition and without the addition of clay. For the sampling frequency, the maximum of 100 Hz has been used as well as 50 Hz. The sampling size has been varied from the minimum of 1 mm to 4 mm distance between the points of measurement. Due to the clear improve in quality for the addition of clay, some tests are not done for the absence of clay. The tests were done for a waterdepth of 120 mm and a discharge of 54 l/s. The ADV was positioned above the smooth part next to the roughness patch, the velocity in the upper part of the column should therefore be around 0.2 m/s.

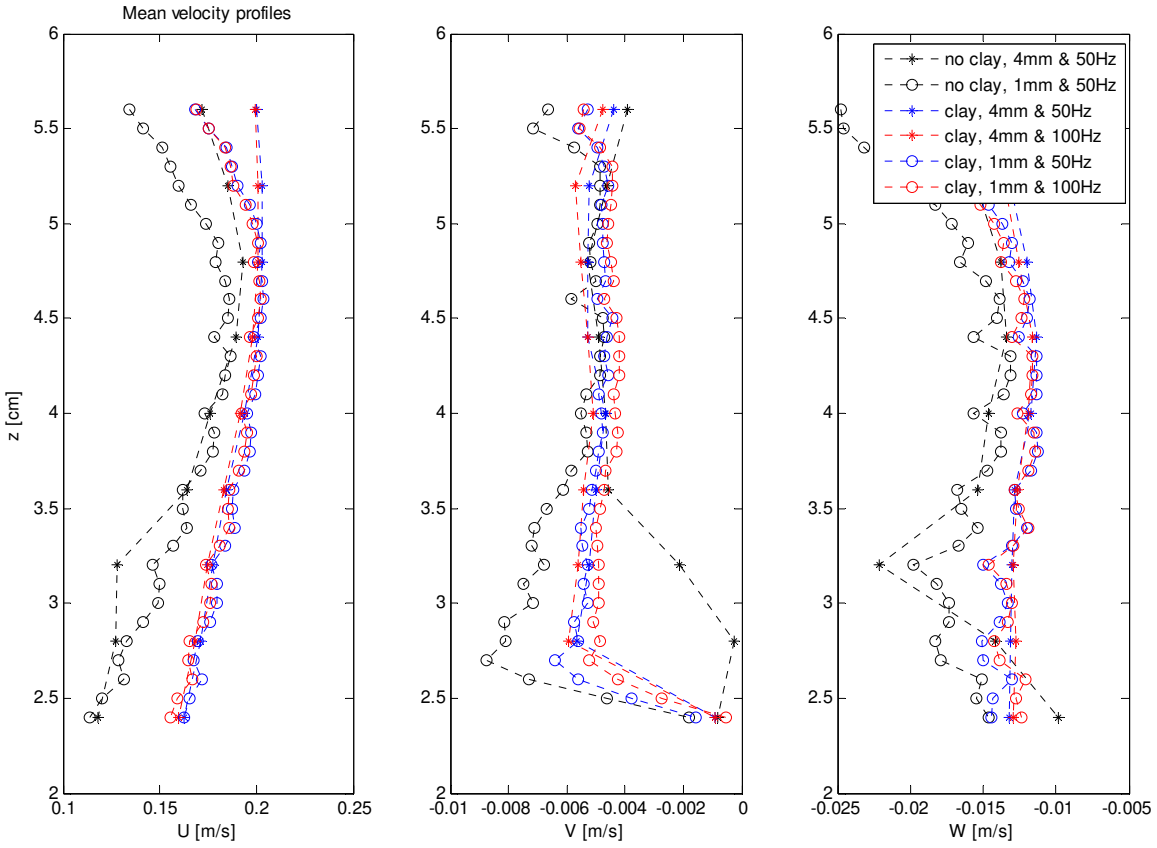

Figure 46; Mean velocity profiles for various settings. Note the underestimated streamwise velocity for the cases without the additional clay particles.

In Figure 46, the mean velocity profiles are shown for the various settings. For the streamwise velocity, the data obtained without the addition of clay causes an underestimation of the velocity expected. Also the edges of the signal deviate significantly. The cases of small sampling size do not show a clear smooth profile. Like the cases without clay, the high resolution of the sampling size shows deviations in the lower edge as well for the turbulent fluctuations .

For the higher order statistics, also the cases including 100 Hz frequency sampling, show deviations, especially large gradients. In these experiments it seems the highest resolution in settings possible is limiting the quality of the signals, therefore a midway is chosen between the settings presented here which is a sampling frequency of 60 Hz and a sampling size of 3 mm, corresponding to a sampling volume of 0.027 cm^3.

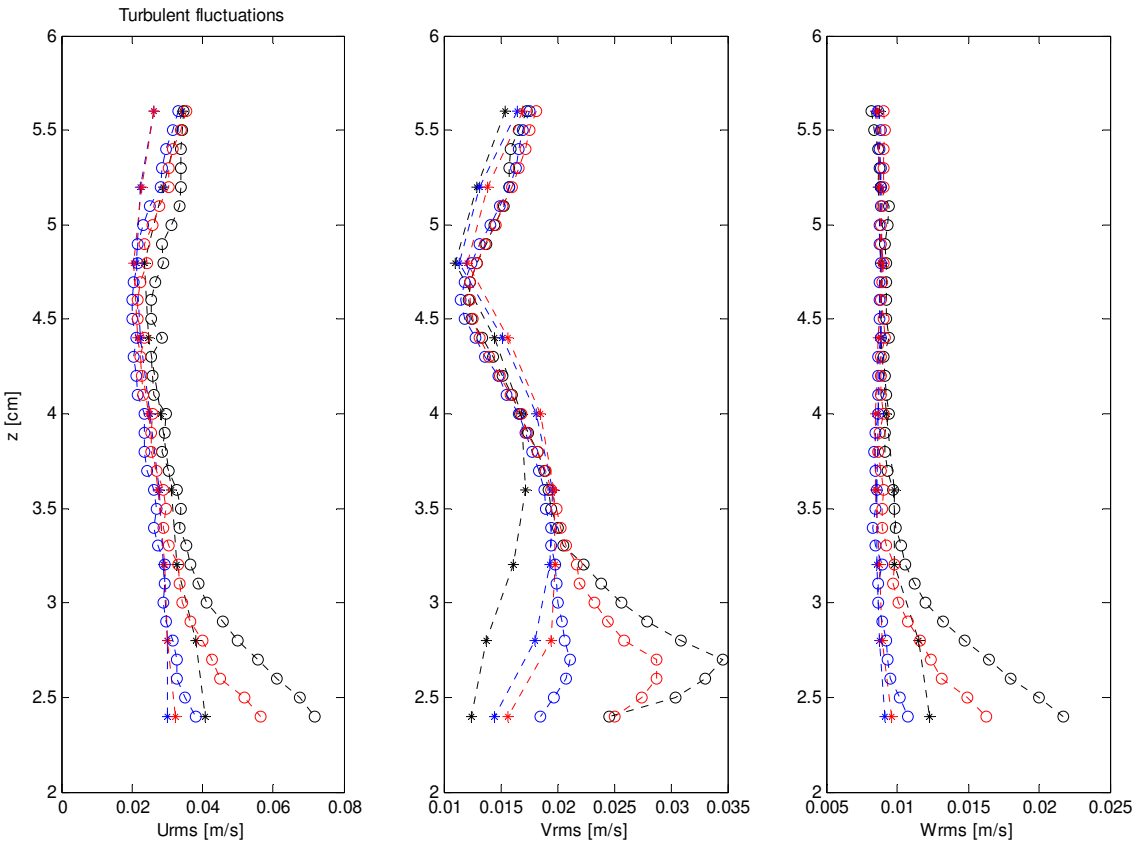

Figure 47; Turbulent fluctuations for various settings. Note the lower edge for a lower sampling size.

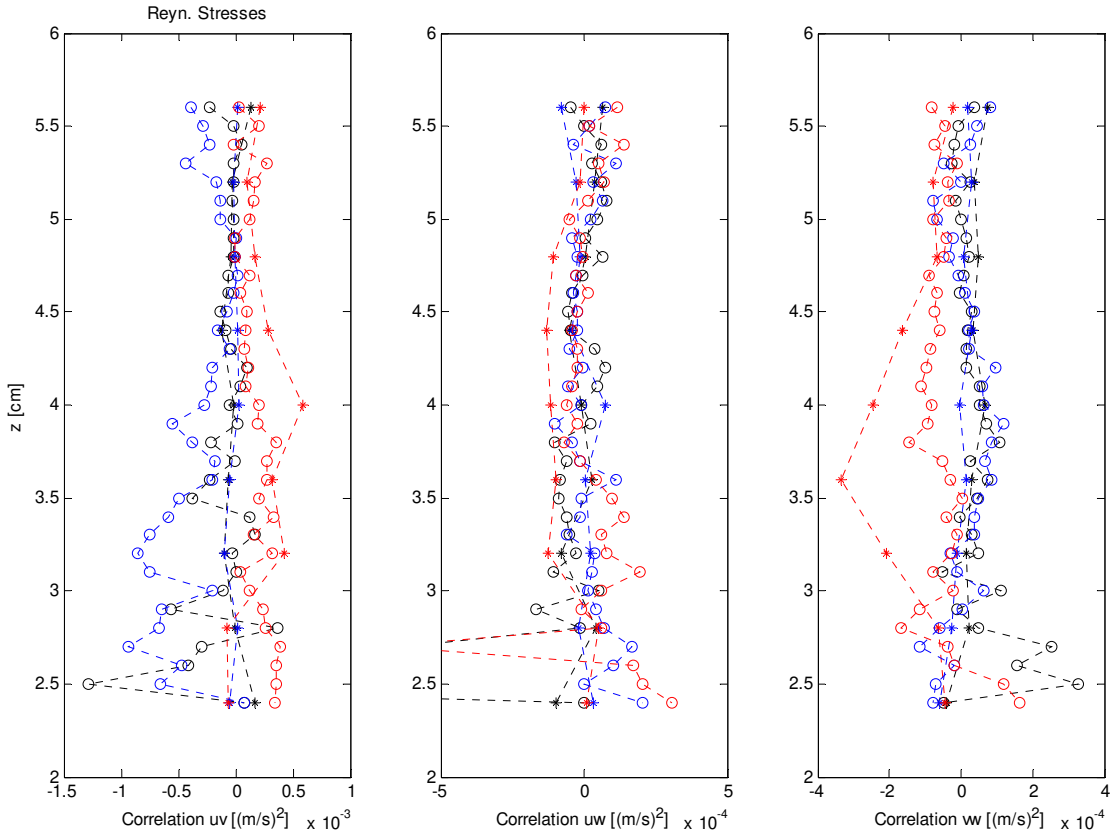

Figure 48; Reynolds stresses for various settings.

Appendix D

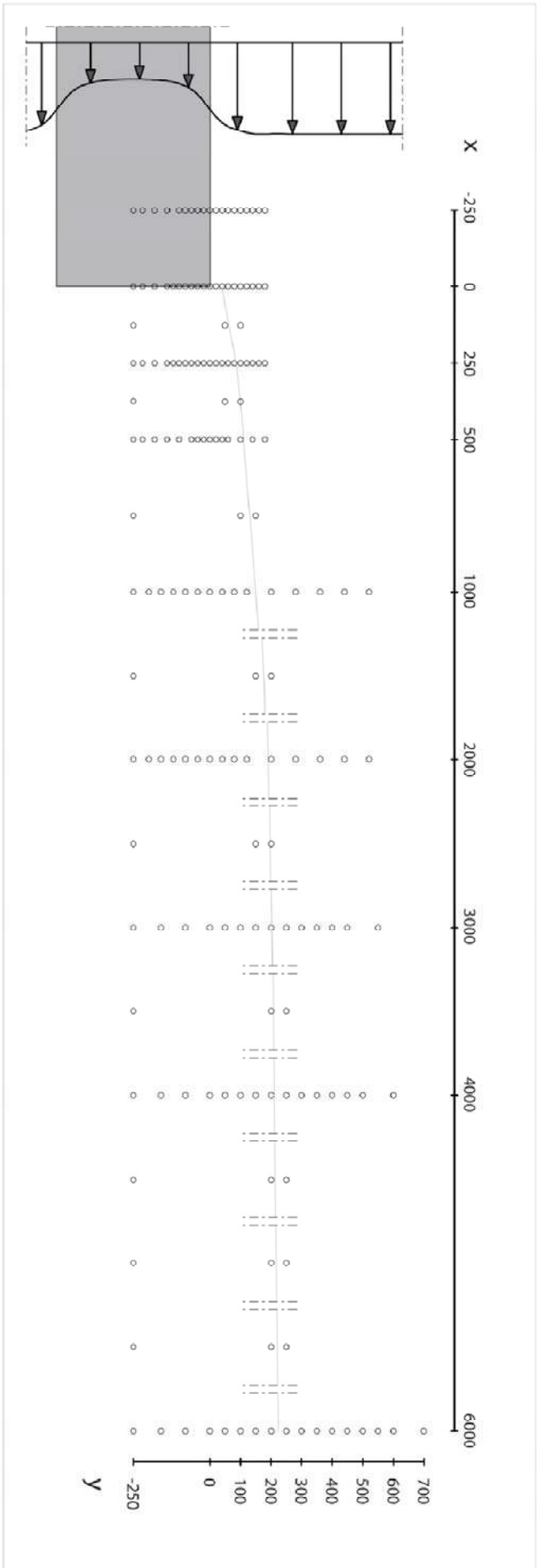

Figure 49; Measurement locations for all six cases. The trailing edge of the roughness patch has been copied in the diagram.

Appendix E

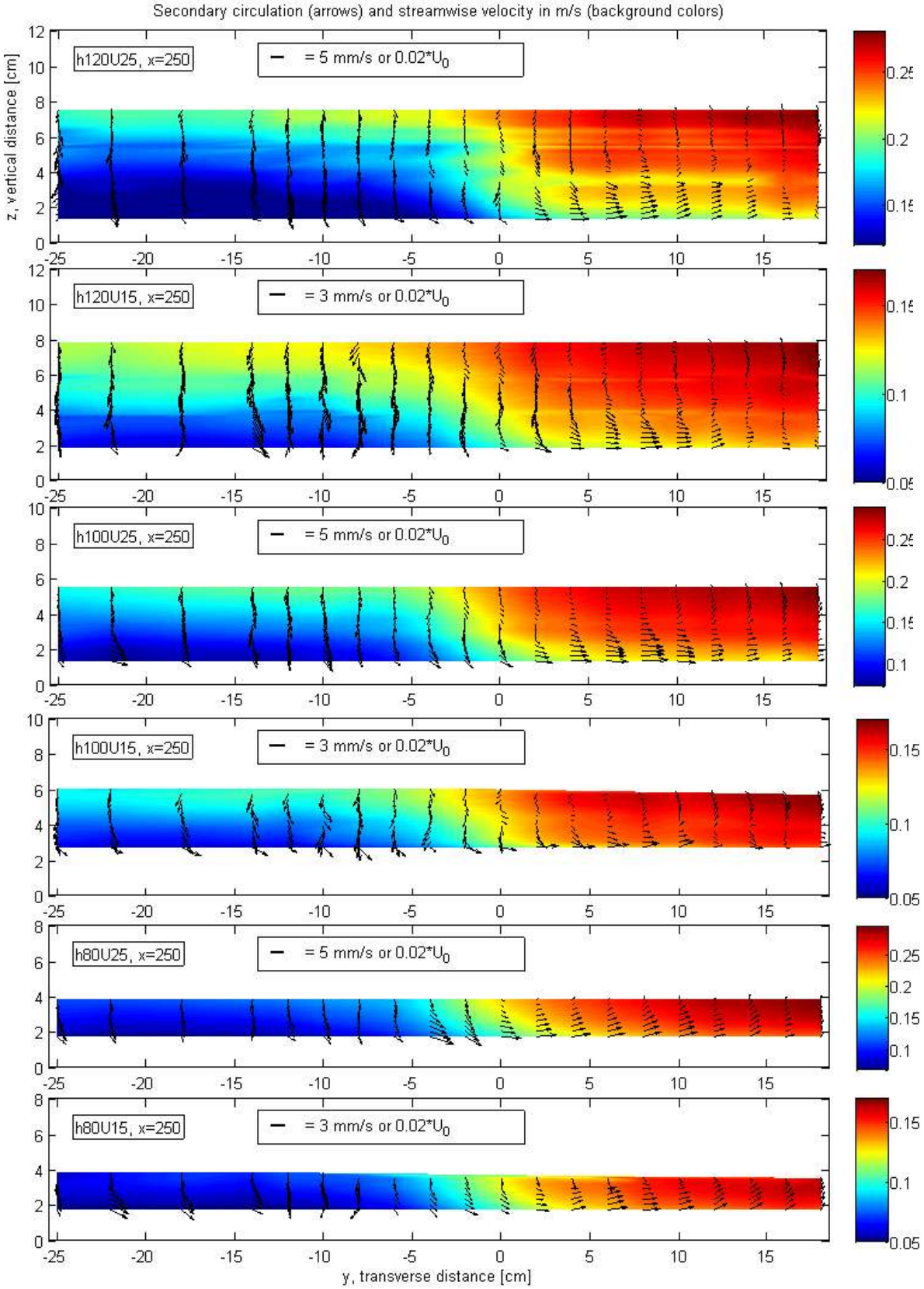

Figure 50; Secondary circulation just behind the roughness patch for all six cases. In the background the magnitude of the streamwise velocity has been indicated by colors.

References

Balachander, R., & Tachie, M. (2001). A study of boundary layer–wake interaction in shallow open channel flows. *Experiments in Fluids* , (30) 511-521.

Belcher, S., Jerram, N., & Hunt, J. (2003). Adjustment of a turbulent boundary layer to a canopy of roughness elements. *J. Fluid Mech.* , 488. 369-398.

Carmer, C. v. (2005). *Shallow turbulent wake flows: Momentum and mass transfer due to large-scale coherent vortical structures.* Karlsruhe: Universitätsverlag Karlsruhe.

Chen, D., & Jirka, G. (1995). Experimental study of plan turbulent wakes in a shallow water layer. *Fluid Dynamics Res.* , (16) 11-41.

Chen, Z., Ortiz, A., Zong, L., & Nepf, H. (2012). The wake structure behind a porous obstruction and its implications for deposition near a finite patch of emergent vegetation. *Water Resour. Res.* , 48. W09517.

Chu, V., Wu, J.-H., & Khayat, R. (1991). Stability of transverse shear flows in shallow open channels. *J. Hydr. Eng.* , (117) 1370-1388.

Einstein, H., & Li, H. (1958). Secondary currents in straight channels. *Trans. Am. Geoph. Union* , (39) 1085-1088.

Goring, D. G., & Nikora, V. I. (2002). Despiking acoustic Doppler velocimeter data. *Journal of Hydraulic Engineering* , 117-126.

Hinze, J. (1967). Secondary currents in wall turbulence. *Phys. Fluids* , (10) S122.

Huthoff, F., Augustijn, D., & Hulscher, S. (2007). Analytical solution of the depth-averaged flow velocity in case of submerged rigid cylindrical vegetation. *Water Resour. Res.* , (43) W06413.

Ikeda, S. (1981). Self-formed straight channels in sandy beds. *J. Hydr. Division* , 389-406.

Ingram, R., & Chu, V. (1987). Flow around islands in Rupert Bay: An investigation of the bottom friction effect. *J. Geophys. Res.* , (92, C13) 14.521-14.522.

Jirka, G. (2001). Large scale flow structures and mixing processes in shallow flows. *J. Hydr. Res.* , 567-573.

Krogstad, P., Antonia, R., & Browne, L. (1992). Comparison between rough- and smooth-wall turbulent boundary layers. *J. Fluid Mech.* , (245) 599-617.

Lacey, R., & Rennie, C. (2012). Laboratory investigation of turbulent flow structure around a bed-mounted cube at multiple flow stages. *J. of Hydraul. Eng.* , 71-84.

Monkewitz, P. A. (1988). The absolute and convective nature of instability in two dimensional wakes at low Reynolds number. *Phys. Fluids* , 999- 1006.

Nakamura, Y., & Ohya, Y. (1984). The effects of turbulence on the mean flow past two-dimensional rectangular cylinders. *J. Fluid Mech.* , (149) 255-273.

Negretti, M., Socolofsky, S., Rummel, A., & Jirka, G. (2005). Stabilization of cylinder wakes in shallow water flows by means of roughness elements: an experimental study. *Experiments in Fluids* , (38) 403-414.

Nezu, I., & Nakagawa, H. (1993). *Turbulence in open-channel flows.* Rotterdam: Balkema.

Nezu, I., & Onitsuka, K. (2001). Turbulent structures in partly vegetated open-channel flows with LDA and PIV measurements. *J. Hydr. Research* , 629-642.

Nikora, V. (1999). Origin of the "-1" spectral law in wall-bounded turbulence. *Physical review letters* , 734-736.

Noat, D. (1984). Response of channel flow to roughness heterogeneity. *J. Hydraul. Eng.* , (110) 1568-1587.

Panofsky, H., & Townsend, A. (1964). Changes in terrain roughness and wind profile. *Quart. J. Roy. Meteor. Soc.* , (90) 147-155.

Park, C.-W., & Lee, S.-J. (2000). Free end effects on the near wake flow structure behind a finite circular cylinder. *J. Wind Eng.* , (88) 231-246.

Pendergrass, W., & Arya, S. (1984). Dispersion in neutral boundary layer over a step change in surface roughness - I. Mean flow and turbulence structure. *Atmos. Environ.* , (18) 1267-1279.

Pope, S. (2000). *Turbulent Flows.* Cambridge: Cambridge University Press.

Prooijen, v. B. (2004). Shallow mixing layers. *Dissertation, TU Delft, Delft* .

Prooijen, v. B., Battjes, B., & Uijttewaal, W. (2005). Momentum exchange in straight uniform compound channel flow. *J. Hydral. Eng.* , 175-183.

Rodríguez, J., & Garcia, M. (2008). Laboratory measurements of 3-D flow patterns and turbulence in straight open channel with rough bed. *J. Hydr. Res.* , 46:4. 454-465.

Rominger, J., & Nepf, H. (2011). Flow adjustment and interior flow associated with a rectangular porous obstruction. *J. Fluid Mechanics* , 636-659.

Sand-Jensen, K., & Madsen, T. (1992). Patch dynamics of the stream macrophyte. *Callitriche cophocarpa, Freshwater Biol.* , (27) 277-282.

Schiereck, G. (2003). *Introduction to bed, bank and shore protection.* Delft: VSSD.

Studerus, F. (1982). Sekundärströmingen im offenen Gerinne über rauhen Längsstreifen. *Dissertation ETH Nr. 7035.* Zürich: Eidgenössischen Technischen Hochschule Zürich.

Tennekes, H., & Lumley, J. (1972). *A first course in turbulence.* MIT Press.

Tominaga, A., & Nezu, I. (1991). Turbulent structures in compound open-channel flow. *J. Hydr. Eng.* , (117) 21-41.

Tominaga, A., Nezu, I., Ezaki, K., & Nakagawa, H. (1989). Three-dimensional turbulent structure in straight open channel flows. *J. Hydr. Research* , (27) 149-173.

Townsend, A. (1976). *The structure of turbulent shear flow.* Cambridge: Cambridge University Press.

Uijttewaal, W., & Booij, R. (2000). Effects of shallowness on the development of free-surface mixing layers. *Physics of Fluids* , (12) 392-402.

Vermaas, D. (2007). MSc Thesis: Mixing layers in open channel flow over heterogeneous bed roughness. *MSc Thesis Wageningen University* .

Vermaas, D., Uijttewaal, W., & Hoitink, A. (2011). Lateral transfer of streamwise momentum caused by a roughness transition across a shallow channel. *Water Resour. Res.* , (47) W02530.

Vreugdenhil, C. (1994). *Numerical methods for shallow-water flow.* Dordrecht: Kluwer.

Wang, Z.-Q., & Cheng, N.-S. (2005). Secondary flows over artificial bed strips. *Adv. Water Res.* , 28. 441-450.

Wesenbeeck, B. v., Koppel, J. v., Herman, P., & Bouma, T. (2007). Does scale-dependent feedback explain spatial complexity in salt-marsh exosystems? *Oikos* , 152-159.

Wolanski, E., Imberger, J., & Heron, M. (1984). Island wakes in shallow coastal waters. *J. Geoph. Res.* , 89. 10.553 - 10.569.

Wygnanski, I., Champagne, F., & Marasli, B. (1986). On the large scale structures in two-dimensional, small-deficit turbulent wakes. *J. Fluid Mech.* , 168 - p. 31-71.

Yalin, M. (1992). *River mechanics.* Oxford: Pergamon Press.

Zedel, L., & Hay, A. (2011). Turbulence measurements in a jet: Comparing the Vectrino and VectrinoII. *Working Conference on Current Measurement - CMTC*, (pp. 173-178). Monterey.

Zong, L., & Nepf, H. (2012). Vortex development behind a finite porous obstruction in a channel. *J. Fluid Mech.* , (691) 368-391.